NORTHWESTERN UNIVERSITY

The effect of crack-parallel stresses on fracture properties of quasibrittle and ductile materials

A DISSERTATION

SUBMITTED TO THE GRADUATE SCHOOL
IN PARTIAL FULFILLMENT OF THE REQUIREMENTS

for the degree

DOCTOR OF PHILOSOPHY

Theoretical and Applied Mechanics

By

Hoang Nguyen

EVANSTON, ILLINOIS

June 2022

ABSTRACT

The goal of this thesis is to develop an experimental setup to evaluate and analyze the effect of crack-parallel stress on the fracture response of materials. In standard fracture test configurations, the crack-parallel normal stress is negligible. However, a new type of experiment, briefly named the *gap test*, revealed that it was not the case for many quasibrittle and ductile materials. This experiment consists of a simple but new modification of the standard three-point-bend test. Plastic pads with a near-perfect yield plateau are used to generate a constant crack-parallel stress, and the end supports are installed with a gap that closes only when the pads yield. This way, the test beam transits from one statically determinate loading configuration to another, making evaluation easy and accurate. In addition to the *gap test*, the size effect method, devised in the 1990s, was used to obtain an unambiguous fracture energy based on the geometric scaling of cracked structures with positive geometry. Unlike the work-of-fracture method which measures the total fracture energy on structures of one size, the size effect method was shown in 2014 to give a unique value of the initial fracture energy. It can be widely applied.

For *quasibrittle materials*, i.e. heterogeneous materials consisting of brittle phases, concrete was used as a typical example. The gap test showed that a moderate crack-parallel compressive stress could increase up to ≈ 2 times the Mode I (opening) fracture energy of concrete, and reduce it to almost zero when approaching the compressive stress limit. Behavior with a similar trend can be observed within the characteristic length scale, which may be explained by the interplay between friction, interlocking and dilation of microcracks and microsurfaces. To explain this phenomenon, computational models were used, but not all of them could reproduce the results. In particular, the line-crack models, including the basic and enhanced phase-field models with one or two phase variables (PFM), cohesive crack models (CCM), and extended finite element method (XFEM)

cannot capture such an effect. The reason lies in the inability of these methods to generate a fracture process zone (FPZ) with *finite width*. Consequently, the FPZ (if it exists) is one dimensional and cannot interact with the crack parallel stress. On the contrary, finite elements (FE) or any method that does not confine the energy dissipation within a line in theory can capture the effect of crack -parallel stresses (both in-plane and out-of-plane). However, they must be characterized by a realistic tensorial softening damage model whose vectorial constitutive law captures oriented mesoscale frictional slip, microcrack opening and splitting with microbuckling (i.e. the scalar stress-displacement softening law of CCM and tensorial models with a single-parameter damage law are inadequate). This is best accomplished by the rack band model which, when coupled with microplane model M7, fits the test results satisfactorily. Other standard tensorial strength models such as Drucker-Prager cannot reproduce these effects realistically. Alternatively, one can think of using an equation to describe the dependence of G_f as a function of σ_{xx} (as well as σ_{zz} and σ_{xz} in general). However, this is an approximation that ignores stress tensor history and can only be accepted in some special cases where the crack-parallel stresses are negligible.

For *ductile materials*, even though the small-scale yielding fracture of plastic-hardening metals (conceived by Hutchinson, Rice and Rosengren) is a well-established theory, their scaling law is not fully understood. Therefore, it must be evaluated before proceeding to the effect of crack-parallel stresses. Unlike the fracture of quasibrittle materials, the fracture of plastic-hardening materials is complicated by a millimeter scale singular yielding zone (YZ) that forms between the micrometer-scale FPZ and the elastic (unloading) material on the outside. Essential for the large-scale transitional size effect is the YZ size, which is here calculated from the condition of equivalence of the virtual works of the plastic-hardening and elastic singular stress fields within the transition zone. The size effect analysis requires taking into account not only the dissipation in the FPZ delivered by the J-integral flux of energy through the yielding zone, but also the energies re-

leased from the structure and from the unloaded band of plasticized material trailing the advancing yielding zone. Consequently, to describe the transition from micron-size to structure-size specimens (in which both large-scale and small-scale yielding are present), we develop a modified size effect method that includes three asymptotes and requires nonlinear optimization. The size effect law is verified by scaled tests of notched specimens of aluminum.

The *gap test* is again applied to evaluate the effect of an extrinsically applied σ_{xx} on the initial fracture energy of aluminum alloy, an example of a ductile material. The "extrinsic" nature of σ_{xx} should be emphasized to highlight the novelty of this work. In fact, the crack parallel stress can arise "intrinsically" due to the constraint arising at the tip, which is a result of plastic strain in this area and the geometry of the specimen. This phenomenon was extensively studied in the 1990s by Shih, Hutchinson and many other authors under the name of J-T (or J-Q) theory. To avoid such "intrinsic" effect, the thickness, the length-to-depth ratio and the notch length ratio of the specimens in this study were chosen so that such "intrinsic" parallel stress can be negligible. Using the size effect method as previously described, it is found that, at crack-parallel stress σ_{xx} = 40% of the yield strength, the G_f of aluminum (or J_{cr}) is roughly doubled and the r_p, which represents collectively the effective radius of the YZ and the characteristic length (or size) of the FPZ, is roughly tripled. To reproduce these results in finite element analysis, one must again consider a realistic tensorial elastic-plastic-damage constitutive law. Such analysis is essential to distinguish the changes in FPZ and in YZ, in which the former must be simulated with a finite width, as in the crack band model.

The results in this thesis have broad implications for many materials, e.g., shale, fiber composites, sea ice, foams, bone, and metallic structures that possess the grain boundary comparable to the structural size. These results challenge the century-old hypothesis of constancy of materials fracture energy and set a new paradigm to define the adequacy of the experiments to fully describe the

mechanical properties of a material. In addition, these results can be used as a source of validation to evaluate the performance of a damage/fracture model.

ACKNOWLEDGEMENTS

This thesis has been done when I am a student in the Theoretical and Applied Mechancis program at Northwestern University (NU). I gratefully acknowledge the support from the National Science Foundation, the Army Research Office, the Vietnam Education Fellowship, and the Department Terminal Year Fellowship. In addition, I would like to acknowledge the support from Infrastructure Laboratory in the department of Civil and Environmental Engineering, the Micro and Nanomechanics Lab in the department of Mechanical Engineering at NU, and the Structural and Concrete Materials Research Laboratory at the University of Illinois Chicago (UIC). I also want to thank Quest High Performance Computing (HPC) Cluster at NU, Frontera and Stampede HPC at Texas Advanced Computing Center (TACC), and Carbon HPC at Argonne National Laboratory for providing computing resources. Above all, I would like to express my deepest gratitude towards my co-advisors, Prof. Zdeněk P. Bažant and Prof. Horacio D. Espinosa, for their guidance, support, and encouragement. For Prof. Bažant, I sincerely appreciate the amount of diligence and dedication he put into this project (and others that we have been working on). His demanding advising style encourages me to obtain more knowledge skills to prove or disprove a hypothesis, which leads me to a level I would never imagine. For Prof. Espinosa, I am indebted to him for teaching me a new language that my seven-year-ago-self would not appreciate–experimental mechanics. He encourages me to dig deeper into the physics of a problem and use the obtained knowledge to guide the model development. Both of my advisors help get me through new challenges that even they are not familiar with, making my time here a wonderful journey of finding what I am really excited about. I would like to send many thanks to the committee members: Prof. Gianluca Cusatis and Prof. Victor Lefèvre for spending their precious time to participate, read, and provide constructive feedback on my thesis. I'm also grateful to Prof. John Rudnicki for his

feedback on my doctoral candidate proposal. I would like to acknowledge Dr. Madura Pathirage, Dr. Masoud Rezaei, and his advisor, Dr. Mohsen Issa, for assisting me with the test on concrete. The acknowledgement also goes to Dr. Dönmez, Abdullah for carrying out a major part of the experiments on aluminum alloy and dedicating time for long remote discussion. Mr. Houlin Xu is thanked for helping me with the calibration. I would like to thank my hardcore collaborator, Dr. Xu Zhang, for performing good-quality high-resolution imaging of the cracks on transition metal dichalcogenides cracks and devoted his time to many helpful debates. My sincere thanks also goes to Prof. Jeff Paci for giving me guidance with many density functional theory codes. Aside from the project presented in this thesis, I would like to thank Dr. Saeed Rahimi-Aghdam for involving me in the projects dealing with thermo-hygro-mechanical responses of cement and shale. Thanks are also due Dr. Wenfeng Li and Dr. Luke Frash for a collaboration on hydraulic fracture in plaster. My gratitude goes to Dr. Rafael Soler-Crespo for helping me in my first year. I would like to thank my former colleagues: Dr. Viet Chau, Dr. Wen Luo, and Dr. Mohammad Rasoolinejad, Dr. Cunbao Li for many helpful discussions. I also want to express my gratitude towards the former and current members of the Micro and Nanomechanics Lab–Dr. Prithvijit Mukherjee, Cesar Patino, Dr. Shiva Nathamgari, Nibir Pathak, Jin Choi, Nicolas Alderete, Dr. Matthew Daly, and Graham Pritchard for their constant physical and mental support. I am grateful to my Vietnamese mentors Mr. Quoc D. Le ,Prof. Quoc K. Do, Prof. Phuoc T. Nguyen, Prof. Y Q. Nguyen for motivating me to pursue a PhD degree at NU. My life in the US is full of great experience thanks to my friend, Dr. Tho Le, Dr. Anh Le, Dr. Dung Nguyen, Dr. Trung Nguyen, Dr. Anh Bui, Dr. Duyen Cao, Dr. Lan Chu, Thao Nguyen, Dat Ha, and San Dinh. Last but not least, I would like to express my deepest gratitude to my parents and my younger brother for their wholehearted love and their calling every day just to make sure I am OK. I also owe my grandma, who passed away two years ago, an apology for not being able to make it back in time.

DEDICATIONS

To my parents, my younger brother and my grandmas.

TABLE OF CONTENTS

Acknowledgments 6

Dedications 9

List of Figures 15

Chapter 1: Introduction and Background 21

1.1 Length scale of quasibrittle and elastic-plastic fracture mechanics 22

1.2 Why crack-parallel stresses matter? 24

1.3 The non-uniqueness of the cohesive law and the importance of the scaling test in determining a unique fracture energy 28

1.4 T-stress in metal–the current progress 29

Chapter 2: Size effect method and the effect of crack parallel stresses on quasibrittle materials 31

2.1 Scaling of structural strength for quasibritlle materials 31

2.2 Gap test - a new setup to investigate the effect of crack-parallel stress on the fracture energy of materials 37

2.3 Further aspects and details of the gap test 39

2.4 Functions for stress intensity factor and energy release rate of the gap test 43

2.5 Concrete mix design and dimensions of tested specimens 44

2.6 Material calibration results 45

2.7 The effect of crack-parallel stress on G_f 47

2.8 Physical mechanism of crack-parallel stress effect on G_f 50

2.9 Basic features of microplane model 53

2.10 Further simulations of crack-parallel stress effect on G_f 60

2.11 Limitations of cohesive crack model and contrast with crack band model 62

2.12 Gap test for crack-parallel tension 66

2.13 Alternative test methods 66

Chapter 3: Scaling of structural strength for ductile materials 70

3.1 Scaling tests - a missing piece in understanding the fracture of ductile materials . . 70

3.2 Scaling of near-tip field and of structure strength in absence of a characteristic length 72

3.3 Review of power-law stress-strain relation for plastic-hardening metals 74

3.4 Large-scale yielding in small structures 76

3.5 For comparison—derivation of scaling law for quasibrittle structures with no plasticity 79

3.6 Energy dissipation rates of small-scale yielding in large structures 81

3.7 Size effect on fracture strength of plastic-hardening structures 83

3.8 Size effect method for testing material fracture properties in large enough structures in small-scale yielding range 86

3.9 Simple asymptotic matching of small-to-large-scale yielding 86

3.10 Small-to-large-scale asymptotic matching anchored in yielding zone 87

3.11 Closed-form approximation of small-to-large-scale yielding and evaluation of size effect tests 89

3.12 Tests of notched specimens of aluminum and comparisons 90

3.13 The optimum fit of size effect law for ductile materials 91

3.14 Scaling for the FPZ-to-yielding transition and intermediate asymptote 96

3.15 Numerical predictions 97

3.15.1 The Bai-Wierbiczki model and its prediction 97

3.15.2 The extrapolation to the micrometer scale 99

Chapter 4: The effect of crack parallel stresses on ductile materials 100

4.1 Yielding zone size under crack-parallel stress via energy matching of singular fields 100

4.2 Calculation of dimensionless angular functions and work expressions 103

4.3 Gap Tests of Aluminum 105

4.4 Aluminum test results and their discussion 110

4.5 The effect of T-stresses via Bai-Wierbiczki model 116

4.5.1 The prediction with σ_{xx} 116

Chapter 5: The effect of the crack-parallel stress in other materials and the implication of the gap test results in different engineering problems 118

5.1 The applicability to other materials 118

5.1.1 Fiber reinforced concrete (FRC) 118

5.1.2 Shale 119

5.2 Crack-parallel stresses at nanoscale 119

5.2.1 The fracture response of pristine transition metal dichalcogenides and the brittleness of covalent bonds 119

5.2.2 The emergence of heterogeneous structures due to the presence of vacancies 121

5.2.3 The effect of crack parallel tensile stress 125

5.3 The implications of the crack-parallel stress in engineering problems 125

5.3.1 Crack-parallel stresses: where do they matter in practice? 125

5.3.2 Gap test as an indicator of a model capability to describe damage and fracture properly 127

Chapter 6: Conclusion and Future direction 129

6.1 For quasibrittle materials 129

6.2 For ductile materials 130

6.3 Opportunities for future research 133

References 145

Appendix A: Bai-Wierbickzki model for metals 147

Appendix B: The approximate constancy of the yielding zone in scaled structures with small-scale yielding 149

Appendix C: Distinguish between the intrinsic vs. extrinsic crack-parallel stress 150

Appendix D: The calibration process for microplane model, Bai-Wierbiczki model and others 151

Appendix E: Description of models used in chapter 5 153

E.1 Basic phase-field model 153

E.2 Phase-field modifications by Feng and Wu 157

E.3 Phase-field modifications by Fei and Choo 158

E.4 Overview of the concept of peridynamics 158

E.5 The mathematical basis of bond-associated PD 163

E.6 The mathematical form of CDPM2 model by Grassl *et al.* [66] 163

E.7 The ability of the crack-band microplane model in describing curved crack 164

LIST OF FIGURES

1.1 The emergence of the nonlinear zone in the crack front in elastic-plastic (ductile) (b) and in quasibrittle materials (c), compared with homogeneously brittle materials (a). 23

1.2 (a) A sketch of the mechanics governing the strength of scaled RC beams, reproduced from [21]; (b) The effect of the crack-parallel stress on the microcracks pattern leading to the difference in pressure profile; and (c) the fracture of sea ice near the legs of oil platforms. 26

1.3 Standard notched fracture specimens that neglect the effect of crack-parallel stress. 27

1.4 (a) A traction-separation curve without crack-parallel stress; (b) A linear approximation of the initial fracture energy; (c) The effect of the boundary on the fully developed FPZ, which leads to ambiguity in the work-of-fracture and the G_F measurement. 29

2.1 (a) Geometrically scaled compact-tension specimens; (b) The FPZ with finite length and width; and (c) The applicability of the size effect method on different quasibrittle materials and on different configurations, reprinted with the authors' permission [21]. 33

2.2 (a) Schematic experimental set-up (with coordinates x, y, z); (b) Real set-up; and (c) Stress-strain behavior of plastic pad corresponding to two values of tested σ_{xx} (note that only a short segment of the quasi-plateau intervened during the rise of bending moment 36

2.3 (a) Experimental procedure; (b) A load-machine displacement behavior (note that within the segment F, which is what matters for G_f, the change in pad reaction (dashed line), is negligible); and (c) Extracted load-CTOD. 38

2.4 (a) A circular plastic pad under compressive force; and (b) The shape of the pad should be designed to minimize H. 42

2.5 Calibrations and validations to obtain parameters for M7-CBM: (a) Uniaxial compression of cylinders; (b) Uniaxial compression of square prisms; and (c) Brazilian splitting tests. 46

2.6 (a) Linear regression of size effect method and (b) The size effect curve plotted in log-log scale. 47

2.7 (a) G_f ($G_{f0} = 86.7$ N/m) as a function of σ_{pad} (dashed curve) and of σ_{xx} (solid curve); (b) c_f ($c_{f0} = 8.8$ mm) as a function of σ_{pad} (dashed curve) and of σ_{xx} (solid curve). 48

2.8 (a) Suggested mechanisms for enhancement and diminishing of G_f; (b) Mohr circles corresponding to the M7-CBM predictions in Fig. 2.5a), with σ_{yy} = nominal strength at peak load for samples of medium size; and (c) A closer look to the region of small σ_{xx}. 52

2.9 (a) The planes of inelastic deformations in a representative volume element of particulate composite are imagined to be lumped into one continuum point. (b) Decomposition of strain vector into its normal and shear components along basis vectors $(\boldsymbol{n}, \boldsymbol{l}, \boldsymbol{m})$. (c) The normals to radial rays through the circled points on this icosahedron define the system of microplanes. (d) The mechanisms that can be captured by microplane model. (e) Predictor-corrector method for each component on one microplane allows the damage to emerges naturally without using a damage variable. (f) The constitutive algorithm to compute stresses from strain tensor via microplane decomposition. 56

2.10 (a) The conversion of contour integral to domain integral and how it is calculated using FEM (b). (c) The results from a non-converged and converged contour. (d) An approximation of the variation of FPZ using J-integral contour and M7 model. 59

2.11 G_f and c_f as functions of σ_{xx} subject to different values of anti-plane stress σ_{zz} (with results approximated by Eqn. 2.21). 61

2.12 (a) History dependence of the stress path; (b) G_f as a function of σ_{xx} predicted by tensorial models by Grassl *et al.* [66] σ_{xx}; (c) G_f as a function of σ_{xx} predicted by tensorial Drucker-Prager model [67] a; and (d) A premature failure predicted by D-P ahead of the main crack tip before moment M is applied. 64

2.13 Gap test for crack-parallel tension. 67

2.14 An alternative test method considered to generate σ_{xx} with proportional loading. . . 68

3.1 (a) Stress-strain behavior of the deformation theory of plasticity (nonlinear elasticity); (b) Elasto-plastic constitutive law with different n; (c) Approximation of total stress-strain by plastic stress-strain relation (elastic strain is neglected); and (d) Partition of strain energy into released and dissipated. 75

3.2 (a) Actual and equivalent yielding zones with the same area (or volume), as indicated by FE analysis using von-Mises type plastic-hardening constitutive law; (b) Propagation of the equivalent yielding zone as crack grows. 84

3.3 Comparison of accuracy of Eq. (3.56) in approximating the exact solution, Eq. (3.55). 90

3.4 (a) Schematic and (b) actual setup of notched three-point-bend tests; (c) Geometrically-scaled specimens with the same transverse thickness and various depths, $D = 6, 12, 24$ mm (specimens with $D = 48$ mm were tested but not shown here). 92

3.5 Optimum fits of size effect law to test result on aluminum beams based on: Eq.(3.39) (a,d), Eq.(3.46) (b,e), Eq.(3.50) (c,f). The transverse thickness of specimens was 10 mm (a,b,c), and 25.4 mm (1 in.) [85] (d,e,f). 93

3.6 J-integrals on different contours, computed on the specimens with $D = 24$ mm and transverse thickness $b = 25$ mm (d,e,f). Path 3 and 4 indicate path-independence, but 1 and 2 not. 95

3.7 (a) Micron-scale asymptote for specimens with sizes comparable to process zone size (volume confined within slip planes or grain boundaries). (b) Simulated and extrapolated results by Bai–Wierzbicki [95] plasticity-damage model. 97

4.1 Schematic radial stress profiles; (a) intersection of yielding and elastic zones; and (b) mismatch areas (cross-hatched) for equilibrium matching of both zones by virtual work. 101

4.2 (a) Uniaxial stress-strain curves of aluminum (Al), copper (Cu) and polyvinyl-chloride (PVC); (b) The deformed shapes of Al, Cu and PVC loading pads after compression test; (c,d) compression tests of PVC pad and perforated Cu pad.(Note: w and t are the cross sectional dimensions and r is the radius). 106

4.3 (a) The geometry of the Al specimens used; (b) Geometrically similar specimens of four scaled sizes; (c) The load-deflection curves of the scaled specimens; (d) Failure and grown crack image in 8D sized specimen. 108

4.4 (a) The loading scheme of the gap tests using PVC pads and corresponding failure and cracking; (b) The load-deflection curves of the gap tests using PVC pads generating a 67 MPa crack-parallel compression in the Al specimens. 109

4.5 (a) The loading scheme of the gap tests using Cu pads. and the corresponding failure and cracking; (b) The load-deflection curves of the gap tests using Cu pads that generate a 172 MPa crack-parallel compression in the Al specimens. 110

4.6 (a) Measured size effect data of aluminum for four different specimen sizes D and three different ratios of crack-parallel stress σ_{xx} to yield strength f_y in logarithmic scales; (b) ditto in a linear regression plot (the square and triangle data points give averages of 3 tests, the diamond data points the averages of 2 tests) 111

4.7 Experimentally obtained data on (a) the dependence of fracture energy G_f of aluminum on the ratio of crack-parallel compressive stress σ_{xx} to yield strength σ_y; and (b) ditto for the dependence of the characteristic size r_p of the fracture process zone. 112

4.8 (a) Size effect curves of aluminum in logarithmic scales for $\sigma_{xx} = 0$ and for large σ_{xx} $(= T)$; (b) Mohr and von Mises yield envelopes of metals; (c) size effect curves of concrete, showing, for comparison, that for quasibrittle materials the curves do not cross; (d) dependence of G_f on σ_{xx} in concrete. 114

4.9 (a) The fitted fracture energy resulted from Eq. 3.50; (b) The variation of G_f with different σ_{xx}. 115

4.10 (a) The prediction of the size effect of aluminum alloy using Bai-Wierbiczki's model; (b) The corresponding change of the YZ as σ_{xx} increases. 117

5.1 (a–b) The variation of G_f and c_f of 3% Dramix-fiber-reinforced concrete as functions of σ_{xx} ; (c–d) The variation of G_f and c_f of shale with bedding plane normal and parallel to the crack as functions of σ_{xx}. 120

5.2 (a) Domain sizes used in the uniaxial and fracture tests, D = 40nm; (b) A comparison between HR-TEM and atomically simulated images of the crack tip and crack edges on a pristine monolayer; (c) The stress distribution of σ_{yy} in front of the tip; (d-f) The interaction of the main crack with isolated Se, Mo/Se_2, and Se vacancy lines (red arrows show the propagating direction of the crack); (g) Typical nominal stress-strain curves for pristine and in the presence of these types of vacancies; and (h) The effect of these vacancies on $MoSe_2$ fracture energy (yellow bar indicates the experimental value). 124

5.3 (a-b) Two possible atomic changes when the heterogeneous structure arises at the crack front due to the isolated vacancies, leading to the formation of a strengthening phase and ultimately a crack deflection (c). (d) The energy difference between path-a and path-b transitions without (left0 and with (right) a crack-parallel tension $\sigma_{xx} = 0.1\sigma_t$ in which such a stress suppresses the formation of the strengthening phase. 126

5.4 a) The deviations from the experimental fracture energy of CB, PF, and PD models. b) Gap test results showing the relative change of measured concrete fracture energy G_f versus crack-parallel compression σ_{xx}, normalized by uniaxial compression strength σ_c, and comparisons to CB, PF, and PD models. 128

B.1 The constancy of the YZ's size. 149

E.1 Schematic concept of phase-field φ, chosen with w_0 or supporting band, and profile of damage $c = 1 - \varphi$. 155

E.2 a) Central forces (or lattice bonds) connecting each material point to all other material points within its horizon, shown as two dashed circles, and the same for the horizon (unreduced) of a point at the boundary (note the reduced density of connections near the boundary) [130]. b) Particles (or grains) in a quasibrittle material and their interactions by contact normal and shear forces. c) Horizons spanning a crack or fracture process zone, with interactions AA′, AA″, AA‴, BB′, CC′, DD′ when considered undisturbed by the crack (note that CC″, DD″ must be eliminated, while BB″ is getting progressively weaker while moving along the FPZ closer to crack tip. 160

E.3 a) A curved crack on the compact-tension specimen with a hole in front of the notch is captured by the CB model in (b). c) The load versus crack-opening-displacement (COD) curve of the specimen in (a). 164

CHAPTER 1

INTRODUCTION AND BACKGROUND

Fracture mechanics' origin dates back to a paper by Inglis [1] in which he attempted the elastic solution for stresses at the vertex of an ellipsoidal cavity in an infinite solid and observed that, as the ellipse approached a line crack (i.e., as the shorter axis tended to zero), the stress at the vertex of the ellipse tended to infinity. Noting this fact, Griffith [2] concluded that, in presence of a crack, the stress value could not be used as a criterion of failure since the stress at the tip of a sharp crack in an elastic continuum is infinite no matter how small the applied load. The propagation of cracks therefore relies on an energy criterion of failure, which serves as the basis of the classical elastic fracture mechanics (or EFM). This form of fracture mechanics, however, was applicable only to homogeneous brittle materials, such as glass at the scale larger than several millimeters. The question of applicability of these classical theories to other materials was explored long ago on quasibrittle [3] and ductile materials [4], [5]. Now, we understand that the physical processes occurring in the fracture of these materials are very different from those taking place in the fracture of the homogeneous brittle materials and so are their relevant length scales. The new developments of fracture mechanics that can be applied to these kinds of fracture, therefore, appeared only during the late 1970s and the 1980s. While there are many fracture mechanics theories based on the diversity of materials behavior, in this thesis, only quasibrittle and elastic-plastic fracture mechanics will be discussed.

1.1 Length scale of quasibrittle and elastic-plastic fracture mechanics

What sets the new forms of fracture apart from the classical EFM? Fig.1.1 illustrates this difference by the emergence of the fracture process zone (FPZ) and the yielding zone (YZ). The FPZ often arises in quasibrittle materials, i.e., heterogeneous materials consisting of brittle constituents and inhomogeneities not negligible compared the structure dimensions. The FPZ is a nonlinear zone characterized by progressive softening for which the stress decreases at increasing deformation. The YZ, on the other hand, is a non-softening nonlinear zone characterized by hardening plasticity or perfect plasticity, for which the stress increases at increasing deformation or remains constant. Depending on the relative sizes of these two zones and of the structure, one may distinguish three types of fracture behavior. In the first type of behavior (Fig.1.1a), the whole nonlinear zone (and thus also the FPZ) is small compared to the structure size. Then, the entire fracture process takes place almost at one point-the crack tip. The whole body is elastic, and elastic fracture mechanics (EFM) described before can be applied. This type of model is a good approximation for perfectly brittle materials such as Plexiglas, glass, brittle ceramics, and metals embrittled by hydrogen diffusion. It must be emphasized that the applicability of EFM is relative, i.e., the structure must be sufficiently large compared with the FPZ. Thus, the overall behavior of extremely large concrete structures, such as gravity dams, can be described by EFM, while the behavior of a very small part made of a brittle fine-grained ceramic cannot. In the second and third types of behavior (Figs. 1.1b,c), the ratio of the nonlinear zone size to the structure size is not sufficiently small, leading to the inapplicability of the EFM theory. Although it can still be applied in a certain equivalent sense if the nonlinear zone is not very large.

In the second type of behavior (Fig.1.1b), we include situations where most of the nonlinear zone consists of elastoplastic hardening or perfect yielding, and the size of the actual FPZ in which

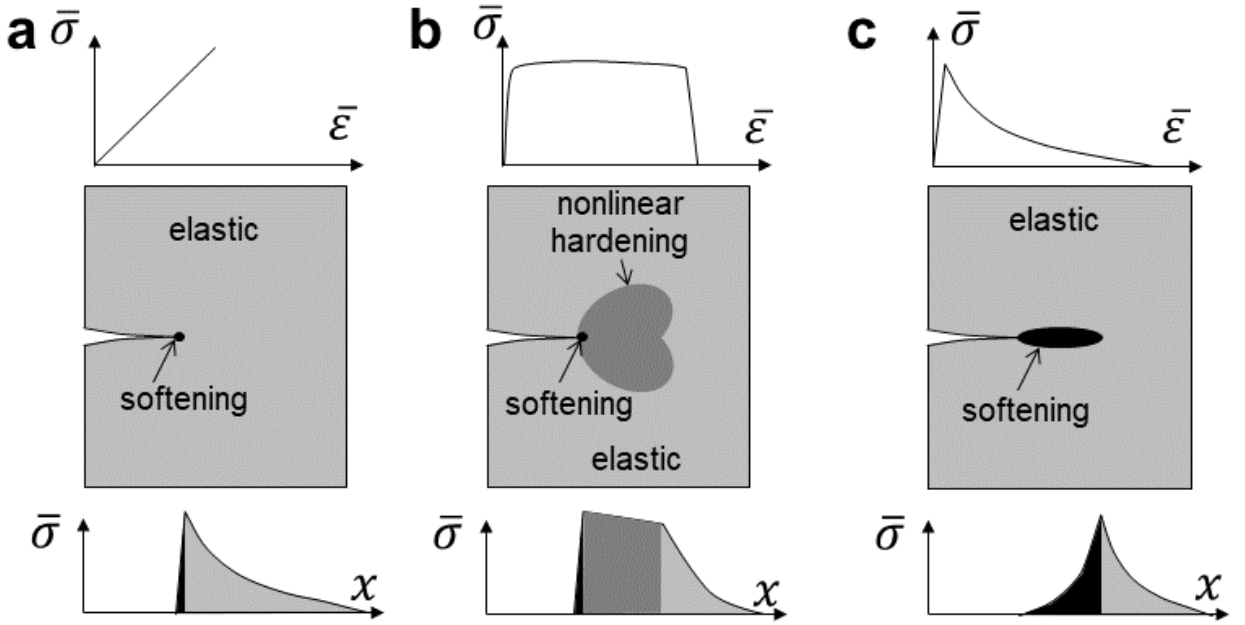

Figure 1.1: The emergence of the nonlinear zone in the crack front in elastic-plastic (ductile) (b) and in quasibrittle materials (c), compared with homogeneously brittle materials (a).

the breaking of the material takes place is still small. Many metals, especially various tough alloys, fall into this category. and its general type may be defined as ductile. This kind of behavior is best treated by a specialized branch of fracture mechanics–the elastic-plastic fracture mechanics [4], [5]. The third type of behavior (Fig.1.1c) includes situations in which a major volume of the nonlinear zone undergoes progressive damage with material softening, due to microcracking, void formation, interface breakages and frictional slips, and other similar phenomena (e.g., crystallographic transformation in certain ceramics). The zone of plastic hardening or perfect yielding in this type of behavior is often negligible, i.e., there is a rather abrupt transition from elastic response to damage. This happens for concrete, rock, ice, cemented sands, stiff clay, various ceramics with hard inclusion, fiber composites, wood particle board, paper, shale with arresting bedding plan, and many more materials. We call these materials quasibrittle because even if no appreciable plastic deformation takes place, the size of the FPZ is large enough to have to be taken into account in

calculations. A special case in which both nonlinear zones have non-negligible sizes will also be discussed.

1.2 Why crack-parallel stresses matter?

Depending on the type of nonlinear zone arising at the crack front, various methods have been used to compute the fracture energy of materials, including both experimental and numerical approaches. In many cases, the nonlinearity is condensed to the interactions between cracked surfaces. The crack is, therefore, represented by a zero-width interface (via a line or surface) within which any material behaviors are described based on the separation, normal contact and sliding motions. This approach, however, fails to consider the finite-size nature of the nonlinear zone in the crack front and reduces the number of relevant length scales to one, which is measured along the interface. Consequently, this approach completely ignores the interaction between the stress/strain components that are parallel to the crack and the microstructure in the nonlinear zone. Note that, due to the absence of any length scale in the EFM, these crack-parallel stresses would cancel each other due to the superposition principle and result in a more severe misrepresentation of the fracture energy.

In reality, crack-parallel stresses are important for many scenarios. The importance of considering a finite width of the FPZ is supported by futile experience with the cohesive crack modeling of size effect in shear failure of reinforced concrete beams and slabs, which has been a formidable problem for decades. A crack of nearly mode I type, driven by shear force, propagates in a stable manner through about 80% of the cross section depth, and the failure eventually occurs because of crack-parallel compression at the crack front (Fig.1.2a). Also, this stress may be the gross overestimation of the forces exerted by sea ice on the legs of oil platforms (Fig.1.2c). In another case, the increase of deviatoric stress state in shale may be the cause for the crumbling of materials ahead

of the tip (Fig.1.2b), leading to a more uniform pressure field in a hydraulic crack, which prevents the localization of parallel cracks.

The effect of crack-parallel stresses also have important implications on the validity of numerical models in the presence of damage and cracks. For example, two prime representatives of the modeling approach that idealizes fracture as zero-width interface are the cohesive crack method (CCM, introduced by Barenblatt in 1959 [6]) and extended finite element method (xFEM, introduced by Belytschko in 1999 [7]). These so-called line crack models do not include the crack-parallel normal strain ϵ_{xx} (as well as ϵ_{zz} and ϵ_{xz}) among the basic thermodynamic variables, and thus cannot take the crack-parallel normal stress σ_{xx} properly into account. As a zero-width FPZ (or the interface mentioned above) is considered, the effect of the crack-parallel normal stress σ_{xx} on the microstructure that happens at the continuum material points outside of this FPZ could be captured. Therefore, a FPZ of finite width must be modeled, reflecting its meso-scale physical behavior. The possibilities are a tensorial damage softening constitutive law coupled with crack band model (CBM) [8], the nonlocal models [9], or the lattice discrete particle model (LDPM) [10]–[12]. The CB model, however, must be accompanied by a sufficiently realistic damage model such as the microplane model, particularly its latest version M7 [13]. This speculation was confirmed by the capability of the CBM (with M7) [14]–[18] and the LDPM [19], [20] in capturing the correct behavior of the problem in Fig.1.2b. This experience is what partly inspired this thesis.

Despite the importance of these crack-parallel stresses in fully describing the fracture characteristics of materials, most of the existing experimental configurations have failed to include or capture them. Such an effect could not be captured because all standard notched fracture specimens (three-point-bend (3PB), single-edge-notched tension (SENT), circumferentially notched tension (CNT), compact tension (CT), double cantilever (DC), edge-notched eccentric compression, etc.; see Figs. 1.3a-f) have a negligible normal stress parallel to the crack. The wedge-splitting spec-

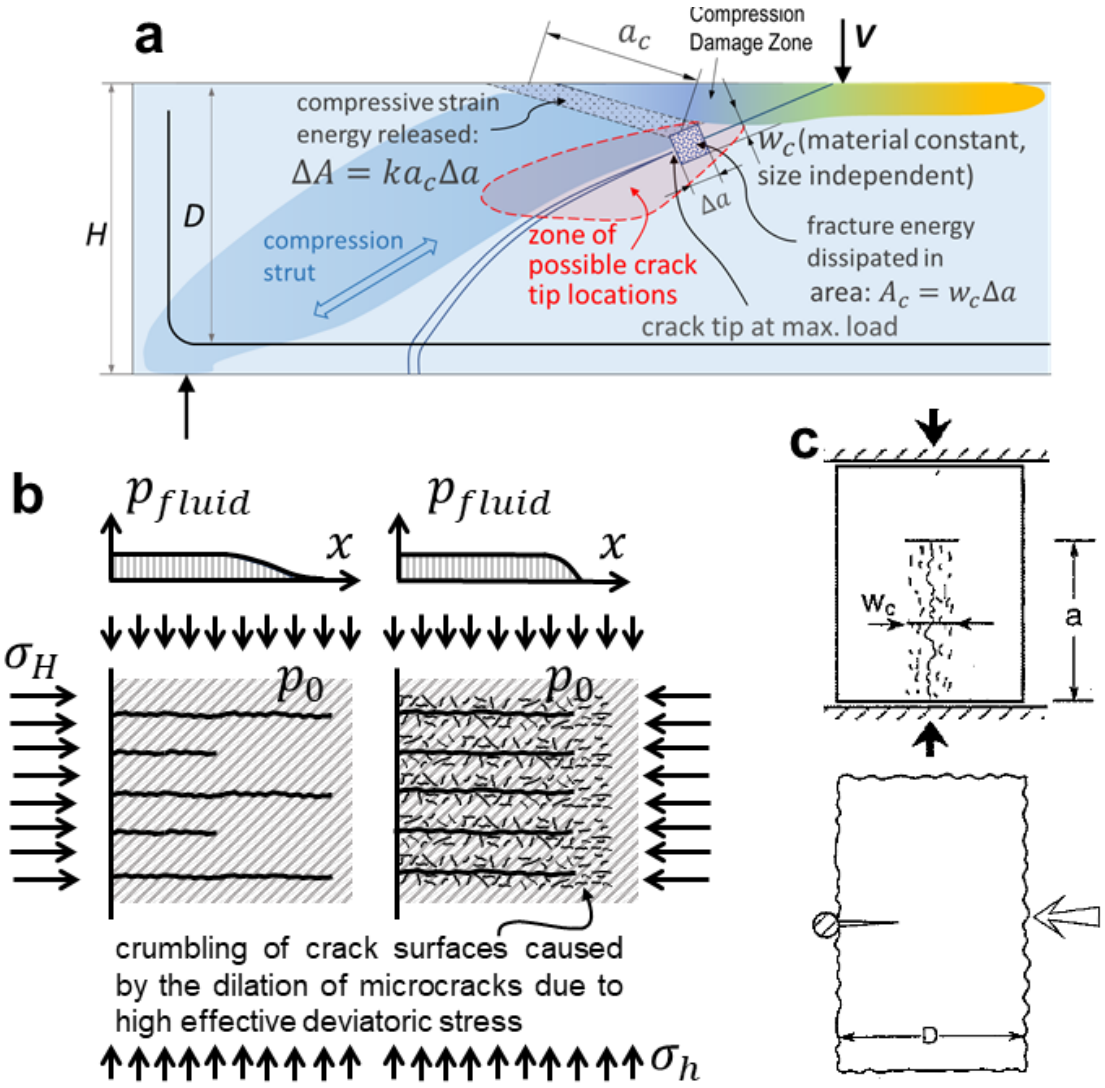

Figure 1.2: (a) A sketch of the mechanics governing the strength of scaled RC beams, reproduced from [21]; (b) The effect of the crack-parallel stress on the microcracks pattern leading to the difference in pressure profile; and (c) the fracture of sea ice near the legs of oil platforms.

imen (Fig.1.3g) might seem to be an exception, but the $|\sigma_{xx}|$ is insignificant compared with the uniaxial compressive strength, f_c, and such a stress is non-uniformly distributed throughout the specimens. In addition, cracks appear experimentally as lines (albeit rough), and it is obvious that a line cut in direction x in a specimen under homogeneous uniaxial stress σ_{xx} causes no stress

change in the classical EFM as already mentioned above.

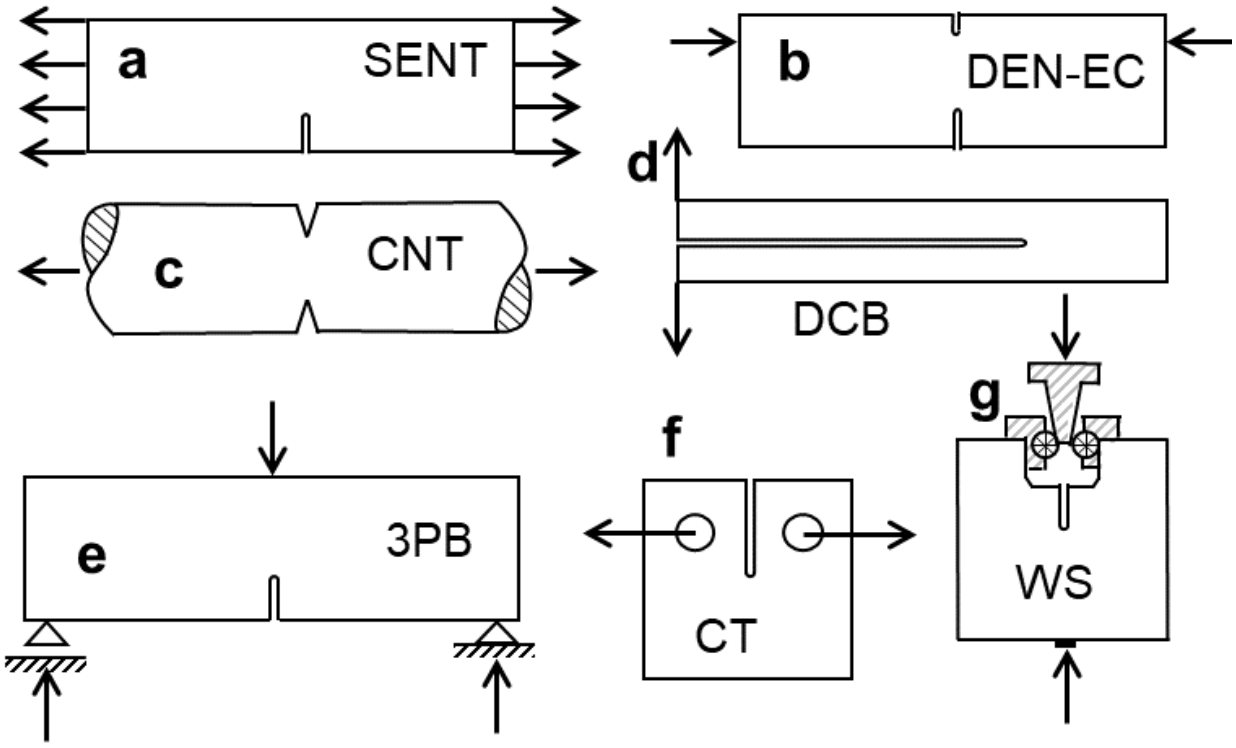

Figure 1.3: Standard notched fracture specimens that neglect the effect of crack-parallel stress.

On the other hand, experiments with non-negligible σ_{xx} have not been usually considered due to the complexity of applying additional loads, which leads to ambiguities in performing the tests and analyzing the results. In structural engineering labs, tests with multiple loads are, of course, commonplace, but they require the use of multiple hydraulic jacks, which introduce undesirable self-weight loads and lead to a statically indeterminate support system in which stress evaluation requires a damage constitutive law which may be well understood. Hydraulic jacks causing crack-parallel compression were used in 1995 by Tschegg et al. [22] in an elaborate modification of the wedge-splitting test. The results confirmed the hint from the 1987 microplane model that crack-parallel compression should matter. Despite a trend similar to this thesis was observed, several

ambiguities emerged, including the incapability to distinguish the effect of crack parallel stress on the total fracture energy and the initial fracture energy and the complexity of the stress field due to the weight of heavy clamping frames, and to friction under the jacks. Such a difference will be discussed next.

1.3 The non-uniqueness of the cohesive law and the importance of the scaling test in determining a unique fracture energy

In discussing the fracture energy, we must first clarify what kind. The typical softening stress-separation curve of concrete begins with a steep initial tangent, followed by a very long tail, as shown in Figs.1.4a,b. Accordingly, two fracture energies are distinguished: (a) the initial fracture energy, G_f, given by the area under the initial tangent, and the total fracture energy, G_F, representing the area under the complete softening curve, including its tail [14], [23]–[25]. Typically, $G_F/G_f \approx 2$ to 6 for concrete. The G_f alone governs the load capacity of most structures, while the G_F governs the energy absorption in dynamic failures such as impact. We note that the work-of-fracture method often used to determine the value of G_F gives ambiguous results [26], due to the FPZ size variation near notch tip and near opposite boundary; see Fig.1.4c. This can severely underestimate the steady-state energy dissipation and cause a major error. Therefore, the G_F suffers from high uncertainty unless the work-of-fracture tests are conducted at various specimen sizes [26].

Fortunately, unambiguous determination of G_f (and characteristic size c_f) from the present experiments and numerical simulations is made possible by the size effect method. This method [14], [27], embodied in the international standard recommendation of RILEM [28], endorsed recently by ACI-446 committee, and improved in [24], [25], [29], was devised in 1990 (and without c_f in 1987 [23]). It is an effective way to circumvent the impossibility of determining, optically or acousti-

cally, the precise location of the tip of a macroscopically equivalent EFM crack within the large FPZ of quasibrittle materials. In this method, based on asymptotic matching, it suffices to measure the maximum loads, P, of notched specimens of several sufficiently different sizes, preferably, but not necessarily, geometrically similar. The details of this method on both quasibrittle and ductile materials will be discussed in the next chapters.

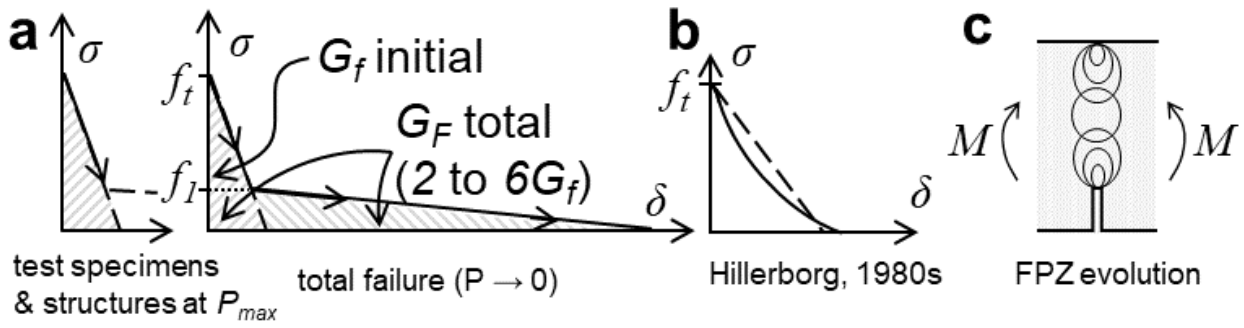

Figure 1.4: (a) A traction-separation curve without crack-parallel stress; (b) A linear approximation of the initial fracture energy; (c) The effect of the boundary on the fully developed FPZ, which leads to ambiguity in the work-of-fracture and the G_F measurement.

1.4 T-stress in metal–the current progress

Unlike quasibrittle materials, the effect of σ_{xx}, called the T-stress, was long considered in fracture of plastic metals [30]–[33]. Important studies on the size and behavior of the YZ with respect to Q (or T) have been supported by extensive finite element analyses, but not experimental efforts. In particular, O'Dowd and Shih [30], [31] proposed the concept of J-Q-annulus surrounding the crack tip, in which the J-integral characterizes the remote stress field corresponding to a $-1/2$-power stress singularity, while Q corresponds to the second, non-singular, term of the near-tip asymptotic expansion, which represents a uniform stress field of crack-parallel T-stress. Triaxiality of stress state in a tip-surrounding annulus, described by this parameter Q as the relative difference between

stress fields when T is not zero and when T vanishes, led to a monotonic increase of the critical J-integral value based on the Hutchinson-Rice-Rosengren (HRR)[4], [5] field. This stress was shown to act as a crack tip constraint, suppressing cleavage.

The J-Q concept, however, has not been extended to a simple analytical scaling law, which makes the measurement more complicated. Similar comments apply to the studies of Betegón and Hancock [32], Xia, Wang and Shih [34], and Gao, Shih, Tvergaard and Needleman [35]. The apparent question on whether T-stress will affect the form of the scaling law and the size of the YZ, therefore, remains unanswered.

It should be noted that, in the field of metals, the term "size effect" has been applied to a variety of different phenomena. E.g., the well-known Hall-Petch effect [36]–[38] is not a size effect on structure strength but the effect of grain-size on the yield strength of metal, explained by dislocation arrest at grain boundaries. In crystal plasticity, the term is used for the strength variation of miniaturized single-crystal specimens [39]. The term has also been used for the effect of geometrically necessary dislocations and of strain gradients on the yielding strength of metals. Further the term has been used for the increase of specific cutting force with a decreasing depth of a cut [40].

In addition, these T-stresses that have been studied emerge intrinsically at the crack tip due to the constraint caused by either the geometry of specimens or the loading configuration. The impact of externally applied in-and-out-of-plane crack-parallel stresses (i.e. the extrinsic effect) has not been studied yet.

CHAPTER 2

SIZE EFFECT METHOD AND THE EFFECT OF CRACK PARALLEL STRESSES ON QUASIBRITTLE MATERIALS

2.1 Scaling of structural strength for quasibritlle materials

As mentioned in the previous chapter, the classical methods to measure fracture energy, including the work-of-fracture method, are applied only to one size, which suffers from high uncertainty. Therefore, the size effect method is used to compute the initial fracture unambiguously [26]. In the classical theories based on plasticity or limit analysis, the strength of geometrically similar structures is independent of the structure size. As already pointed out [41], however, concrete structures and, in general, structures made of brittle or quasibrittle materials, do not follow this trend. In this section we first define what is understood by the strength and size of a structural element and then examine how the strength depends on the size. To observe the size effect, the strength of geometrically similar structures of different sizes are compared. It is conveniently characterized in terms of the nominal strength, σ_{Nu}, representing the value of the nominal stress, σ_N, at maximum (ultimate) load, P_u. The nominal stress serves as a load parameter and may, but need not, represent any actual stress in the structure, which can be defined as: $\sigma_N = P/bD$ when the similarity is two-dimensional or as P/D^2 when the similarity is three-dimensional; b = thickness of a two-dimensional structure, and D = characteristic dimension of the structure, which may be chosen as any dimension, e.g., the depth of the beam, or the span, or half of the span, since only the relative values of matter. The nominal strength is then $\sigma_{Nu} = P_u/bD$ or P_u/D^2.

Since crack growth in EFM is defined by the condition $\mathcal{G} = G_f$ = or $K_I = K_{Ic}$, we need to

know the structure of the equations for K_I and $\mathcal{G}$ if we want to investigate the influence of the size. And since size effect is one of the main topics of this book, it is also convenient to define the conventional forms of the equations we are going to use so that the size D is made explicit. Systematization of the presentation of the existing results also requires using general mathematical forms of the equations for K_I and $\mathcal{G}$, so that a single experimental or numerical result may be used for any similar specimen or structure. To determine the general form, we consider a family of geometrically similar structures subjected to the same type of loading (for example, the center cracked panel in Fig. 2.1a. Let D be a characteristic dimension (for example, the panel width) to which all the remaining dimensions are proportional (for example, the height-to-width ratio), except for the crack-to-depth ratio a/D, which is free to vary. The purpose of the analysis is to obtain the general expression for K_I and $\mathcal{G}$ showing explicitly the dependence on the variables P (or σ_N), D and $\alpha = a/D$.

The early researchers on concrete fracture often attempted to apply EFM directly to evaluate the fracture tests. In this case, the fracture toughness K_{Ic} is calculated from the peak load P_u (or the nominal strength σ_{Nu}) using the EFM formula for a propagating crack in a specimen. If the geometry is so-called positive (K_I at constant load increasing with the crack length, or $\partial K_I/\partial a$), the onset of crack extension coincides with the peak load and :

$$K_{Ic} = \sigma_{Nu}\sqrt{D}k\left(\alpha_0\right) \tag{2.1}$$

where α_0 is the relative initial crack depth (usually the notch depth in concrete). The condition of positiveness of the geometry is the same as $k'\left(\alpha_0\right) > 0$, where the prime indicates the derivative. Most of the specimens used in fracture testing have positive geometry. It turned out, however, that the toughness values thus determined were not invariant with respect to the beam size, shape, or notch depth. This means that Eq. 2.1 did not supply the true fracture toughness, but an apparent

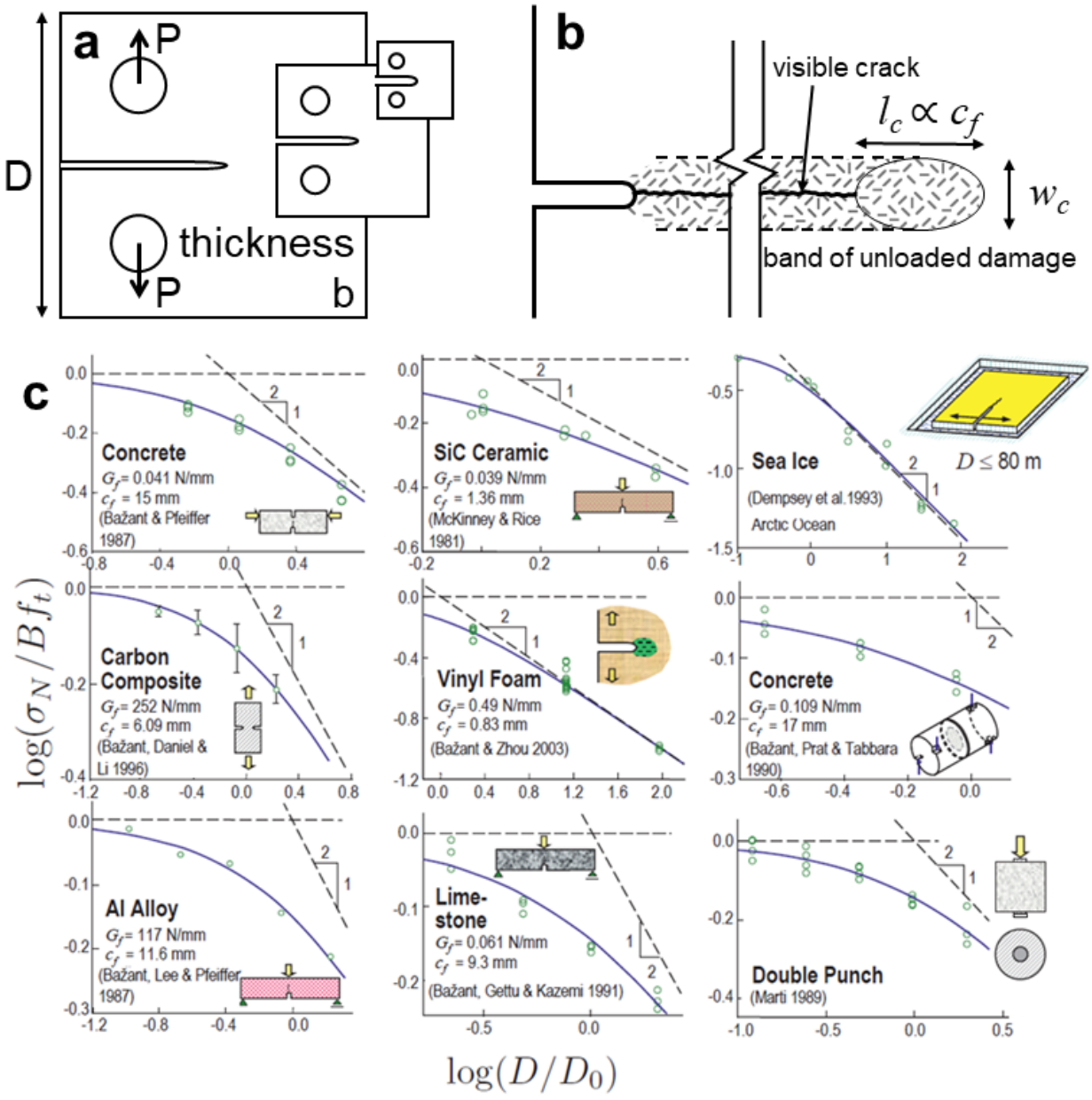

Figure 2.1: (a) Geometrically scaled compact-tension specimens; (b) The FPZ with finite length and width; and (c) The applicability of the size effect method on different quasi-brittle materials and on different configurations, reprinted with the authors' permission [21].

fracture toughness that varied with testing conditions. To emphasize this fact, we use in this book a special notation for the apparent fracture toughness: first, we define the nominal stress intensity factor K_{IN} as the stress intensity factor computed for the actual load and the initial crack length, i.e.,

$$K_{IN} = \sigma_N \sqrt{D} k\left(\alpha_0\right) \tag{2.2}$$

Then, the apparent fracture toughness K_{INu} is defined as the value of KIN at peak load:

$$K_{INu} = \sigma_{Nu} \sqrt{D} k\left(\alpha_0\right) \tag{2.3}$$

Eq. 2.3 is nearly identical to Eq. 2.1, but the conceptual difference is huge: K_{Ic} in Eq. 2.1, must be a material property, independent of testing details; K_{INu} need not. Of course, for positive geometries:

$$K_{INu} = K_{Ic} \tag{2.4}$$

Let us now examine how the apparent toughness K_{INu} deviates from the EFM prediction. For a large, but not infinitely large specimen, we use the definition of critical equivalent crack and write the condition that the stress intensity at peak load for the equivalent crack must be the true fracture toughness, i.e.

$$K_{Ic} = \sigma_{Nu} \sqrt{D} k\left(\alpha_{ec}\right) \Rightarrow \sigma_{Nu} = \frac{K_{Ic}}{\sqrt{D} k^2\left(\alpha_{ec}\right)} \tag{2.5}$$

Now, recalling that all our reasoning in the preceding sections refers to a specimen much larger than the fracture process zone, we see that $\Delta a_{ec} \approx c_f \ll D$; see Fig. 2.1b. Because $\alpha =$

$\alpha_0 + \Delta a_{ec}/D$, we may use a two-term Taylor expansion for $k^2(\alpha)$:

$$k^2(\alpha_{ec}) = k^2(\alpha_0) + 2k(\alpha_0)k'(\alpha_0)\frac{c_f}{D} = k_0^2 + 2k_0k_0'\frac{c_f}{D} \text{ as } \frac{c_f}{D} \to 0 \tag{2.6}$$

Substitution of Eq. 2.6 into Eq. 2.5, followed by series expansion of the result, leads to the asymptotic two-term expression:

$$\sigma_{Nu} = \frac{K_{Ic}}{\sqrt{k_0^2 D + 2k_0k_0'c_f}} = \frac{K_{Ic}}{\sqrt{2k_0k_0'c_f}\sqrt{1 + D/\left(2k_0'c_f/k_0\right)}} = \sqrt{\frac{E'G_f}{g_0'c_f + g_0 D}} \tag{2.7}$$

where $g_0 = k_0^2$, $g_0' = 2k_0k_0'$. If we set $Bf_t = K_{Ic}/\sqrt{g_0c_f}$ and $D_0 = g_0'/g_0c_f$:

$$\sigma_{Nu} = \frac{Bf_t}{1 + D/D_0} \tag{2.8}$$

This form can be turned into the linear form:

$$Y = AD + C;\ Y = 1/\sigma_{Nu}^2,\ C = 1/(Bf_t)^2,\ A = C/D_0 \tag{2.9}$$

The fracture energy G_f and the characteristic size c_f can be computed:

$$K_{Ic} = k_0/\sqrt{A},\ G_f = k_0^2/E'A,\ c_f = k_0/2k_0'C/A \tag{2.10}$$

The performance of size effect method has been shown in Fig. 2.1c.

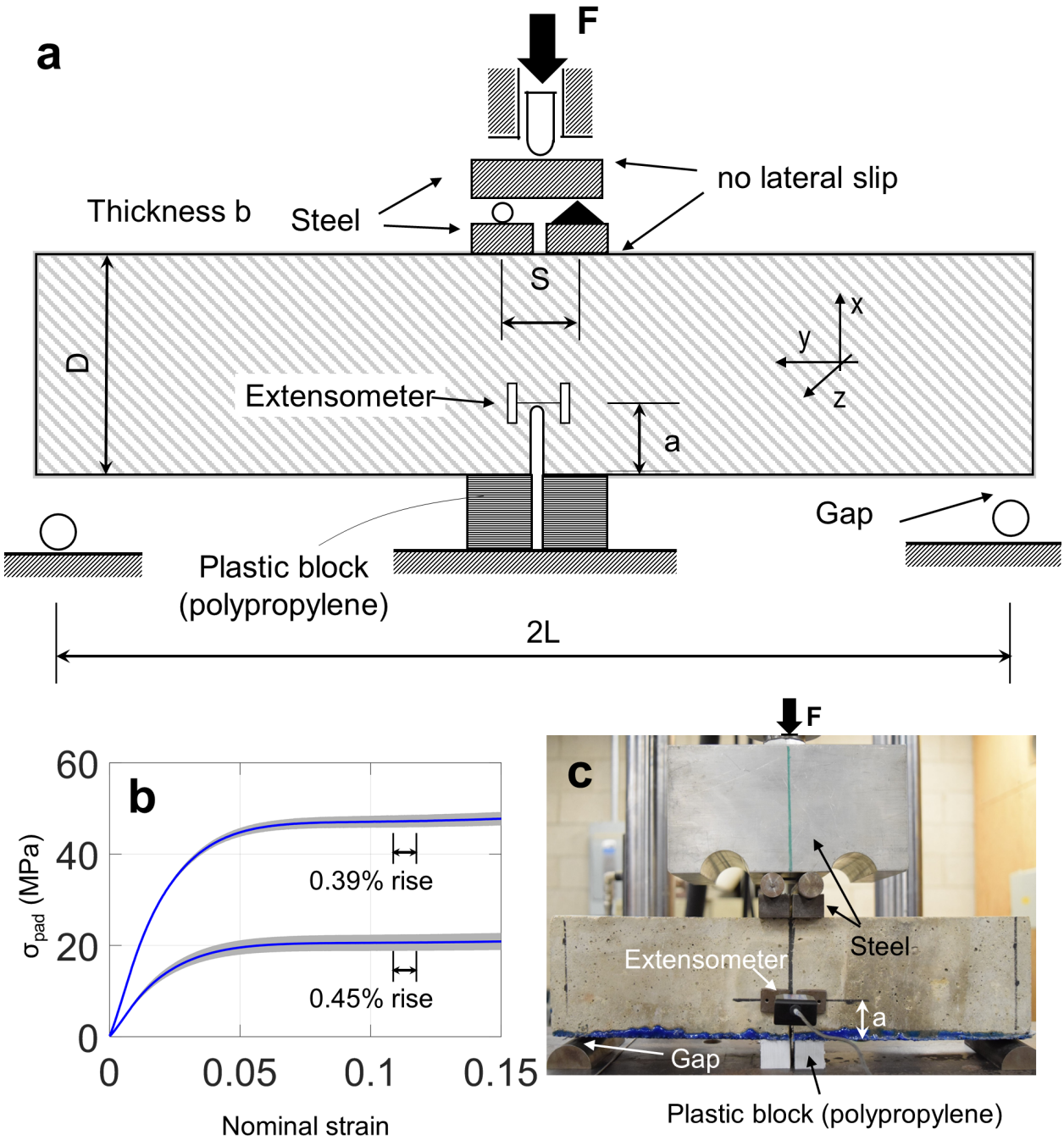

Figure 2.2: (a) Schematic experimental set-up (with coordinates x, y, z); (b) Real set-up; and (c) Stress-strain behavior of plastic pad corresponding to two values of tested σ_{xx} (note that only a short segment of the quasi-plateau intervened during the rise of bending moment

2.2 Gap test - a new setup to investigate the effect of crack-parallel stress on the fracture energy of materials

To investigate the effect of crack-parallel stresses on the material fracture energy, a novel, yet simple, gap test [42], depicted in Fig. 2.2a, has four key features:

1) A pair of compressible pads (Fig. 2.2a,b) capable of nearly perfect plastic yielding (Fig. 2.2c) is installed next to the notch mouth to produce notch-parallel compression of desired magnitude (Fig. 2.2c), with no bending moment (Fig. 2.3a-i).

2) Rigid supports at beam ends are installed with a gap (of about 2 to 4 mm) so as to engage in contact and apply the crack-producing bending moment (Fig. 2.2a,b) only after the pads start plastic yielding (Fig. 2.3a-ii,iii).

3) This way the test beam passes from one statically determinate system to another, which makes evaluation simple and unambiguous.

4) The static determinacy of loading and the constancy of crack-parallel compression make it possible to use the size effect method, which is an easy and robust way to measure G_f, with its dependence on σ_{xx}.

The deflection relative to the end supports causes the load-deflection curve to rise above the yield plateau, peak and then descend back to the plateau, as seen in Fig. 2.3b. The area between this up-and-down curve is the energy dissipated by fracture, which is exploited in the work-of-fracture method of measuring fracture energy. However, only the peak loads, for several different specimen sizes, are needed to determine G_f; Fig. 2.3c. Typical measured curves of load P versus load-point displacement u, and of P versus the crack tip opening displacement, δ_{CTOD}, are shown for D = 101.6 mm in Fig. 2.3b,c.

The statical determinacy of the beam when the pads are yielding is gained from the constancy

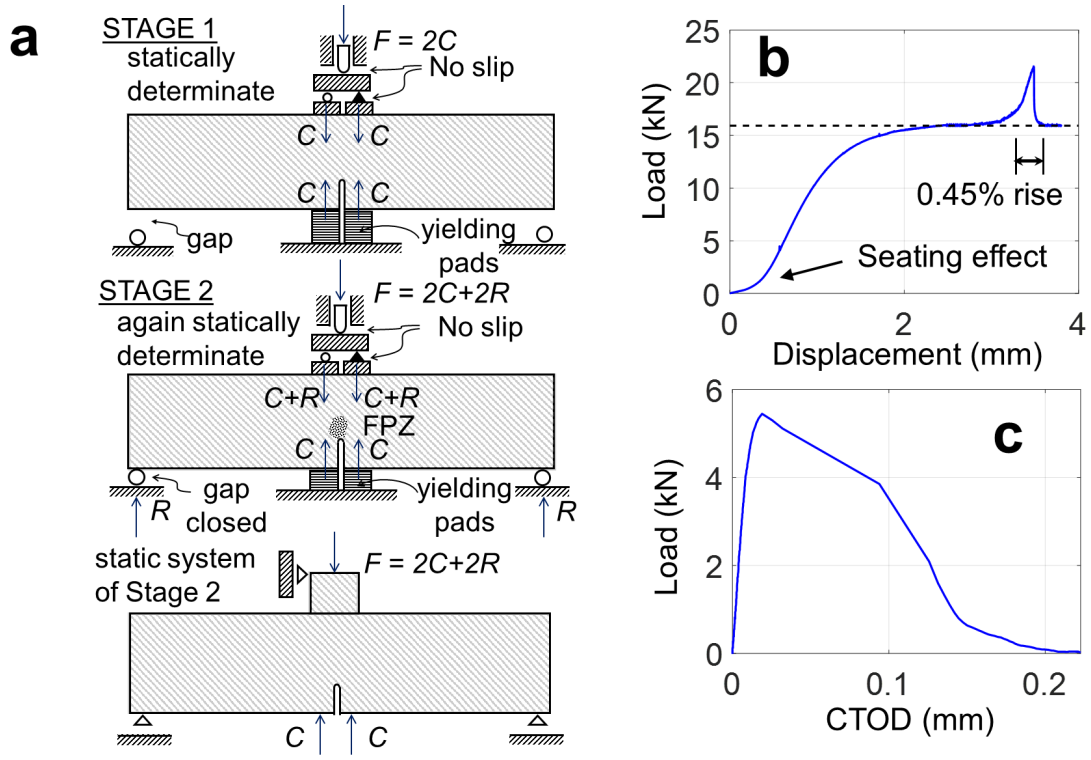

Figure 2.3: (a) Experimental procedure; (b) A load-machine displacement behavior (note that within the segment F, which is what matters for G_f, the change in pad reaction (dashed line), is negligible); and (c) Extracted load-CTOD.

of the reactions of the pads. It makes the pad reactions equivalent to applied dead loads. Hence, after the pads begin to yield, there is again three-point bending, in which the deformation of the beam cannot break symmetry of the left and right halves of the beam, even in postpeak softening. Therefore, any small initial imperfection (such as a small Mode II component) must remain small, i.e., there is no equilibrium path bifurcation. The magnitude of the yield force is controlled by the area of the pad. Smaller yield forces are obtained by drilling holes in the pads.

2.3 Further aspects and details of the gap test

The size effect method, a robust and simple method developed in (1990) [27], is what allows identifying G_f from the maximum load of fracture specimens of different sizes. Based on the Type 2 (energetic, non-statistical) size effect law of quasibrittle fracture [14], [15], [27], [43]–[45], it has been adopted as an international standard recommendation [28], and endorsed by ACI-446 [46]. It has become the most widely used method for testing G_f of concrete and geomaterials. One advantage is that it necessitates measuring only the maximum loads, P_{max}, postpeak being superfluous, but P_{max} must be measured for at least three sufficiently different specimen sizes [27] (preferably, but not necessarily [14] scaled geometrically). As another advantage, the identification of G_f, along with the material characteristic length c_f, is reducible to linear regression. Importantly, the derivation of this method [14], [27] is not affected by the crack-parallel stress, neither in-plane σ_{xx} nor anti-plane σ_{zz}.

The test specimens are analyzed as four-point-bend beams, although the two center-span loads are spaced so closely that the beams are almost equivalent to the standard three-point bend beams. To keep the evaluation simple, the separation of center span loads was scaled with the beam size D.

Beams of three depths D = 101.6 mm (4 in.), 203.2 mm (8 in.) and 406.4 mm (16 in.), measured from top face to the bottom face, were tested. The span-to-depth ratio was $2L/D$ = 3.75, and notch depth ratio a/D = 0.3. The beam thickness was 101.6 mm for all sizes. The beams were scaled geometrically in two dimensions (2D). Normal concrete with mean cylindrical compression strength f_c = 40.5 MPa was used. The maximum aggregate size was d_a = 18 mm. The notch width was 3 mm, which is known to be well within the admissible range compared to d_a.

The negative bending moment caused by self-weight before the pads engage is negligible (for

the heaviest beam, $< 3\%$ of the maximum bending moment). A small restraint against rotation ensures stability before the end supports engage [47]–[49].

The pads consist of a layer of polypropylene. Once plasticized, its tangential hardening shear modulus μ is very small, about 20 MPa (see Fig. 2.2c) (it must be nonzero, or else the plastic would escape from the pads like a fluid). During plastic compression, the polymer behaves as incompressible. The compression causes the polypropylene to be laterally squeezed out, though imperceptibly so. The lateral squeezing governs the tangential hardening stiffness H of the yielding pads, which is also very small but nonzero. The pair of elasto-plastic pads is placed next to the notch mouth (Fig. 2.2a), and a pair of symmetric loading pads on the opposite beam face. Fig. 2.2c documents that the measured load-deflection diagram of the pads exhibits a long near-horizontal yield plateau. To lower the value of the tangential pad stiffness, H (with limited shortening of the yield plateau), regularly spaced holes are drilled through the pads (this also reduces the elastic stiffness); Fig. 2.2c.

To prevent shear failure of concrete under the elasto-plastic pads, a 2 mm laminate layer has been glued to the concrete surface, and it has been calculated that its effect on the stress intensity factor is negligible. The loading rate is scaled so as to reach the maximum load within approximately the same time. An extensometer crossing the crack tip is used to measure the crack tip opening displacement, δ_{CTOD} (Fig. 2.2a or 2.3a). The complete set-up is seen in Fig. 2.3b.

Compression stiffness of plastic pads and their optimization

For simplicity, consider a circular pad with radius r and polymer layer thickness h (Fig. 2.4). In the plastic regime, we assume the polymer is incompressible and has a very small but non-zero shear modulus μ (if μ were zero, the plasticized polymer would flow out). The boundaries of the layer are confined and behave as rigid. Volume conservation in the disc of radius $x \leq r$ requires that

$\pi x^2 w - 2\pi shu$ where w - relative displacement of decrease of thickness and u - average increase of radius x. Hence $uwx/2h$. Given that the polymer does not slide on the layer surfaces, we may assume the radial displacement profile across layer thickness to be parabolic Fig. 2.4). In that case, the maximum displacement is $1.5\times$ higher than u, the mean, and thus the profile of shear angle is $ga = \partial u/\partial y = 3wxy/h^3$, where y is the transverse coordinate. The strain energy density with respect to radial coordinate x then is $\bar{W}(x) = 2\int_0^{h/2} \mu\gamma^2/2\mathrm{d}y = 3\mu w^2 x^2/8h^3$. Conservation of energy requires the work of compression of the layer by w to equal the strain energy increment of the whole layer, i.e., $W = Hw^2/2 = \int_0^r \bar{W} \cdot 2\pi\, \mathrm{d}x$ where H = compression stiffness of the layer. Integration yields:

$$H = k_p \mu A^2/h^3, \quad k_p = 3/8\pi \tag{2.11}$$

where $A = \pi r^2$ = area of the pad. This equation may also be used as an approximation for a square pad of the same area (an accurate solution is more complicated). The pads should be shaped so as to minimize H (subject to Haringx's critical load formula [50] for shear buckling governing the elastomeric bearings of bridges), or minimizing A, which means replacing one pad with several small ones (or drilling big holes). Haringx's formula gives the critical ratio $\lambda_{cr} = \sqrt{A}/h$ for buckling.

Second, let us analyze an elongated $l \times L$ rectangle (the pad in Fig. 2.4), with $L \gg l$, approximately in 1D, coordinate x. Due to incompressibility, the axial strains are distributed as $u = (w/h)x$, and the strains are $\gamma = (6u/h^3)y$. The work per unit length in x is $\bar{W} = 2\int_0^{h/2} \frac{1}{2}\mu\gamma^2 \mathrm{d}y = 3\mu w^2 x^2/2h^3$. By integration, $W = 2b\int_0^{l/2} \bar{W}\mathrm{d}x = b\mu w^2 l^3/8h^3$. Setting $W = \frac{1}{2}Hw^2$, we get

$$H/L = (\mu/4)(l/h)^3 \tag{2.12}$$

The same formula approximately applies to an annular pad with internal and external radii $r_1 m r_2$

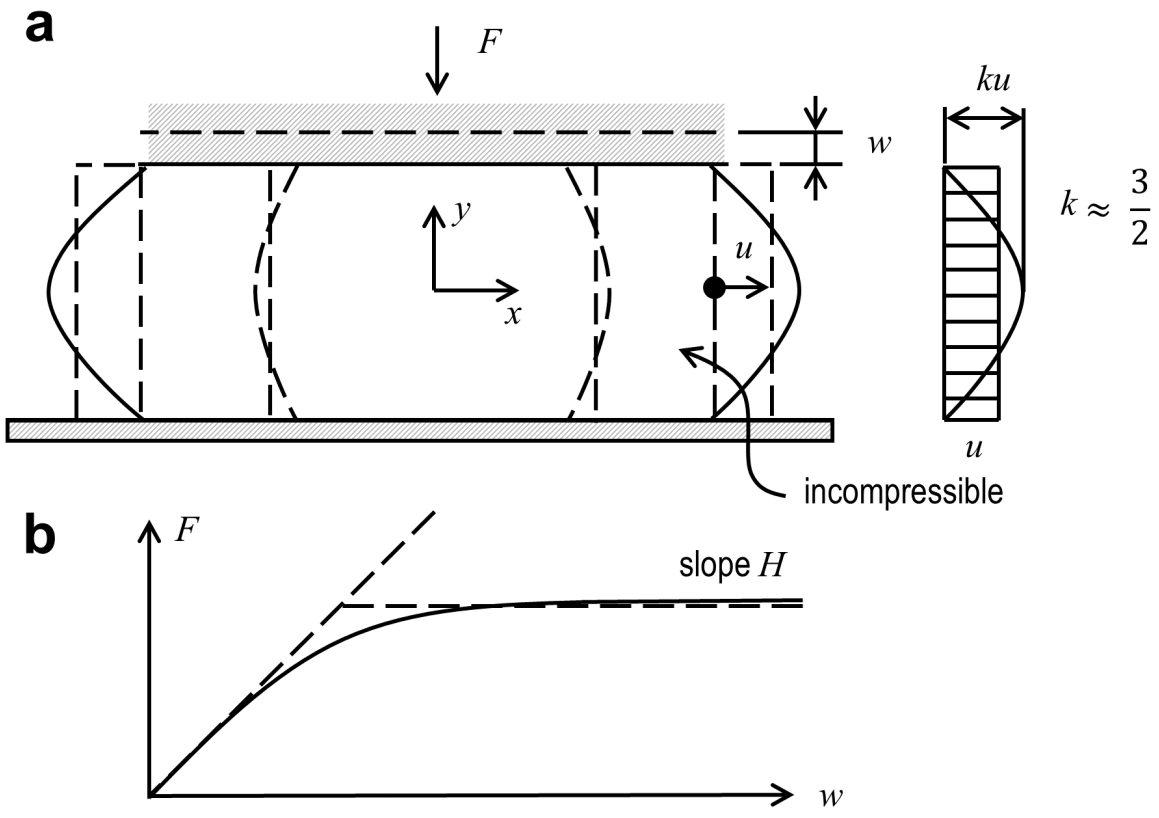

Figure 2.4: (a) A circular plastic pad under compressive force; and (b) The shape of the pad should be designed to minimize H.

provided that $l = r_2 - r_1 < r_1/4$. It also roughly applies to a pad with many sufficiently big regularly spaced holes (Fig. 2.4) of radius r provided that approximately $\sqrt{A/A_s - 1} < 1/4$ where A = total area and A_s = area of the holes. If $> 1/4$, one can interpolate. Other polymers, e.g. polyethylene, PDMS, can be also used to get a different μ. A possible alternative to the plastic pads are blocks of perfectly plastic metal, e.g., tin (Sn).

2.4 Functions for stress intensity factor and energy release rate of the gap test

To determine G_f, one needs the LEFM stress intensity factor, K_I [14], [27]. Although the load configuration is close to 3-point bending, four-point-bending with a small but finite distance between the loads gives better accuracy (Fig. 2.2c). According to [51]:

$$K_I = \sigma_N \sqrt{D} k(\alpha) \quad \text{where} \quad \sigma_N = P/bD \ (\alpha = a/D) \tag{2.13}$$

$$k(\alpha) = \frac{1.1682(2l - s)\sqrt{\pi\alpha}}{8\beta^{3/2}} \left(5 - 10\alpha/3 + \alpha^2 + 40\alpha^2(1-\alpha)^6 + 3e^{-6.134\alpha/(1-\alpha)}\right) \tag{2.14}$$

where P = total load (sum of two loads) applied at center-span, σ_N = nominal strength of beam; $2L$ = span between the supports, S = distance between the two center-span loads; $l = L/D, s = S/D$; b, D = thickness and depth of beam; a = crack (or notch) length, $\alpha = a/D$ = relative crack length; σ_N = nominal bending strength of each size; $f(\alpha)$ = dimensionless stress intensity factor. The size effect law (SEL) reads:

$$\sigma_N = B f_t (1 + D/D_0)^{-1/2} \tag{2.15}$$

$$1/\sigma_N^2 = (1/B^2 f_t^2 + D/B^2 f_t^2 D_0) \ \Rightarrow \ Y = C + AD \tag{2.16}$$

For data fitting, the SEL may be converted to a linear regression plot of $1/\sigma_N^2$ versus D as in 2.16 [14], [52]. To determine the size effect parameters, we need not only $k(\alpha)$ but also its derivative [14], [27]:

$$
\begin{aligned}
k'(\alpha) = \frac{\mathrm{d}k(\alpha)}{\mathrm{d}\alpha} &= \frac{0.8411(2l-s)\sqrt{\pi}}{8(1-\alpha)^{3/2}\sqrt{\alpha}}\left(5-10\alpha/3+\alpha^2+40\alpha^2(1-\alpha)^6+3\,e^{-6.134\alpha/(1-\alpha)}\right)\\
&+\frac{2.523(2l-s)\sqrt{\pi\alpha}}{8(1-\alpha)^{5/2}}\left(5-10\alpha/3+\alpha^2+40\alpha^2\beta^6+3\,e^{-6.1342\alpha/(1-\alpha)}\right)\\
&+\frac{1.6823(2l-s)\sqrt{\pi\alpha}}{12(1-\alpha)^{3/2}}(-5+3\alpha+120\alpha((1-\alpha)^6-360\alpha^2(1-\alpha)^5\\
&-27.6(1/(1-\alpha)+\alpha/(1-\alpha)^2)\,e^{-6.134\alpha/\beta})
\end{aligned}
\tag{2.17}
$$

Upon rearranging Eq. (2.15) as linear regression and fitting maximum load data, Eq. (2.16), the fracture energy and the characteristic material length (roughly 40% of actual FPZ length) can then be computed from [14], [27]:

$$G_f = K_f^2/E, \quad K_f = Bf_t\sqrt{D_0}k(\alpha_0) \tag{2.18}$$

$$c_f = \frac{D_0 k(\alpha_0)}{2k'(\alpha_0)} \tag{2.19}$$

Note that the crack-parallel compression is not a parameter in LEFM, and so, in LEFM, it cannot affect function $k(\alpha)$ and the equations relating G_f and c_f to $k(\alpha)$.

2.5 Concrete mix design and dimensions of tested specimens

To minimize the scatter of mechanical properties, all the specimens were cast within a few hours from the same batch of concrete delivered by a ready-mix supplier (Ozinga co.). Normal concrete of specific compression strength f_c' = 27.58 MPa (4000 psi) at 28 days of age was used. The slump range was 7.62–12.70 cm ($3.00-5.00$ in.), and the specific air content 0–3%. In the mix, one cubic

yard contained 470 lb. of cement (ASTM C150, 100 lb. of blast-furnace slag (labeled C989), 1750 lb. of coarse aggregate (ASTM C33#67), 1500 lb. of fine agreegate (ASTM C33#2); water-cement ratio w/c = 0.45.

The specimens for material characterization and model calibration include: cylinders for compression tests of diameter 101.6 mm and length 203.2 mm; square prisms for compression tests of side 76.2mm and length 152.4 mm; cylinders for splitting tests of diameter 101.6 mm and length 203.2 mm; and prisms for splitting tests of side 76.2 and length 152.4 mm. The beams for fracture tests, geometrically scaled, were of three sizes; small: $101.6 \times 101.6 \times 406.4$mm; medium: $101.6 \times 203.2 \times 812.8$ mm; and large: $101.6 \times 203.2 \times 812.8$ mm. The notch/depth and span/depth ratios were a/D = 0.3 and $2L/D$ = 3.75, respectively. For tests with various crack-parallel pressures, the beam dimensions were $76.2 \times 101.6 \times 406.4$ (all dimensions were in mm). The elasto-plastic loading pads had sides S of ratio S/D = 1/4 (Fig. 2.2a). All the specimens were test within 3 weeks, but the effect if this age difference on the degree of hydration and strength was negligible since the specimens were 1 year old. The specimens were all cured in a fog room until the time of test.

2.6 Material calibration results

Aside from the results of the gap tests for different specimen sizes at zero σ_{xx}, the properties of concrete were calibrated by tests of uniaxial compression of cylinders and prisms Fig. 2.5a,b. These calibrations are sufficient for M7 to characterize the behavior of normal concrete, which was validated by Brazilian splitting tests on both cylinders and prisms (see Fig. 2.5c, where the error bars indicate one standard deviation based on 4 tests for each case). The same model was utilized to predict the results of the gap test at non-zero σ_{xx}. For uniaxial compression, the specimens were capped with sulfur to make sure the loaded surface would be flat and almost frictionless. Linear

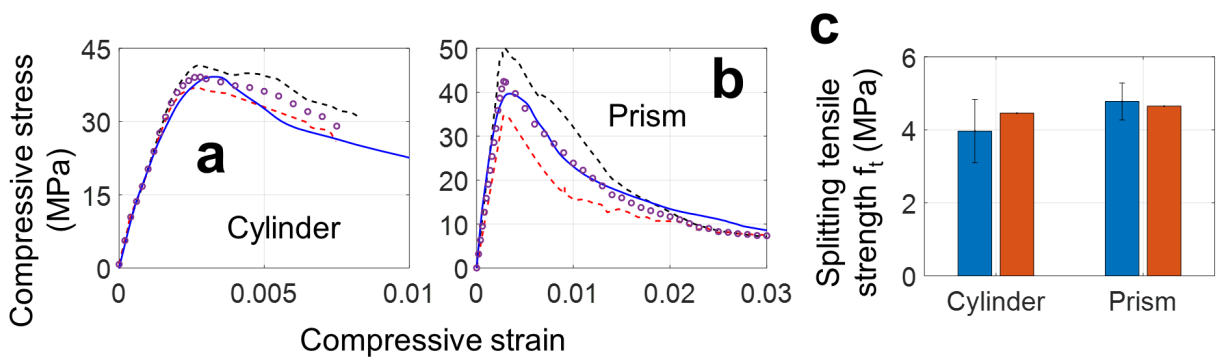

Figure 2.5: Calibrations and validations to obtain parameters for M7-CBM: (a) Uniaxial compression of cylinders; (b) Uniaxial compression of square prisms; and (c) Brazilian splitting tests.

Variable Differential Transformers (or LVDT) were used to record two crack-parallel displacements, as well as one lateral displacements used to control the loading, see Figs. 2.5a,b (ASTM C39). In the Brazilian tests (Fig. 2.5c), the loading strip was 12.7 mm wide and the samples were held in place at the beginning by a mild pressure (ASTM C496). The uniaxial tests of specimens of both types were conducted in the Tinus Alson frame with maximum load of 1000 kips, and the Brazilian split experiments the MTS loading frame of capacity 50 kips, both at the loading rate of 0.00635 mm/sec. Every test took for approximately ≈ 0.5 hour.

Fig. 2.5 shows the results on uniaxial compression strength of cylindrical and prismatic specimens (Figs. 2.5a,b) and their corresponding Brazilian splitting tensile strength (Fig. 2.5c). In Fig. 2.5a,b, the dashed curve shows the upper and lower envelope of data from three tests, whose average is represented by the dotted curve. This result is consistent with the average strength f_c' = 42.74 MPa reported by concrete supplier. Optimum fits of these results were obtained with the microplane constitutive model M7 [13], [53] shown by solid curves. The M7 was implemented in Abaqus using the crack band model with element size 12 mm. The dotted and solid curves are consistent and serve to indicate the level of compression on notched beams.

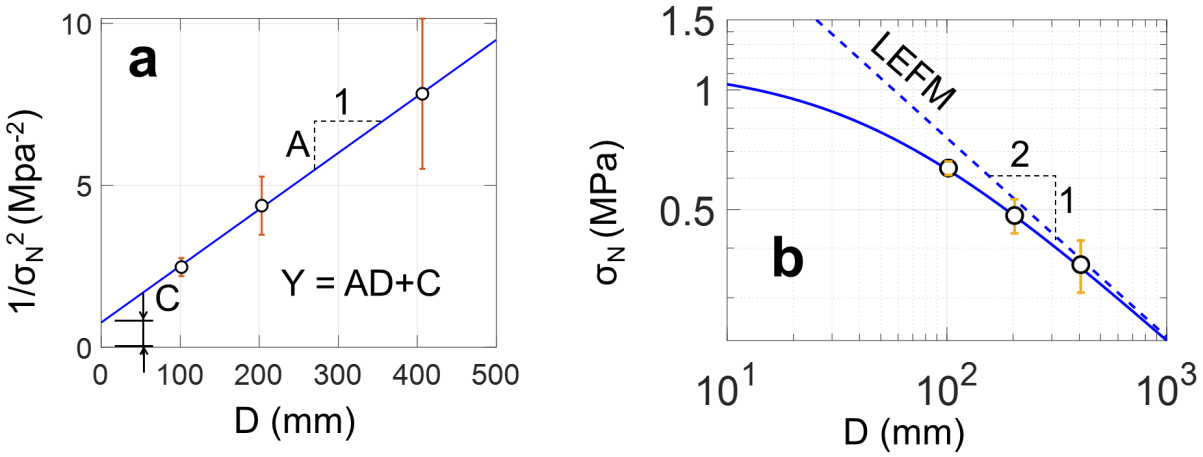

Figure 2.6: (a) Linear regression of size effect method and (b) The size effect curve plotted in log-log scale.

2.7 The effect of crack-parallel stress on G_f

Each of the three data points for different σ_{xx} has been obtained by linear regression of experiments on three sizes (see Fig. 2.6) and shown as the empty circles in Fig. 2.7a, . The coefficients of variation of the regressions (i.e., the root-mean-square of the deviations from the regression line divided by the data mean) were only 0.087%, 0.113%, 0.211%. These data points represent the effective values of fracture energy G_f as a function of three levels of compression stress σ_{pad} applied at the yielding pads. These experimental results reveal an important fact—G_f is not constant but depends on σ_{pad}, in fact, strongly. This raises doubts about the applicability of both the LEFM and the CCM, each of which requires constancy of G_f.

To get the effective G_f as a material property, σ_{pad} must be transformed to the crack-parallel normal stress σ_{xx} at the at the notch tip. FE analysis was used to get the ratio $r_c = \sigma_{xx}/\sigma_{pad}$. Elastic analysis gave $r_c = 0.962$, while crack band finite element analysis with M7 gave $r_c = 0.942$ for medium samples. The elastic values is seen to be a good enough approximation, with an error

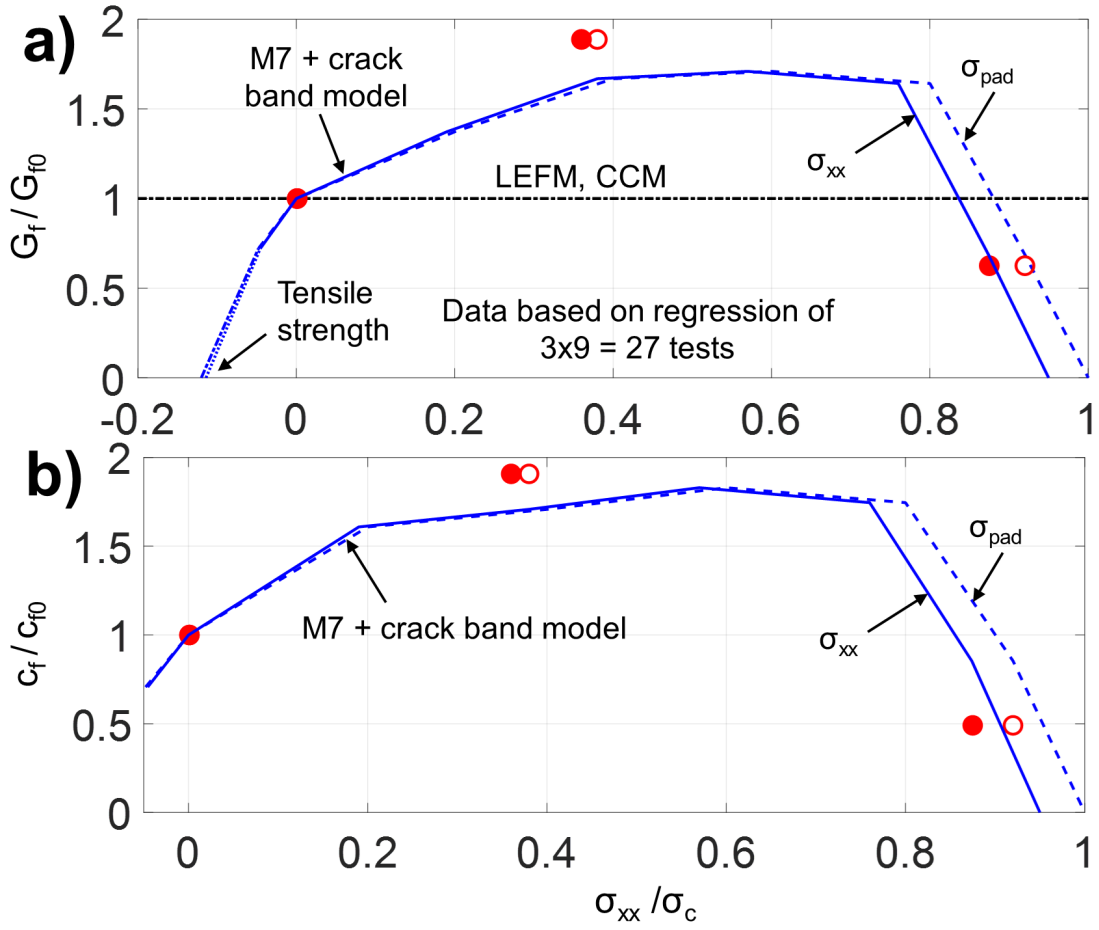

Figure 2.7: (a) G_f ($G_{f0} = 86.7$ N/m) as a function of σ_{pad} (dashed curve) and of σ_{xx} (solid curve); (b) c_f ($c_{f0} = 8.8$ mm) as a function of σ_{pad} (dashed curve) and of σ_{xx} (solid curve).

less than 3%. That σ_{xx} must be less than σ_{pad} is intuitively obvious from the field of principal stress vectors in Fig. 2.7c obtained by FE. The data points of σ_{xx} obtained after transformation with r_c are shown as the solid squares in Fig. 2.7a.

For zero crack-parallel compression, the gap test gave $G_f = 86.7$ N/m, which is within the range of values reported by many authors [14]. The characteristic length in this case is approximately 18 mm. This is about 1.5 times the average coarse aggregate size.

For a moderate crack-parallel compression, $\sigma_{xx} \approx 0.4\sigma_c$, the size effect analysis of the present test data yields $G_f = 154.2N$/m, which roughly doubles the value at zero compression (Fig. 2.7a).

The material characteristic length is also nearly doubled, to c_f = 37.1 mm, and the FPZ gets more elongated. Another consequence is that the postpeak softening slope gets less steep or that the snapback is suppressed.

For high crack-parallel compression at $\sigma_{xx} = 0.9\sigma_c$, the fracture energy is, by contrast, drastically reduced—to G_f = 51.2 N/m (Fig. 2.7a). So is the value of characteristic length, c_f = 11.2 mm, which indicates a shorter and wider FPZ, and a reduced c_f. As $D \to \infty$, the final asymptotic slope of LEFM, $-1/2$, is approached more quickly. Hence, the brittleness number D/D_0 [14], [23] for a given D increases.

Alternatively, according to the classical work-of-fracture method [54]–[56], one could estimate the total fracture energy, G_F, via the area between the entire up-and-down curve and the horizontal yield line in Fig. 2.3c. However, this method requires stabilizing the postpeak softening and is rather ambiguous if the correct shape of the cohesive law, Fig. 1.4a, is not known *a priori* [26]. To avoid ambiguity of G_F, the work-of-fracture test would have to be also conducted for several sufficiently different specimen sizes [26].

2.8 Physical mechanism of crack-parallel stress effect on G_f

The mechanism was briefly discussed in [42] and here we are more specific. Depending on the magnitude of crack parallel compressive stress σ_{xx} (negative for compression), we can distinguish two different regimes of FPZ behavior, explained by two different mesoscale mechanisms:

Regime 1: Friction: Moderate σ_{xx} increases static friction which prevents slip, and provides confinement without damage. This tends to increase strength and may be explained by the increase of interlocking and increase of static friction on rough inclined surfaces. For σ_{xx} = 0, the deviatoric (or shear) stress intensity $\tau = \tau_a$, shown in the figure, corresponds to hydrostatic pressure is $p = p_a = -\sigma_{yy}/3$, where σ_{yy} is the tensile normal stress caused by beam bending in the FPZ at crack or notch front; see Fig. 2.8a ($\tau = \sqrt{J_2}$ where J_2 = second invariant of the stress deviator. By applying a not too high compressive stress σ_{xx}, the hydrostatic pressure increases from p_a to $p = p_b = (\sigma_{xx} - \sigma_{yy})/3$ and the stress state corresponds to an expanded circle. Thus p_b provides confinement, which increases the resistance τ from τ_a to τ_b, as shown in Fig. 2.8b. Moreover, the numerical simulations show the active FPZ to become longer and narrower, which may be explained by a reduction of the average inclination of the microcracks from the macrocrack direction.

Regime 2: Expansive Slipping and Splitting: When, however, compression σ_{xx} is raised to approach the compressive stress limit, one must consider the Mohr circle shifted to the left in Fig. 2.8c. The minim principal stress indicates the uniaxial splitting strength of concrete, where, FPZ is failing in compression due to σ_{xx}. The static friction on inclined microcracks in the FPZ is overcome and the cracks slip, which tends to widen the active FPZ and reduce the resistance to tensile stress σ_{yy} caused by bending, as intuitively explained by sliding over the entire FPZ portrayed in Fig. 2.8c. This kind of failure mechanism has been observed in simulations with the

crack band microplane model, by inspecting the stresses and deformations in FPZ on microplanes of inclined orientations. Another possible mechanism is the arise and collapse of splitting microcracks between micropillar of width s [57], which also leads to lateral widening (Fig. 2.8b) and shortening of FPZ. The widening and shortening of the FPZ in this regime in manifested in a decrease of c_f obtained from the size effect method.

The widening of the FPZ is accompanied by widening of the crack or notch behind it, which further allows the compressed material at crack faces to expand into the crack space and thus reduce the resistance to compression.

After the experiments, the fractography showed small, crumbly pieces of nearly detached concrete, demonstrating the formation of small splitting microcracks and slip expansion. Another consequence is that the postpeak softening slope gets steeper or that snapback gets promoted.

Does Mohr failure envelope exist? The Mohr circles for different stress states in the FPZ are plotted in Figs. 2.8b,c (σ = hydrostatic stress, τ = maximum shear stress). The first slip mechanism, frictional resistance with no damage, seems to follow a curved Mohr failure envelope with strength expanding at moderate increase of hydrostatic pressure (Fig. 2.8b). However, when the second mechanism with expansive damage takes over, the Mohr envelope concept breaks down. This is blatantly demonstrated by zooming in Fig. 2.8c, on the critical region of small σ and τ. Obviously, no envelope exists. This is not surprising since the plasticity-type failure criteria based on tensor invariants are inherently incapable of capturing the concentration of slip into planes of distinct orientations, which represent the reality.

We note that, a reasonable prediction of the numerical models to explain the experimental results (in Figs. 2.7, 2.8) was made available through the microplane model along with the crack band theory in its M7 version. The detail of such model will be discussed next.

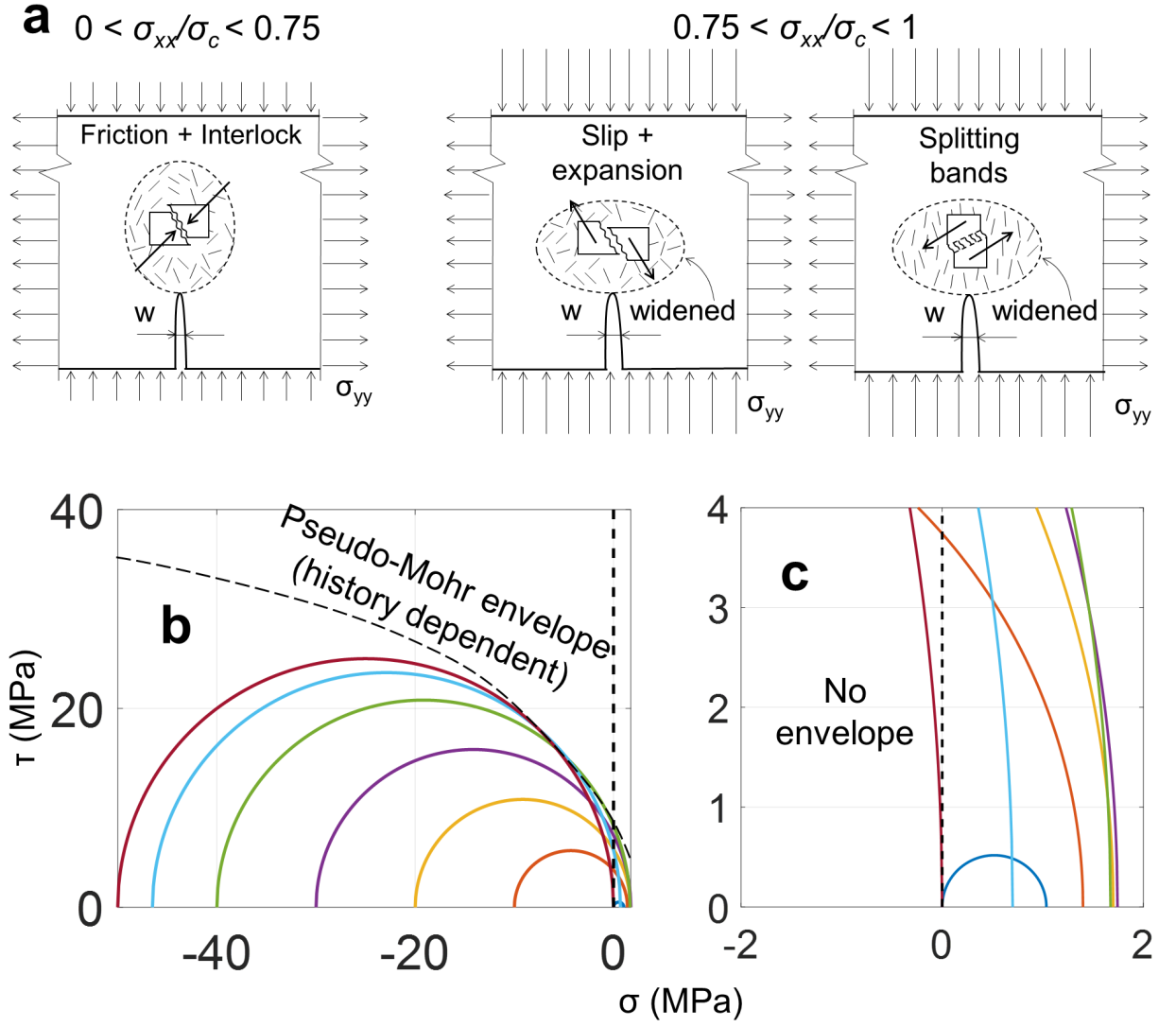

Figure 2.8: (a) Suggested mechanisms for enhancement and diminishing of G_f; (b) Mohr circles corresponding to the M7-CBM predictions in Fig. 2.5a), with σ_{yy} = nominal strength at peak load for samples of medium size; and (c) A closer look to the region of small σ_{xx}.

2.9 Basic features of microplane model

The classical plasticity and damage models use the stress and strain tensors with tensorial invariants and their constitutive law is defined by loading surfaces, normality rules, plastic-hardening parameter(s) and damage parameter(s). Such models are called tensorial. The microplane constitutive model also relates the stress and strain tensors. But the constitutive law is vectorial [8], [13], [14], [21], [58]. It is defined as a relation of the stress vectors to the strain vectors, the latter representing the projections of the strain tensor onto a generic plane of arbitratry orientation within the material, called the microplane. The use of vectors helps physical insight, intuitively reflecting the microcrack openings, compression splitting cracks, shear slip and frictional dilatancy. M7 is the latest in a series of progressively improved models M1–M7. In M7, as well as M3 and M4, all the inelastic behavior is characterized by the stress-strain boundaries. The return (or drop) to a boundary is in each loading step done at a constant strain (which amounts to a special case of the radial return algorithm). The drop to the boundary on the microplane level suffices to guarantee non-negativeness of energy dissipation. There is no need for non-associated plasticity violating the normality rule. Unequal friction and dilatancy angles on the continuum level are reproduced automatically, with no possibility of negative energy dissipation (the non-associatedness is a non-issue for microplane model). The stress tensor is obtained variationally according to the principle of virtual work, by properly weighted integration over all spatial orientations. The integration is carried out numerically over a hemispherical surface according to one of optimal Gaussian formulas. It amounts to weighted summation over a set of discrete microplanes (whose number must be at least 21 but typically is 37, see Fig. 2.9).

The boundaries of negative slope define the evolution of damage, and the horizontal ones define plasticity. There is no need for hardening plasticity, since it is automatically generated by

interaction of the microplanes. Also, there is no use for a separate damage parameter per se, and there exists no single damage variable (they are many). There are one normal component and two shear components on each microplane. Using 37 microplanes per hemisphere, one has effectively 37 x 3 = 111 possible damage and plasticity sources. In effect this is a sort of analog of multi-surface plasticity with 111 independent loading surfaces which are, however, vectorial rather than tensorial. This feature explains why the vertex effect is endemic, why it can occur at any point of the 9D space of stress tensor components. Beginning with Koiter [59], [60] and Phillips [61], it has been widely acknowledged that multisurface plasticity is more realistic, but 111 (even 10) plastic loading surfaces in the tensorial, rather than vectorial, space would be virtually intractable, both for model development and computer modeling (an omnipresent vertex effect nevertheless exists also in the tensorial endochronic theory [62] which, however has other limitations).

The fact that all the response within the boundaries is treated as elastic is a significant simplification. Curved rising stress-strain response is nevertheless automatically reproduced, thanks to different boundaries kicking in gradually in different loading steps. The damage is generated on softening stress-strain boundaries at some microplanes but not at others, which is what creates the strong path dependence of the constitutive law at continuum level. The generation of damage on a microplane does not proceed monotonically. The damaged material can even stiffen when, e.g., hydrostatic pressure or transverse compression gets superposed on damage in shear (Figs. 2.9).

During unloading and reloading, different microplanes become active. This is what reproduces the Bauschinger effect and the correct response under load cycleskirane2015microplane. Even though the plentiful test data on cyclic and fatigue fracture are not covered here, the ability to capture the opening and closing of microcracks and sequential microplane activation in a material experiencing multiple loading cycles is also an important capability of model M7. The M7 crack band model [53], [63] has been shown to possess such a capability. It can predict the behavior up

to several thousand load cycles. The explicit description of damage on each microplane helps.

One feature that simplifies model formulation is that one-to-one relations between the conjugate stress and strain components on the microplanes are sufficient. There appears to be no need for cross-interactions such as the Poisson effect on the microplanes. The reason is that such cross effects are automatically generated by interaction of microplanes of different orientations.

What matters for the good performance of CB-M7 is that this model implies three independent material characteristic lengths. The M7 correctly captures the fact [14], [21] that the tensile post-peak softening curve begins with a steep softening slope and ends with a very long tail (Fig. 1.4). The area under the initial slope is called the initial fracture energy G_f. The total area including the whole tail is called the total fracture energy G_F. The corresponding Irwin's lengths, which are $l_f = EG_f/f_t^2$ and $l_F = EG_F/f_t^2$ matter mainly for the length of the FPZ, while the w_0 is a material length characterizing the FPZ width, considered as the crack band width. The ability to capture all the three material characteristic lengths is an advantage of the crack band model compared to others.

Normally, the microplane model for concrete is calibrated by adjusting its three scaling parameters to fit the tensile strength and Young's modulus. Four more parameters can be easily adjusted to fit the confined compression data. The initial fracture energy G_f is obtained through the fitting of the maximum loads for scaled notched fracture specimens using the size effect law (if such data exist). If G_f is specified , the scaling parameters of M7 are best adjusted so as to fit the size effect law (SEL) that corresponds to the G_f value [14], [21]. Alternatively, a given G_f can be matched as the area under the initial tangent of the postpeak softening load-displacement curve (corrected for dissipation away from the FPZ, if any). The total fracture energy G_F is obtained as G_f times the ratio of the total areas under the total load-displacement curve and under its initial tangent.

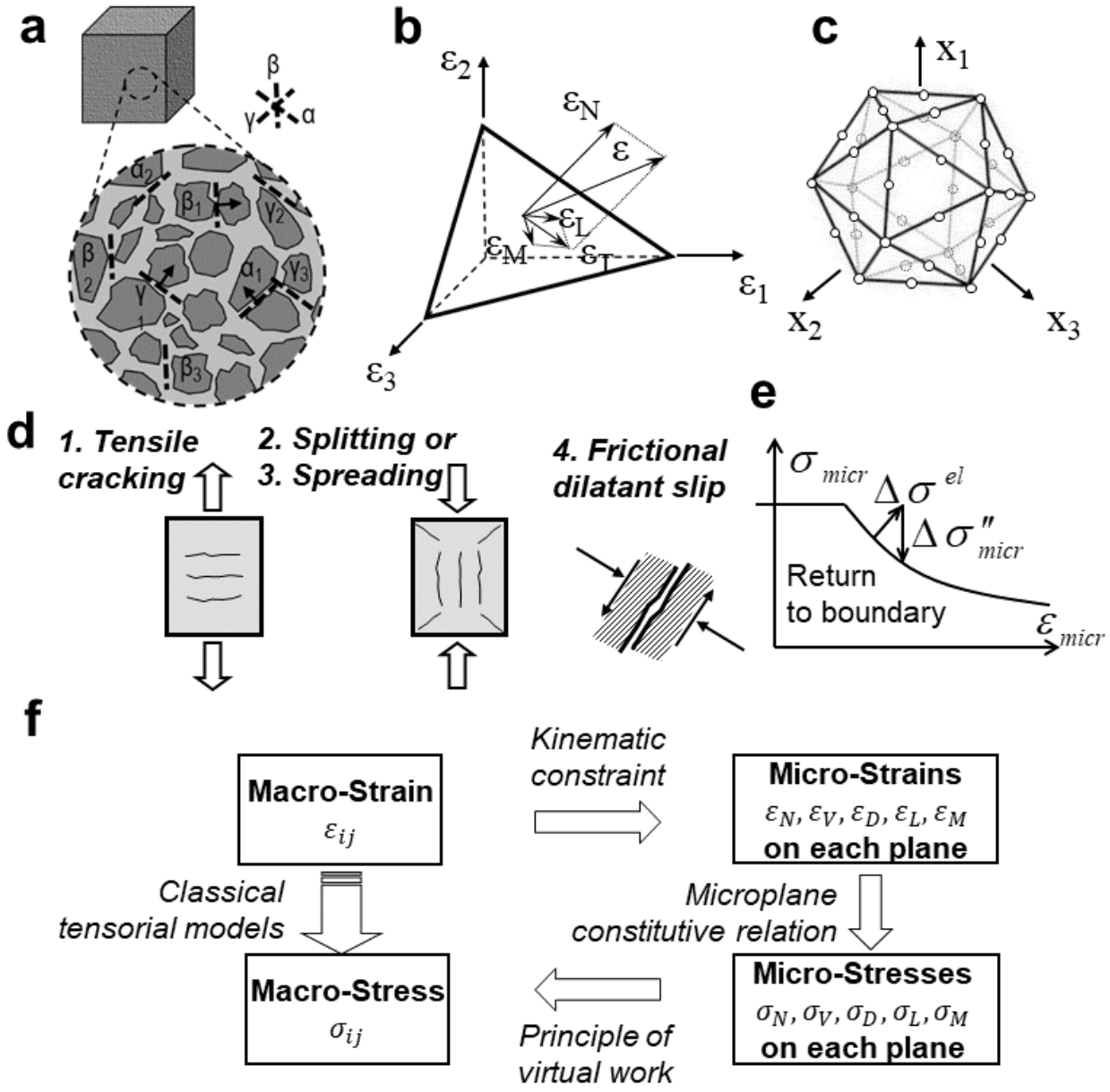

Figure 2.9: (a) The planes of inelastic deformations in a representative volume element of particulate composite are imagined to be lumped into one continuum point. (b) Decomposition of strain vector into its normal and shear components along basis vectors $(\boldsymbol{n}, \boldsymbol{l}, \boldsymbol{m})$. (c) The normals to radial rays through the circled points on this icosahedron define the system of microplanes. (d) The mechanisms that can be captured by microplane model. (e) Predictor-corrector method for each component on one microplane allows the damage to emerges naturally without using a damage variable. (f) The constitutive algorithm to compute stresses from strain tensor via microplane decomposition.

Essential features of microplane model to correctly predict the effect of crack-parallel stresses on G_f

The microplane model used in the present simulations is described in detail in [13]. Let us list here briefly the features of microplane model that are advantageous for the modeling of crack-parallel compression effects and distinguish it from the models based on tensors and their invariants.

1) Whereas the microplane model calculates the strain tensor from the stress tensor, the constitutive equation is vectorial, calculating the stress vector from the strain vector on a generic plane of any orientation, called the microplane. The vectors, unlike tensors, can be intuitively related to tensile crack opening, compression splitting or frictional slip.

2) A big advantage is that one can capture the *vertex effect*, e.g., the fact that a shear stress increment applied after compressive stress in the inelastic range has incremental stiffness much softer than elastic (even three-times lower, for concrete), while in all the classical tensorial models (Mohr-Coulomb, Drucker-Prager, von Mises, etc.) a stress increment parallel to the loading surface gives incorrectly an elastic incremental stiffness, even in damage states.

3) Another advantage is that, in M7, the hydrostatic or uniaxial strain compression is always hardening, while the uniaxial compressive stress has a peak and postpeak softening.

4) M7 also delivers correct hysteretic loops under cyclic loading, and reproduces subcritical fatigue crack propagation up to several thousand cycles (in agreement with Paris law).

Early on it was thought that the microplane model was computationally too demanding. For one material point it may run ten-times longer than a tensorial constitutive law. But for a system of millions finite elements, tractable today, the difference in running time is imperceptible because the computational work increases, with the number of displacements, quadratically, but on the constitutive law only linearly.

The confirmation of the variation of FPZ using crack band microplane model M7

As the M7-version of microplane model does not have explicit definitions of damage variables, any inelastic strain arises when an incremental vector in the stress-strain space goes beyond the boundary. Therefore, to describe the change of FPZ as a function of σ_{xx}, we used the J-integral [64] technique to calculate the energy release rate at the peak load. This value indicates the amount of energy dissipated along a unit length of crack and is equal to of G_f at any structural size. However, in finite element method, calculate a contour integral is challenging, so Li *et al.* [65] proposed a method to convert the contour integral to a domain integral with the following relation (Fig. 2.10):

$$\begin{aligned} J &= -\oint_C \left[(\sigma_{ij}-\sigma_{ij0})\frac{\partial u_i}{\partial x_1} - (W-W_0)\delta_{1j}\right] n_j \mathrm{d}s \\ &= \int_A \left[(\sigma_{ij}-\sigma_{ij0})\frac{\partial u_i}{\partial x_1} - (W-W_0)\delta_{1j}\right] \frac{\partial q_1}{\partial x_j}\mathrm{d}A \end{aligned} \tag{2.20}$$

where the flux is meant with respect to crack length a, not time; C is a closed contour around the crack tip, s is the length coordinate of that contour, n_i its unit outward normal, $x = x_2, y = x_1$ (x_1 is always aligned with the propagating direction), $\partial_1 = \partial/\partial x_1$, and $\frac{1}{2}s_{ij}e_{ij}$ is the stored strain energy recoverable upon unloading and W is the nonlinear strain energy density. A is the domain between two contours C_{inner} and C_{outer} so that it contains the entire contour C. q is a function that has a value of 1 on and outside of C_{outer} , 0 on and inside of C_{inner} and continuous otherwise (see Figs. 2.10a,b). The material is considered nonlinearly elastic, as if the unloading would follow the same curve as loading. This hypothesis is acceptable if the J contour avoids the zone of unloading in the wake of the advancing yielding zone. Elasticity, whether linear or nonlinear, is essential for the path independence of J-integral.

The hypothesis is confirmed by the results in Fig. 2.10c, in which contour 1 represents a

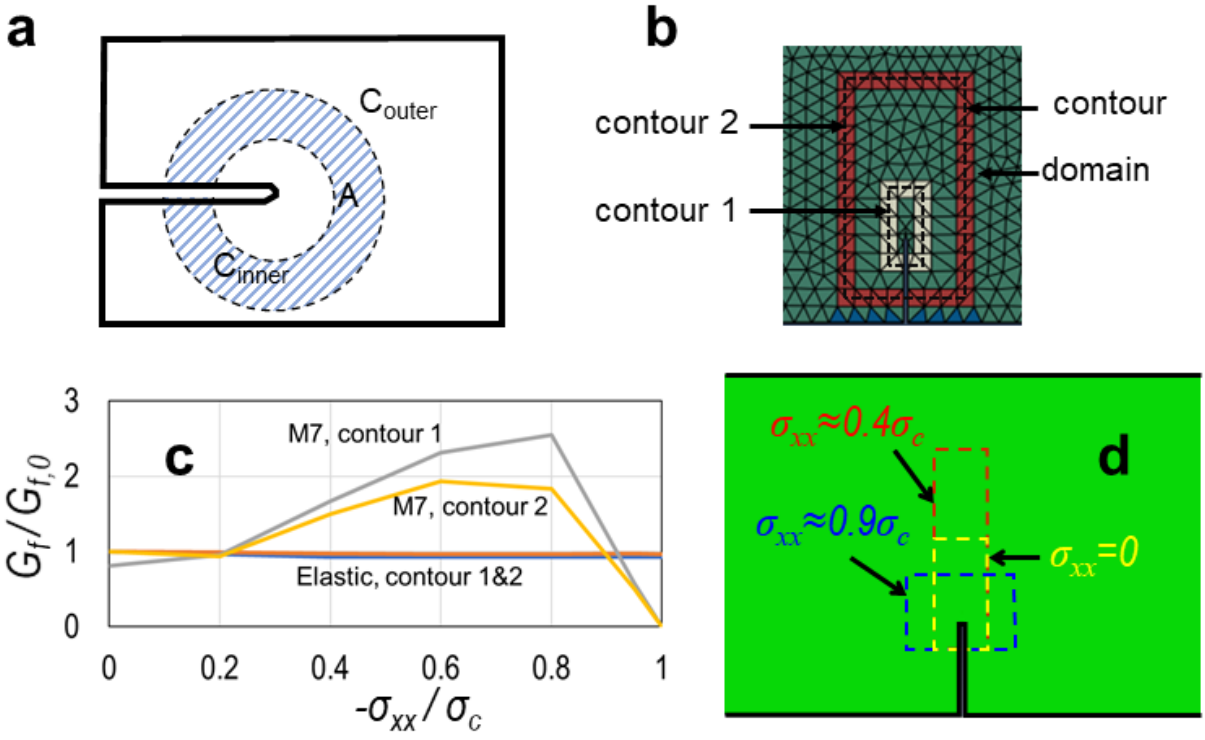

Figure 2.10: (a) The conversion of contour integral to domain integral and how it is calculated using FEM (b). (c) The results from a non-converged and converged contour. (d) An approximation of the variation of FPZ using J-integral contour and M7 model.

contour that crosses the softening zone. Contour 2, on the other hand, is taken completely outside of the FPZ and therefore represents a converged value of G_f at different σ_{xx}. It can be seen that there are a few deviations in Fig. 2.10c compared with Fig. 2.7a (at $-\sigma_{xx}/\sigma_c = 0.1 - -0.3$), probably due to the inevitable numerical issues when comparing the stress field.

The smallest contour where $J_{cr} = G_f$ converges can be an considered an approximated image of the FPZ; see Fig. 2.10d. The hypothesis on the variation of the FPZ due to σ_{xx} (2.8a) is confirmed by the expansion in size of this contour when the crack parallel stress increases to an intermediate value. However, such a contour significantly reduces when σ_{xx} comes closer to σ_c and expands in the laterial direction, indicating the dilation of microcracks by the compressive stress.

2.10 Further simulations of crack-parallel stress effect on G_f

Plane strain and anti-plane normal strain effects

Another interesting aspect is the effect of the antiplane stress σ_{zz}. For σ_{zz} applied on the entire side faces of the present specimens of three sizes, several simulated curves of $G_f(\sigma_{xx})$ are plotted in Figs. 2.11 a,b for various ratios σ_{zz}/σ_c. Obviously, in this case (apparently never studied before), σ_{zz}, too, has a significant effect.

History-dependence of the crack-parallel stress

To demonstrate the path dependence, which is ignored by any formula for G_f (such as Eq. (2.21), Fig. 2.12 presents, for the mid-size concrete specimen, the M7 simulations for four different paths (or histories) of $2R/bD$ versus σ_{xx}, where R is the beam end reaction that produces the bending moment, M, to which the stress-intensity factor K_I is proportional. 1) The first path is a simple increase of R at σ_{xx} = 0 up to failure, which defines the nominal strength σ_N. 2) In the gap test path, as already described, a high crack-parallel compression $\sigma_{xx} = 0.9\sigma_c$ is applied first, and the

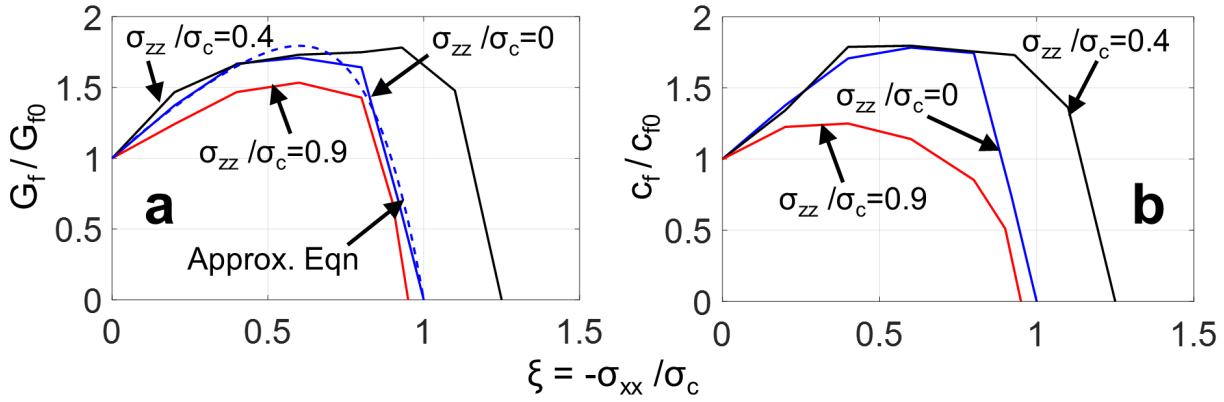

Figure 2.11: G_f and c_f as functions of σ_{xx} subject to different values of anti-plane stress σ_{zz} (with results approximated by Eqn. 2.21).

subsequent path segment with increasing R ends up with the failure value of $2R/bD = 0.62\sigma_N$, as seen in Fig. 2.12. 3) When, however, the end reaction, $R = 0.62\sigma_N$ is applied first (which would require a more complex test setup and controls), and the crack-parallel compression σ_{xx} is subsequently increased up to failure, the failure occurs at significantly higher compression σ_{xx} (because FPZ was less damaged during the first segment of the path. 4) When only a moderate crack-parallel compression $\sigma_{xx} \approx 0.4\sigma_c$ is applied first, the reaction R can be increased to a much higher value, with $2R/bD = 1.81\sigma_N$.

Comparisons with tensorial plastic-failure models

1) Model CDPM2 – constitutive damage plastic model for concrete of the classical type, defined in terms of stress and strain tensors and their invariants. This is an excellent model that has recently been developed by Grassl *et al.* [66], within the framework of tensorial plasticity with damage. The G_f variation obtained with this model is shown in Fig. 2.12b. The qualitative trend obtained reflects both strengthening and weakening phases of G_f evolution, but the differences from M7 are significant and the deviations from the gap test in the last weakening phase is large.

Drucker-Prager and Mohr-Coulomb model from Abaqus: The G_f evolution calculated with the classical Drucker-Prager's (D-P) model [67] is presented in Fig. 2.12c. The strengthening phase is represented, but there is no weakening phase. For this model, the uniaxial compression stress test produces bulging at mid-length of the specimen rather than formations of splitting cracks and inclined shear bands. The strengthening phase gets captured because the D-P described well the frictional resistance to slip and interlock under under triaxial confinement. It should also be mentioned that, at high compression σ_{xx}, the size effect method is inapplicable because there is premature compression failure at the crack front. This gets manifested as a macro-crack in front of the notch, which significantly lowers the peak load, especially in the largest specimens (Fig. 2.12d). This stems from the fact that the largest specimens are less confined by the boundary. Therefore, at higher compression, the size effect G_f had to be computed from linear regression of the results for only the small-size and mid-size specimens, as represented by the dashed curve segment in Fig. 2.12c.

Mohr-Coulomb concrete model with a cap, from Abaqus: Unlike the D-P, the Mohr-Coulomb's model [68] produces an artificial stiffening effect at the crack tip, even at zero σ_{xx}. Therefore, it appears inapplicable for fracture analysis.

2.11 Limitations of cohesive crack model and contrast with crack band model

The present results highlight the limitations of the cohesive crack model for quasibrittle materials. In the case of Mode I fracture, this model is defined by a scalar relation between the crack-bridging, or cohesive, normal stress and the relative normal displacement across the crack. In the case of mixed mode fracture, the model is defined by a relation of crack-bridging normal and shear stresses to the relative normal and shear displacement. But the crack-parallel normal stresses (and strains) cannot be included as the basic force and displacement variables. They can be considered only as

parameters affecting the material fracture properties. For the effect of σ_{xx}, [42] gives the formula

$$\frac{G_f}{G_{f0}} = 1 + \frac{a}{1 + b/\xi} - \frac{1 + a + b}{1 + b}\,\xi^s \tag{2.21}$$

where $\xi = \sigma_{xx}/\sigma_{xx,c}$, and $\sigma_{xx,c}$ at $\sigma_{pad} = \sigma_c$. The curve in Fig. 2.2A,B is well approximated by a = 1.038, b = 0.245, s = 7.441 (as shown by dashed curves). These values will, of course, be different for different materials, structure sizes, load histories, σ_{zz}/σ_{xx} ratios, etc.

A fully realistic model for quasibrittle fracture must, therefore, well describe the microscale mechanisms mentioned above. This can be either a tensorial, with the FPZ described by a tensorial damage constitutive model with strain softening, coupled with some form of a localization limiter or mesoscale descriptive. The simplest and most widely used model is the crack band model coupled with a physically realistic form of the continuum damage model, here the microplane model, underlying the present simulations.

It should be noted in Fig.2.7a that there exists a threshold at which the crack-parallel compressive stress σ_{xx} turns from strengthening to weakening of the fracture resistance. For the present concrete, it is $\sigma_{xx} \approx -0.75\sigma_c$. No doubt this threshold varies among different materials, and for some the strengthening phase might not exist. This might be the case for some uniaxial laminate fiber composites, notoriously weak in compression.

From the microplane simulations it is clear that the microcracking in the FPZ produced by high crack-parallel compressive stress σ_{xx} must increase permeability in the FPZ and in its wake as the crack propagates. This is important for various geomechanics problems, and particularly for hydraulic fracturing (or fracking) of gas or oil shale. In [69] is was shown that the permeability and reduced transverse Biot coefficient due to preexisting microcracks with its Biot coefficient is what causes the hydraulic cracks to branch sideways from the wall of a primary hydraulic crack. The

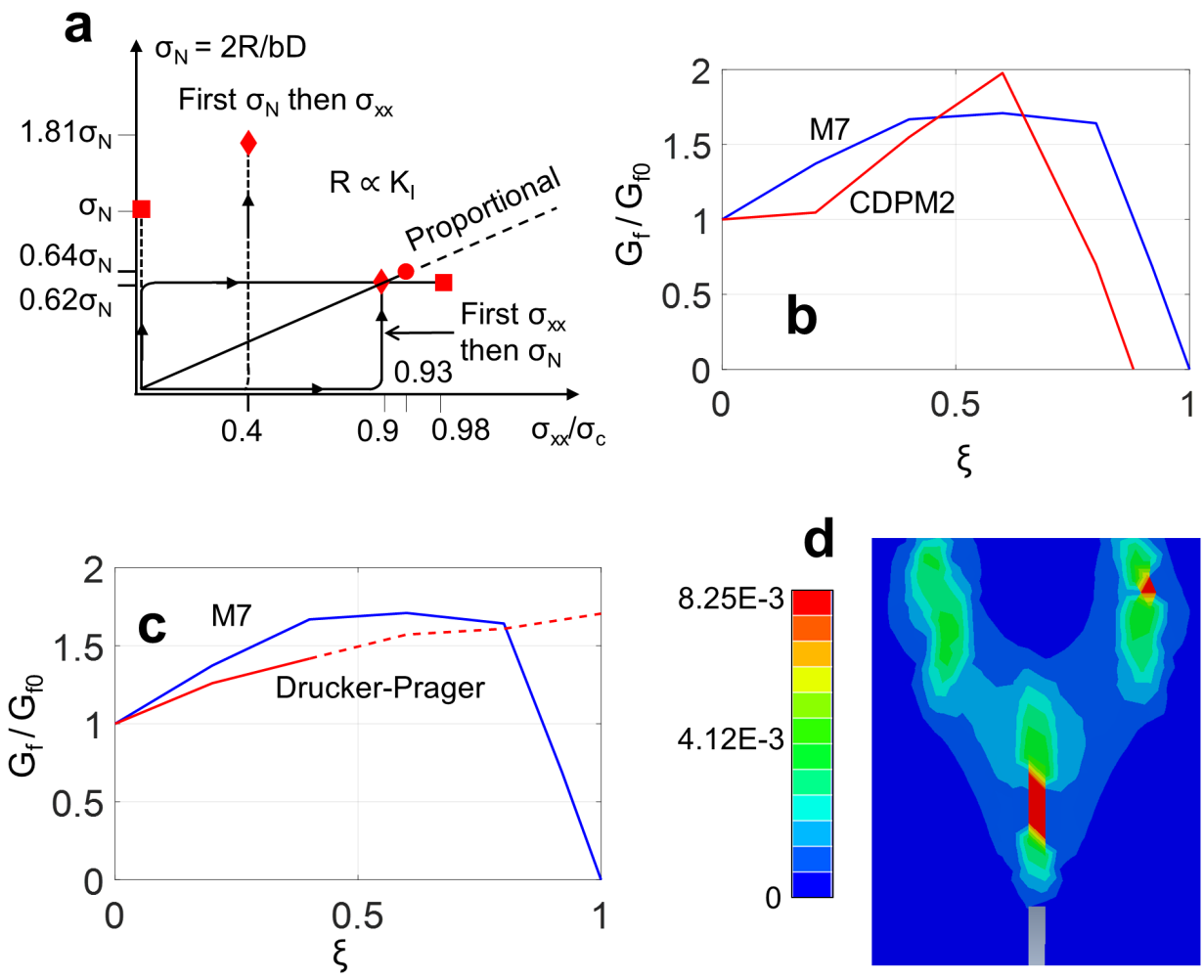

Figure 2.12: (a) History dependence of the stress path; (b) G_f as a function of σ_{xx} predicted by tensorial models by Grassl *et al.* [66] σ_{xx}; (c) G_f as a function of σ_{xx} predicted by tensorial Drucker-Prager model [67] a; and (d) A premature failure predicted by D-P ahead of the main crack tip before moment M is applied.

present analysis shows that the propagations of the primary crack and secondary branched cracks must be strongly affected by the crack-parallel overburden and tectonic stresses, which are about 80 MPa and 40 MPa at the typical depth of fracking, about 3 km.

Because of their simplicity, scalar models for softening damage have become popular for crack band representation of fracture. Some examples are Mazars' isotropic damage model for concrete [70], the nonlocal damage model [71]. and all other models using the Kachanov-Hult-Lemaitre type scalar damage measure ω. These damage laws may be unrealistic for two reasons—they have not been calibrated by various types of triaxial material tests on specimens of sizes nearly equal to the FPZ (or RVE) size (see 21 types of such tests used to calibrate M7 in [53]). Their use of a single scalar damage parameter, φ, varying between 0 and 1, appears too restrictive (the microplane model and fracture characteristics has several independent damage parameters). All these models are usable only if the crack-parallel normal stress is *a priori* known to be negligible (or below about 10% of compressive strength) in all the finite elements within the damage zone. As for peridynamics, no comments are necessary [72].

The fracture models characterized only by G_f can be used if reprogrammed to vary G_f as a function of the crack-parallel stresses, σ_{xx} and σ_{zz}. This, of course, ignores history effects, whose severity has not yet been clarified. As for the cohesive crack model, its softening stress-displacement law would have to be varied depending on σ_{xx} and σ_{zz}. But this brings up the questions of whether the cohesive softening curve should be scaled as a whole (which would scale both G_F and G_f, or only in its initial part (controlled by G_f only), what should be the proportion of such scalings, and whether a horizontal scaling is also necessary. Again, this would miss history effects.

2.12 Gap test for crack-parallel tension

Finally, it may be pointed out that the gap test may be easily adapted to measure the effect of crack-parallel tension on G_f. The setup shown in Fig. 2.13 is self-explanatory.

2.13 Alternative test methods

As an alternative to the present test, a system of two balance beams shown in Fig. 2.14, was fabricated and tried to provide reactions at both beam ends and notch corners, the ratio of these reactions being controlled by moving the locations of the supports at base. But it proved tricky to keep the system stable and properly aligned before applying the load. Another bigger problem was seen in the evaluation. This test would have to be conducted for several different specimen sizes D and heavy I-sections, which must provide a much larger stiffness than the largest specimen size. The self-weight of these I-sections would add up to σ_{xx} or bending moment non-proportionately, which will create complication to the fracture analysis. The biggest problem is that the compressive force would not be constant but (in theory) raised proportionally that would make it difficult to deduce the effect of σ_{xx} on G_f. Since σ_{xx} does not matter for the size effect method, this method could still be used, but it would deliver a fracture energy corresponding to a certain history of σ_{xx} rather than to any specific value of G_f. Complex optimization of tests with many different histories, using an assumed constitutive damage law, would be required, to obtain a rather uncertain result for the effect of σ_{xx} on G_f. The constancy of σ_{xx} is what makes the gap test simple and unambiguous.

As another alternative, one might also think of imposing a compressive displacement with pair of stiff clamping frames mounted on the beam. But the stress induced would relax (by about 30%), due to concrete creep and shrinkage during the test. To get G_f as a function of strain ϵ_{xx}

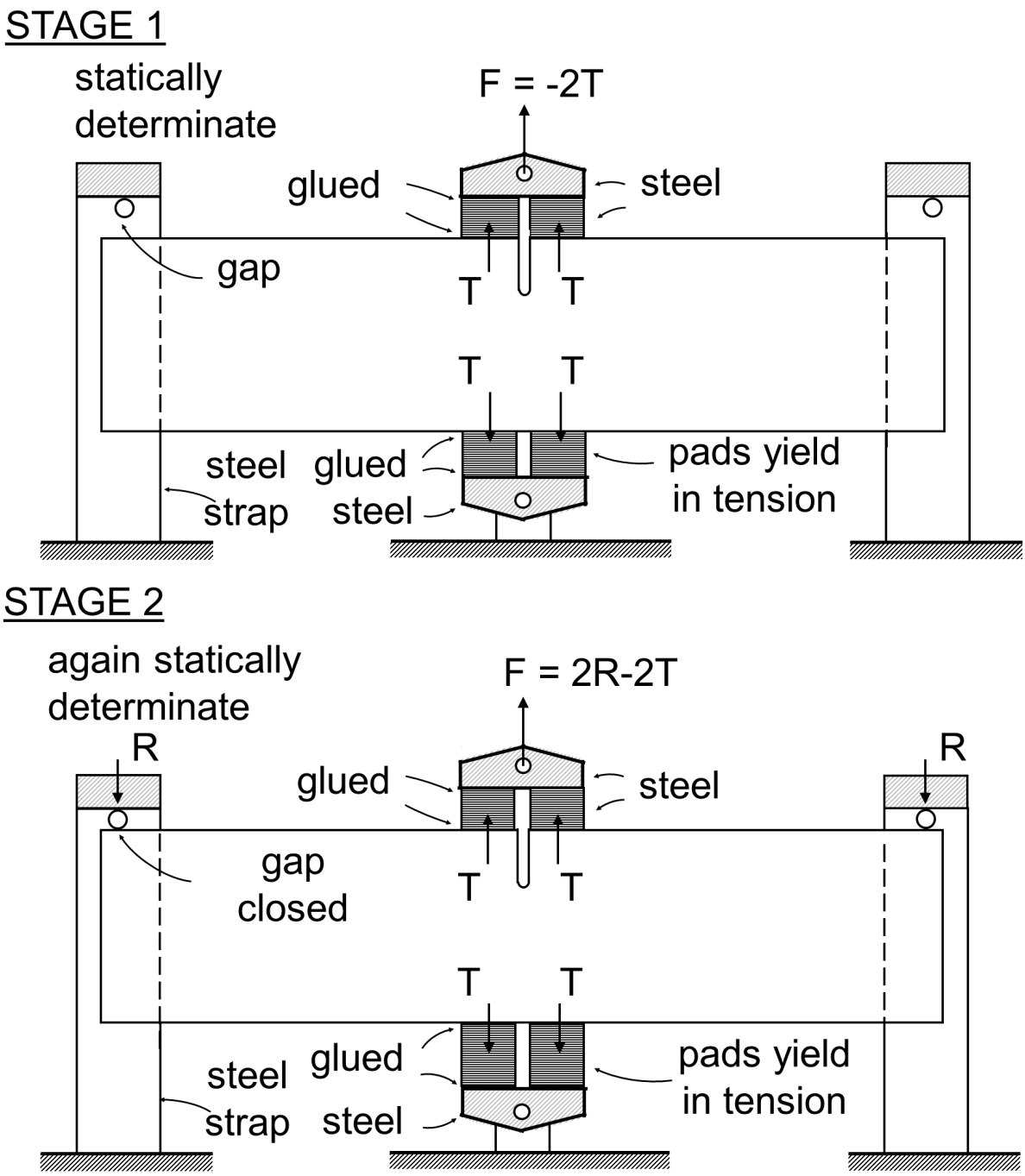

Figure 2.13: Gap test for crack-parallel tension.

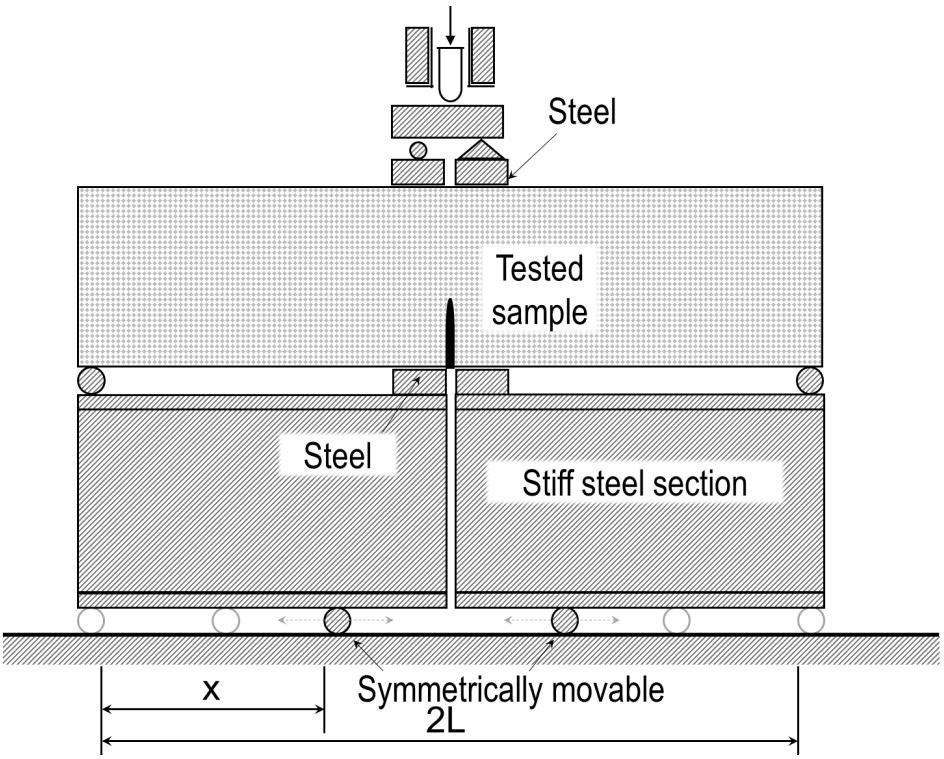

Figure 2.14: An alternative test method considered to generate σ_{xx} with proportional loading.

instead of σ_{xx}, the clamping frames would have to be very stiff and heavy, to maintain constant ϵ_{xx}, and would have different relative weights for different specimen sizes. Another possibility would be hydraulic flat jacks within these frames, similar to those of Tschegg [22] but equipped with computer control. Interpretation would anyway be fraught with ambiguity.

CHAPTER 3

SCALING OF STRUCTURAL STRENGTH FOR DUCTILE MATERIALS

3.1 Scaling tests - a missing piece in understanding the fracture of ductile materials

The theory of small-scale yielding in fracture of plastic-hardening metals is by now a well-developed classical subject. Nevertheless, the analytical laws governing its scaling properties have apparently not been formulated, although they may be useful for fracture testing and for predicting structure strength. Their formulation is the main goal of this study.

The foundation of the small-scale yielding fracture mechanics was laid down by Hutchinson [5], [73] and Rice and Rosengren [4]. They calculated the near-tip singular field, generally called the HRR field, in which the strain energy density exhibits a $1/r$ singularity (r = radial distance from crack tip). Essential for this advance was Rice's J-integral [64], which allowed calculating the energy flux into the crack tip under the hypothesis of negligible elastic strains and no unloading in the near-tip yielding zone. A critical value of the J-integral, J_{cr}, thus became the criterion of crack propagation, and an effective method of measuring J_{cr} was developed [64], [74], [75].

What distinguishes metals most from quasibrittle materials, such as concrete, rocks, tough ceramics and fiber composites, is that the fracture process zone (FPZ), which is of micrometer-scale width and length, is surrounded by a plastically hardening zone. In this respect, though not in others, the fracture of plastic-hardening materials is more complicated than it is for quasibrittle materials, in which the FPZ borders directly on an unloading material undergoing damage.

In fracture of quasibrittle materials, the scaling, particularly the energetic size effect on the strength of specimens or structures, proved to be an essential property, not only for structural

design but also for the testing of material fracture properties, including both the material fracture energy, G_f, and the characteristic FPZ size, c_f. Strangely, though, for ductile fracture of plastic-hardening metals, the problem of an asymptotically matched size effect law for the strength of geometrically similar cracked specimens or structures and for identification of material fracture properties has apparently not been studied.

Important studies of the size and behavior of the yielding zone in ductile fracture have nevertheless been contributed, and supported by extensive finite element analyses. In particular, O'Dowd and Shih [30], [31] proposed the concept of J-Q-annulus surrounding the crack tip, in which the J-integral characterizes the remote stress field corresponding to a $-1/2$-power stress singularity, while Q corresponds to the second, non-singular, term of the near-tip asymptotic expansion, which represents a uniform stress field of crack-parallel T-stress. This stress was shown to act as a crack tip constraint, suppressing cleavage. The J-Q concept, however, has not been extended to a simple analytical scaling law which is the objective here. Similar comments apply to the studies of Betegón and Hancock [32], Xia, Wang and Shih [34], and Gao, Shih, Tvergaard and Needleman [35]. Although the T-stress will not affect the form of the scaling law derived here, it will affect the prediction of the effective size, r_p, of the yielding zone, which figures as a parameter in this law, identifiable by size effect tests.

The effect of crack-parallel stresses on r_p is relegated to a subsequent chapter. So is the likely effect of T-stress on the G_f and on the transverse width of the (micrometer-scale) fracture process zone in metals. Such effects have recently been demonstrated for quasibrittle materials [42], [76].

Finally, it should be noted that, in the field of metals, the term "size effect", has been applied to a variety of different phenomena. E.g., the well-known Hall-Petch effect [36]–[38] is not a size effect on structure strength but the effect of grain-size on the yield strength of metal, explained by dislocation arrest at grain boundaries. In crystal plasticity, the term is used for the strength

variation of miniaturized single-crystal specimens [39]. The term has also been used for the effect of geometrically necessary dislocations and of strain gradients on the yielding strength of metals. Further the term has been used for the increase of specific cutting force with a decreasing depth of a cut [40].

Another point needs to be clarified. In quasibrittle fracture, two types of size effect on structure strength [45] must nowadays be distinguished. Here we deal only with Type 2, which occurs when geometrically similar structures of different sizes contain at maximum load large similar cracks or notches. Type 1, to which most of the present analysis doe not apply, occurs for failures at fracture initiation from a smooth surface, and has, for large structures, a strong statistical component.

The present objective is to find the law governing the size effect in metallic structures with large cracks propagating in the opening mode, i.e., mode I.

3.2 Scaling of near-tip field and of structure strength in absence of a characteristic length

Assuming homogeneous plasticity, the field of any continuum variable close enough to a perfectly sharp tip of a crack (or notch) possesses no characteristic length. Therefore, the field must be self-similar in the radial polar coordinate r centered at the tip. In other words, any response $f(r, \theta)$, such as the displacement or stress, must be such that, for any two radii r and ξr, the scaling ratio $f(\xi r, \theta)/f(r, \theta) = \rho$ would be independent of the polar angle θ. Hence, function $f(r, \theta)$ must satisfy the functional equation:

$$f(\xi r, \theta) = \rho(\xi) f(r, \theta) \tag{3.1}$$

To solve it, note that it will be true for all r if and only if it is true for every interval $(r, r + \mathrm{d}r)$. So we differentiate Eq. (3.1) with respect to ξ and get

$$r f_{,\xi r}(\xi r, \theta) = \rho'(\xi) f(r, \theta) \tag{3.2}$$

where $f_{,\xi r}$ and ρ' denote the derivatives on ξr and ξ. Now we may consider $\xi \to 1$ and denote $\rho'(1) = m$ = constant. This converts the functional equation into a differential equation solvable by separation of variables:

$$r \, \frac{\mathrm{d}f(r,\theta)}{\mathrm{d}r} = m f(r,\theta) \tag{3.3}$$

Its solution is $\ln f(r,\theta) = m \ln r + \ln \psi(\theta)$ where $\ln \psi(\theta)$ = integration constant independent of r but dependent on θ. So we conclude that the near-tip field must be a power law in r:

$$f(r,\theta) \; = \; r^m \psi(\theta) \tag{3.4}$$

Substitution into the field equation yields an eigenvalue problem in θ with an infinite series of eigenvalues m. The eigenfield of the lowest eigenvalue dominates near the tip.

Based on Eq. (3.4), we conclude that any field variable near the tip of a crack (as well as or V-notch) must have a separated form in polar coordinates, and that the radial dependence must be a *power function* (this conclusion also applies to various singularities in hydrodynamics, electromagnetism, electrostatics, etc.).

As a particular case, the foregoing argument applies to the nominal strength, σ_N, of geometrically similar structures with similar cracks and loadings but different characteristic sizes D (see Eq. 1–3 in [77] or Eqs. 1.2–1.4 in [15]); σ_N is a load parameter with the dimension of stress, defined as $\sigma_N = P/bD$ where P = load and b = thickness of two-dimensional (2D) structure. The conclusion is that, in absence of characteristic structure size D_0, which is the case for linear elastic fracture mechanics (LEFM), σ_N must scale as a power law of D multiplied by some constant c_S that depends only on the shape (or geometry) of the structure with crack:

$$\sigma_N \; = \; c_S \, D^m \tag{3.5}$$

3.3 Review of power-law stress-strain relation for plastic-hardening metals

According to the deformation theory of plasticity, it has generally been assumed that plastic-hardening metals can be adequately described by the Ramberg-Osgood [78] uniaxial stress-strain law:

$$\frac{\epsilon}{\epsilon_y} = \frac{\sigma}{\sigma_y} + \alpha_p \left(\frac{\sigma}{\sigma_y}\right)^n \tag{3.6}$$

where n = plastic hardening exponent; σ_y = yield strength, ϵ_y = yield strain limit; α_p = empirical parameter (usually denoted as α, but α is generally used for dimensionless crack length); and n = plastic hardening exponent, typically 3 to 20 [4], [5]. Note that the material is considered plastically incompressible by volume, which means that the material yields only in shear, which allows us to deal only with deviatoric stress and strain tensors s_{ij} and e_{ij}.

Beginning with the HRR (Hutchinson-Rice-Rosengren [4], [5]) theory, the elastic strain is neglected, which has the advantage that stress-strain relation, too, becomes a power law:

$$\frac{\epsilon}{\epsilon_y} = \alpha_p \left(\frac{\sigma}{\sigma_y}\right)^n \tag{3.7}$$

The power law is assumed to start at 0, which ignores the initial elastic response. The benefit stemming from a power law is that it enables an analytical solution [4], [5]. As shown in Fig. 3.1, for high exponents n the initial plastic deformations are negligible, and σ_y represents only an equivalent yield limit characterizing the point where the power law takes off.

The simplest and apparently quite realistic tensorial generalization is [4], [5], [74], [75]:

$$e_{ij} = \frac{3\alpha_p \epsilon_y}{2\sigma_y} \left(\frac{\sigma_{ef}}{\sigma_y}\right)^{n-1} s_{ij} \tag{3.8}$$

$$\text{where} \qquad \sigma_{ef} = \sqrt{\tfrac{3}{2} s_{kl} s_{kl}} \tag{3.9}$$

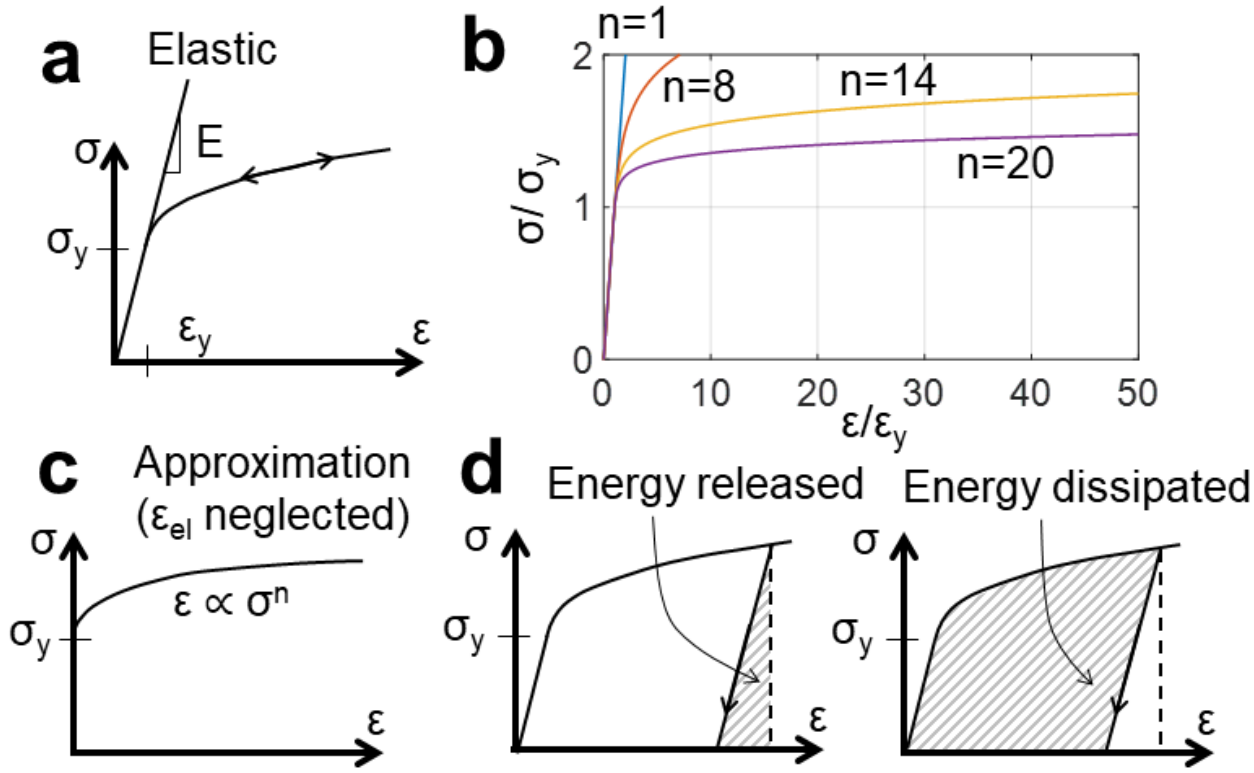

Figure 3.1: (a) Stress-strain behavior of the deformation theory of plasticity (nonlinear elasticity); (b) Elasto-plastic constitutive law with different n; (c) Approximation of total stress-strain by plastic stress-strain relation (elastic strain is neglected); and (d) Partition of strain energy into released and dissipated.

σ_{ef} = scalar effective stress, of von Mises type (conceivable higher-order terms such as $\sigma_{ef}^3 \propto s_{km}s_{mn}s_{nk}$ are omitted). The numerical subscripts refer to Cartesian coordinates (x_1, x_2) and the summation rule applies. Note that the use of the deformation theory of plasticity in the HRR theory is a simplifying hypothesis. It is acceptable if no unloading occurs, and Hutchinson and Paris [79] showed it to be quite accurate.

3.4 Large-scale yielding in small structures

First we consider the case of large-scale yielding, in which the specimen or structure is so small that all of the fracture cross section is plastically yielding and full development of the yielding zone is prevented by the cross section size. We consider geometrically similar specimens of various sizes D, with similar cracks or notches. Based on the preceding arguments (Eq. 3.4), the absence of any characteristic length implies the near-tip stress field to have separated form:

$$s_{ij} = \sigma_y (r/r_p)^m \psi_{ij}(\theta) \tag{3.10}$$

where function ψ_{ij} cannot be expressed by an exact explicit form but can be approximated by several methods, e.g. finite difference method [80], [81], complex solution via conformal mapping [82], [83], and finite element method [84]. It is dimensionless and thus σ_y is required for dimensional consistency. Exponent m is a constant to be determined later, and r_p represents the effective size (or radius) of the yielding zone. Substitution (3.10) into the constitutive law, Eq. (3.8), furnishes:

$$e_{ij} = \alpha_p \epsilon_y (r/r_p)^{mn} \varphi_{ij}(\theta) \tag{3.11}$$

where $$\varphi_{ij}(\theta) = \tfrac{3}{2}\psi_{ij}(\theta)\left(\tfrac{3}{2}\psi_{kl}(\theta)\psi_{kl}(\theta)\right)^{\frac{n-1}{2}} \tag{3.12}$$

where φ_{ij} is also a dimensionless function. Since e_{ij} is expressed in terms of the gradient of displacement u_i, and since an integration increases the r-exponent by 1, the displacement field must have the separated form:

$$u_i = \alpha_p \epsilon_y r_p (r/r_p)^{mn+1} F_i(\theta) \tag{3.13}$$

where F_i are dimensionless functions. Evaluating the expression $\epsilon_{ij} = e_{ij} = \frac{1}{2}(u_{i,j} + u_{j,i})$, we can check that it agrees with Eq. (3.11). At the same time, we get an expression for the function $F_i(\theta)$ in terms of $\varphi_{ij}(\theta)$ (the subscripts preceded by a comma denote derivatives).

It is now useful to recall Rice's J-integral [64] giving the energy flux through the yielding zone into the fracture process zone:

$$J = \int_\Gamma \left(\bar{W}\mathrm{d}y - \nu_j\, s_{ij} u_{i,1} \mathrm{d}s\right), \quad \bar{W} = \int s_{ij}\mathrm{d}\epsilon_{ij} \tag{3.14}$$

where the flux is meant with respect to crack length a, not time; Γ is a closed contour around the crack tip, s is the length coordinate of that contour, ν_i its unit outward normal, $y = x_2$, $\partial_1 = \partial/\partial x_1$, and $\frac{1}{2}s_{ij}e_{ij}$ is the stored strain energy recoverable upon unloading and $\bar{W}$ is the nonlinear strain energy density. The material is considered as nonlinearly elastic, as if the unloading would follow the same curve as loading. This hypothesis is acceptable if the J contour avoids the zone of unloading in the wake of the advancing yielding zone. Elasticity, whether linear or nonlinear, is essential for the path independence of J-integral.

Consider now the J-integral for a circular path, for which $\mathrm{d}s = r\mathrm{d}\theta$ and $\mathrm{d}y = r\mathrm{d}\theta\,\cos\theta$. From this and from Eqs. (3.18)–3.20) it follows that the radial dependence of the the first term of J-integral is

$$\int_{-\pi}^{\pi} \bar{W}\mathrm{d}y \;\propto\; r^m r^{mn} r = r^{m(n+1)+1} \tag{3.15}$$

($\propto$ is the proportionality sign). The same must occur for the second term of J integral. Indeed,

$$\int_{-\pi}^{\pi} \nu_j s_{ij} u_{i,1} \mathrm{d}s \;\propto\; r^m r^{mn+1} r^{-1} r = r^{m(n+1)+1}. \tag{3.16}$$

Since the J-integral is path independent, the exponent of r must be zero, i.e., $m(n+1)+1=0$, or

$$\boxed{m = -\frac{1}{n+1}} \tag{3.17}$$

as noted in 1968 by Hutchinson [5] and Rice and Rosengren [4]. As a check, for the case of a linear elastic behavior, $n=1$, and Eq. (3.16) gives $m=-1/2$. As another check, $s_{ij}e_{ij}$ is known [4], [5] to be proportional to $1/r$ as the crack tip is approached, and this is obviously also satisfied. It should be noted that the power-law hardening is not realistic when $n > 20$ [4] and, although $-1/(n+1) \to 0$ for $n \to \infty$, a different solution is required for non-hardening plastic materials [73]. In practice, though, $n \leq 20$ suffices for most situations.

According to Eq. (3.17), Eqs. (3.10)–(3.13) for large-scale yielding in small structures now take the following particular form (same as Eqs. 5.3.10 in [75]):

$$s_{ij} = \sigma_y \left(\frac{r}{r_p}\right)^{-\frac{1}{n+1}} \psi_{ij}(\theta) \tag{3.18}$$

$$e_{ij} = \alpha_p \epsilon_y \left(\frac{r}{r_p}\right)^{-\frac{n}{n+1}} \varphi_{ij}(\theta) \tag{3.19}$$

$$u_i = \alpha_p \epsilon_y r_p \left(\frac{r}{r_p}\right)^{\frac{1}{n+1}} F_i(\theta) \tag{3.20}$$

The structure strength is normally characterized in terms of the nominal strength of structure, defined as $\sigma_N = P/bD$, where P is the applied load or load resultant, b is the structure width (for a two dimensional structure or specimen), and D is the characteristic structure size, measured

homologously on geometrically similar structures of different sizes. Thus σ_N is a load parameter with the dimension of stress. Obviously $\sigma_N \propto s_{ij}$ and $r \propto D$, considering small enough structures with large-scale yielding, in which the plastic yielding zone occupies the entire fracture cross section. Eq. (3.18) thus yields the size effect law (or scaling law):

$$\boxed{\sigma_N \ \propto \ \sigma_y \left(\frac{r_p}{D}\right)^{\frac{1}{n+1}}} \quad \text{(for large-scale yielding, small } D\text{)} \tag{3.21}$$

where proportionality constants irrelevant to size effect are omitted. Note that in the limit of $n \to 1$, this scaling law reduces to $\sigma_N \propto D^{-1/2}$, which is the case of linear elasticity (or LEFM) except that the material stiffness approaches zero. Although specimens or structures small enough to undergo large-scale yielding may be too small for current practical interest, Eq. (3.21) is nonetheless useful for anchoring the asymptotic matching of the small-to-large-scale yielding transition, which we pursue later.

3.5 For comparison—derivation of scaling law for quasibrittle structures with no plasticity

To derive the scaling law for small-to-large structure transition, we will need to generalize and reinterpret the approach used for quasibrittle materials [14], [15], [43], [77], [85], [86], and so we review it first. We begin by the expression for energy release rate in linear elastic fracture mechanics (LEFM): $\mathcal{G} = (\sigma_N^2/E')Dg(\alpha)$ where $\alpha = a/D$, a = crack or notch length, D = characteristic structure size, and $g(\alpha) = K_I^2/(D\sigma_N^2)$ = dimensionless energy release function of LEFM reflecting the structure shape (K_I = mode I stress intensity factor, $E' = E$ for plane stress or $E/(1-\nu^2)$ for plane strain, E = Young's modulus, ν = Poisson ratio). Replacing the crack length a with the effective crack length $a = a_0 + c_f$ where c_f is a material property characterizing the effective length of the FPZ, we have $\mathcal{G} = (\sigma_N^2/E')Dg(\alpha_0 + c_f/D)$ where $\alpha_0 = a_0/D$ and a_0 = length of the

stress-free crack (or notch). Taking the first two terms of the Taylor series expansion, and denoting $g_0 = g(\alpha_0)$ and $g_0' = \mathrm{d}g(\alpha_0)/\mathrm{d}\alpha$, we get $\mathcal{G} = (\sigma_N^2/E')D(g_0 + g_0'(c_f/D))$, or

$$\mathcal{G} = \mathcal{G}_s + \mathcal{G}_b \tag{3.22}$$

$$\text{where} \qquad \mathcal{G}_s = (\sigma_N^2/E')Dg_0 \tag{3.23}$$

$$\mathcal{G}_b = (\sigma_N^2/E')c_f g_0' \tag{3.24}$$

where $g_0 = g(\alpha_0), g_0' = [\mathrm{d}g(\alpha)/\mathrm{d}\alpha]_{\alpha_0}$. Setting $\mathcal{G} = G_f$ (material fracture energy), and solving for σ_N, we obtain, after rearrangements, the classical size effect law [43], [85], [86] (of Type 2) for geometrically similar quasibrittle structures with similar cracks or notches:

$$\sigma_N = \sqrt{\frac{E'G_f}{g_0'c_f + g_0 D}} = \frac{\sigma_0}{\sqrt{1 + D/D_0}} \tag{3.25}$$

in which $D_0 = (g_0'/g_0)c_f$ (transitional size), $\sigma_0 = (E'G_f/c_f g_0')^{1/2}$ (this law now underlies the ACI standard code provisions for scaling of strength of concrete structures; the material characteristic length, c_f, of concrete has been shown to be about $0.4l_0$, where $l_0 = E'G_f/\sigma_y^2$ = Irwin's characteristic length [24], [25]).

For test data fitting, it is useful that Eq. (3.25) can be rearranged to linear regression plot

$$Y = AX + C \quad \text{where} \quad X = D, \quad Y = \frac{1}{\sigma_N^2} \tag{3.26}$$

$$A = \frac{1}{\sigma_0^2 D_0}, \quad C = \frac{1}{\sigma_0^2} \tag{3.27}$$

Obtaining A and C by regression of test data, we can calculate G_f and c_f from the last equation. This method of measurement of materials fracture characteristics has become widely used for

concrete and geomaterials and has been embodied in the international standard recommendation of RILEM [28] (recently also endorsed by the ACI-446 Committee). Eqs. (3.25)–(3.27) apply even when the structures or cracks for different sizes D are not geometrically similar, but function $g(\alpha)$ is then different for each size.

3.6 Energy dissipation rates of small-scale yielding in large structures

Having reviewed the theory of fracture of plastic-hardening metals, we can now embark on a study of scaling. We will need the strain energy density $\bar{W}$ of the nonlinearly elastic material approximating the plastic-hardening metal. It is defined as

$$\bar{W} = \int s_{ij} \mathrm{d}e_{ij} \tag{3.28}$$

To calculate it, we multiply the right-hand side of Eq. (3.18) for s_{ij} by loading parameter μ. In addition, we must multiply the right-hand side of Eq. (3.11) by μ^n, and the expression for $\mathrm{d}e_{ij}$ by $n\mu^{n-1}$. Integrating from $\mu = 0$ to $\mu = 1$, we obtain the energy density

$$\bar{W}(r,\theta) = \frac{n}{n+1}\,\alpha_p \sigma_y \epsilon_y \,\frac{r_p}{r}\,\varphi_{ij}(\theta)\psi_{ij}(\theta) \tag{3.29}$$

Note that here and further we must use the effective radius r_p of the yielding zone instead of the radius r_p' of the larger energy matching zone. Evaluating $\int\int$[Eq. (3.29)] $r\,\mathrm{d}\theta\,\mathrm{d}r$, one finds that the total strain energy in the circle of radius r_p (per unit width in the transverse direction x_3) is:

$$W = \frac{n}{n+1}\,\alpha_p \sigma_y \epsilon_y r_p^2 \int_{-\pi}^{\pi} \varphi_{ij}(\theta)\psi_{ij}(\theta)\mathrm{d}\theta \tag{3.30}$$

After the entire yielding zone advances beyond a given point, the material gets unloaded. Al-

though the unloaded elastic strain energy $\bar{W}_e$ may be small and negligible, it is easy to include it in our calculations. Considering only the deviatoric stresses and strains, the elastic energy density is $s_{ij}s_{ij}/2G$. Since the elastic shear modulus $G = \sigma_y/\epsilon_y$, substitution of Eq. (3.10) shows that the strain energy density at point (r, θ) of the yielding zone is:

$$\bar{W}_e(r,\theta) = \tfrac{1}{2}\sigma_y\epsilon_y(r_p/r)^{2/(n+1)}\psi_{ij}(\theta)\psi_{ij}(\theta) \tag{3.31}$$

To obtain the strain energy release rate, $\mathcal{G}_b$, due to unloading of the entire yielding zone, the strain energy contained in this zone must be divided by the distance of travel to the next non-overlapping position of the zone (Fig. 3.2), which is the distance $2r_p$, equal to the diameter of the yielding zone approximated as circular. So,

$$G_e = \frac{1}{2r_p}\int_{-\pi}^{\pi}\int_0^{r_p} \bar{W}_e(r,\theta) r \,\mathrm{d}\theta \,\mathrm{d}r = r_p\,\sigma_y\epsilon_y\,Q_e \tag{3.32}$$

$$Q_e = \frac{n+1}{8n}\int_{-\pi}^{\pi} \psi_{ij}\psi_{ij}\,\mathrm{d}\theta \tag{3.33}$$

After the passage of the yielding zone through a fixed station, the irreversible work of plastic yielding does not flow into the crack tip but is dissipated by unloading of the plasticized material. Over the effective width, $2r_p$, of the yielding zone, the energy dissipation rate is

$$G_p = \frac{1}{2r_p}\int_{-\pi}^{\pi}\int_0^{r_p} [\bar{W}(r,\theta) - \bar{W}_e(r,\theta)] r \,\mathrm{d}\theta \,\mathrm{d}r$$

$$= \sigma_y\epsilon_y\, r_p\,(Q_p - Q_e) \tag{3.34}$$

where $$Q_p = \frac{n\alpha_p}{2(n+1)}\int_{-\pi}^{\pi} \varphi_{ij}(\theta)\psi_{ij}(\theta)\mathrm{d}\theta \tag{3.35}$$

3.7 Size effect on fracture strength of plastic-hardening structures

To exploit an analogy with the size effect mechanism in quasibrittle structures, we need to interpret Eqs. (3.22)–(3.24) physically. The energy release rates $\mathcal{G}_s$ and $\mathcal{G}_b$ correspond to two different zones in the structure: (i) $\mathcal{G}_s$ is the energy release from the undamaged, elastic, zone of the structure, which is proportional to D (approximately, though for $D \to \infty$ exactly), and (ii) $\mathcal{G}_b$ is the rate of energy release from the damage band, which is independent of D (the rates are considered with respect to crack length a, not time). This band is the zone trailed by the advancing FPZ of finite width $2r_p$ if the yielding zone is approximated as circular. Before fracture, the material in this band is under transverse tension proportional to σ_N.

Compared to quasibrittle materials, which are incapable of plastic yielding, the situation in metals is complicated by the presence of a plastic-hardening yielding zone, inserted between the damage zone and the elastic zone. The yielding zone (typically of millimeter dimensions) plays a triple role—first, it conveys energy flux J through the yielding zone to the FPZ (typically of micrometer dimensions) and, second, it also dissipates energy, at the rate G_p, as the plastically deformed material unloads in the wake of the yielding zone. However, aside from these two dissipation roles, there is a third role: as the yielding zone travels forward, it unloads, at the rate $\mathcal{G}_b$, the strain energy $(\gamma_c \sigma_N)^2/2E'$ initially stored in the band of width $2r_p$ trailed by the yielding zone (here γ_c is a certain stress concentration factor, which is independent of structure size D and which we absorb into the definition of σ_N).

The rates of energy release from the elastic part of the structure and from the band swept by the yielding zone must be equal to the rates of energy dissipation at the crack tip and in the trail of the yielding zone, Therefore,

$$\boxed{\mathcal{G}_s + \mathcal{G}_b = G_f + G_p} \tag{3.36}$$

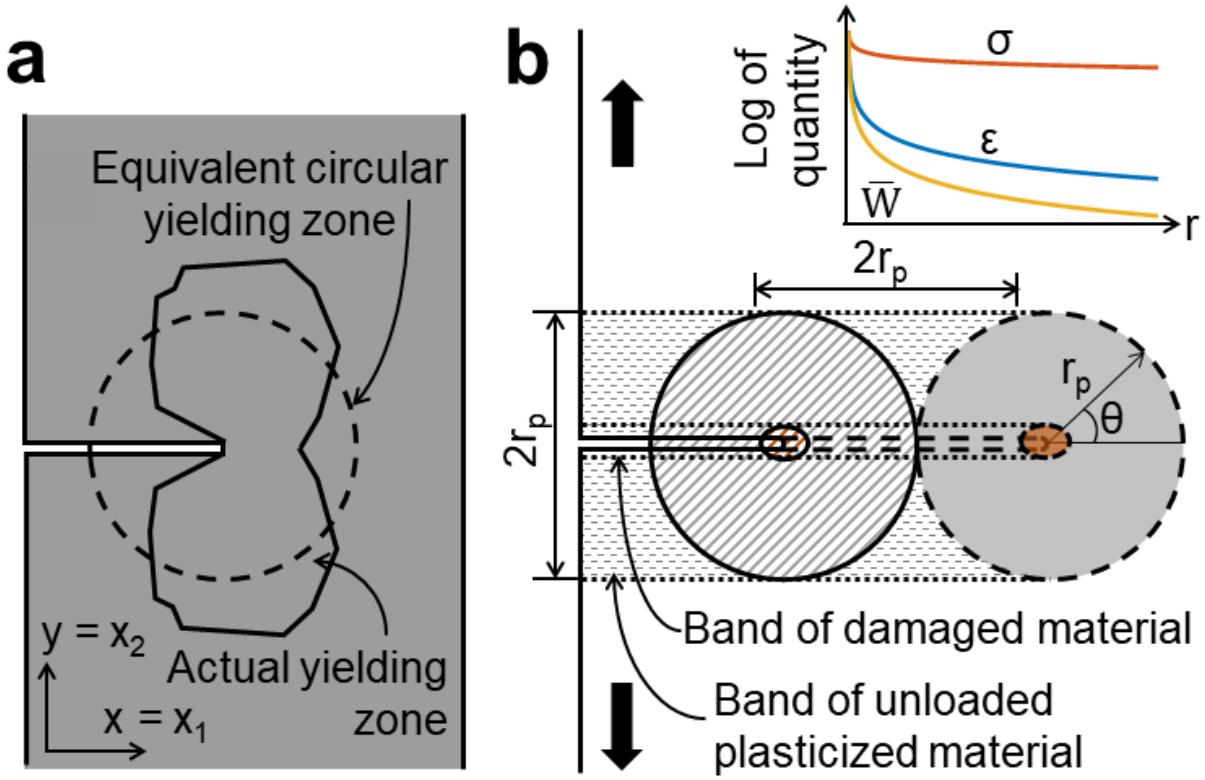

Figure 3.2: (a) Actual and equivalent yielding zones with the same area (or volume), as indicated by FE analysis using von-Mises type plastic-hardening constitutive law; (b) Propagation of the equivalent yielding zone as crack grows.

For $\mathcal{G}_b$ we can take the same expression as in Eq. (3.24) but with the damage band width, c_f, replaced by $2r_p$, i.e.,

$$\mathcal{G}_b \;=\; (\sigma_N^2/E')\,2r_p \tag{3.37}$$

For $\mathcal{G}_s$ we can co-opt Eq. (3.23) (this is a simplification which may be supported by the thermodynamic theory of material (or configurational) forces used by Herrmann et al. [87], [88] who observed, on that basis, that the crack widening gives approximately the same LEFM energy release rate as the crack extension; see Fig. 12.8 in [49] and [25] where this concept was refined and calibrated). Substitutions of Eqs. (3.23), (3.34), and (3.37) into (3.36) then yield the energy balance equation:

$$\frac{\sigma_N^2}{E'}\,Dg_0 + \frac{\sigma_N^2}{E'}\,2r_p = G_f + G_p \tag{3.38}$$

Solving for σ_N finally furnishes the size effect law:

$$\boxed{\sigma_N = \frac{\sigma_0}{\sqrt{1 + D/D_0}}} \tag{3.39}$$

This law has the same form as the size effect law, SEL, for quasibrittle materials (Eq. 3.25) but its coefficients are expressed differently and depend on the hardening exponent n:

$$D_0 = \frac{2r_p}{g_0}, \quad \sigma_0^2 = \frac{E'G_f}{2r_p} + \sigma_p^2, \tag{3.40}$$

$$\sigma_p^2 = \frac{E'\sigma_y\epsilon_y}{2}\,(Q_p - Q_e) \tag{3.41}$$

The asymptotes of size effect are also the same:

$$\sigma_N \underset{D\,\to\,0}{\Rightarrow} \sigma_0 = \text{constant}, \quad \sigma_N \underset{D\,\to\,\infty}{\Rightarrow} D^{-1/2} \tag{3.42}$$

3.8 Size effect method for testing material fracture properties in large enough structures in small-scale yielding range

Like Eq. (3.25), Eq. (3.39) can again be transformed to linear regression

$$\boxed{Y = AX + C} \quad \text{where} \quad X = D, \;\; Y = 1/\sigma_N^2 \tag{3.43}$$

$$A = 1/\sigma_0^2 D_0, \quad C = 1/\sigma_0^2 \tag{3.44}$$

If σ_N-values are measured for various D, and $\sigma_y, \epsilon_y, \alpha_p, E', n$, and if functions $\varphi_{ij}(\theta), \psi_{ij}(\theta)$ are all known, at least numerically, and if their integrals in Q_p and Q_e are evaluated (which could be done once for all), then the fracture energy G_f (equal to J_{cr}) and the effective width $2r_p$ of the yielding zone can be identified by testing the size effect. To this end, one must first determine the value of g_0 (and E'). Then one conducts linear regression of the measured data pairs (X, Y) according to Eq. (3.43), to get A and C, and calculates: $\sigma_0 = 1/\sqrt{C}$ and $D_0 = C/A$. Finally, if if even the smallest tested specimen is large enough to be in the small-scale yielding range, we have

$$r_p = \frac{g_0}{2\sigma_0^2 A}, \quad G_f = \frac{2r_p}{E'}\left(\frac{1}{\sqrt{C}} - \sigma_p\right) \tag{3.45}$$

3.9 Simple asymptotic matching of small-to-large-scale yielding

The small-size asymptote of Eq. (3.39), i.e. σ_N = constant, does not match the small-size large-scale yielding $\sigma_N \propto D^{-1/(n+1)}$ in Eq. (3.17) or (3.21). This is caused by considering, in our analysis, a different physical mechanism which is inappropriate for the range of transition from large-scale yielding to small-scale yielding. As the simplest, phenomenological, way to make the small-size asymptote match the power law $D^{-1/(n+1)}$ instead of D^0 without spoiling the large-size

asymptote $D^{-1/2}$, Eq. (3.39) may be modified as follows:

$$\boxed{\sigma_N = \sigma_0 \left(\frac{D}{D_0}\right)^{-\frac{1}{n+1}} \left(1 + \frac{D}{D_0}\right)^{-\frac{n-1}{2n+2}}} \tag{3.46}$$

or
$$\sigma_N = \sigma_0 \left(\frac{D_0}{D}\right)^{\frac{1}{2}} \left(1 + \frac{D_0}{D}\right)^{-\frac{n-1}{2n+2}} \tag{3.47}$$

This asymptotic matching formula cannot be derived by the previous asymptotic argument, and so it cannot be used for small specimens for which D is not much larger than r_p. This is not surprising because the derivation was purely phenomenological as it was not anchored in the rate of energy release from unloading of the material swept by the advancing yielding zone. We will try to remedy it next.

3.10 Small-to-large-scale asymptotic matching anchored in yielding zone

When the specimen or structure cross section, of size D, is smaller than the width, i.e, $D < 2r_p$, of the fully developed yielding zone, we have large-scale yielding, for which we must consider the restricted yielding zone width, which we denote as $2r = h_0 D$ where h_0 is a dimensionless constant. Similar to the argument for Eq. (3.21), we recognize proportionality to σ_N by replacing s_{ij} in Eq. (3.18) with σ_N, but replace now $2r_p$ with the restricted width $h_0 D$. This yields $\sigma_N = \sigma_0 (2r/h_0 D)^{\frac{1}{n+1}}$, from which

$$2r = (\sigma_N/\sigma_0)^{n+1} h_0 D \tag{3.48}$$

The linear elastic strain energy that was initially stored in the material and was subsequently released by the passage of the yielding zone is, per unit length in the x direction, $\mathcal{G}_b = (\sigma_N^2/E')(2r)$.

Replacing $2r$ in Eq. (3.48), we obtain

$$\mathcal{G}_b \;=\; \frac{\sigma_0^2}{E'}\left(\frac{\sigma_N}{\sigma_0}\right)^{n+1} h_0 D \tag{3.49}$$

If we substitute this equation, instead of Eq. (3.37), into the energy balance equation (3.36), we obtain, instead of Eq. (3.38), the following equation

$$\boxed{\frac{\sigma_0^2}{E'}\left(\frac{\sigma_N}{\sigma_0}\right)^{2} g_0 D + \frac{\sigma_0^2}{E'}\left(\frac{\sigma_N}{\sigma_0}\right)^{n+1} h_0 D = G_f + G_p} \tag{3.50}$$

in which only the second term differs from Eq. (3.38). The above equation may be rewritten as

$$AX^{n+1} + BX^2 = C \qquad \text{in which} \tag{3.51}$$

$$A = (\sigma_0^2/E')h_0 D,\;\; B = (\sigma_0^2/E')g_0 D,\;\; C = G_f + G_p,\;\; X = \sigma_N/\sigma_0 \tag{3.52}$$

It is proper to acknowledge that Eq. (3.48) was previously obtained in a different way by Kanninen and Popelar [75, pp.c314-317]. They replaced the fixed limiting width of the yielding zone (here denoted as $2r_p$) by a reduced width restricted by the specimen size (Eqs. 5.4-9 and 5.4-11 in [75]). With their empirical function ϕ they achieved a smooth transition. For notched three-point bend specimens, they calculated by finite elements and tabulated a function, $h_1(\alpha, n)$, that describes this transition for various relative crack lengths α. The present constant h_0 may be taken as equal to $\alpha_p(1-\alpha)h_1(\alpha_0, n)$.

To obtain the size effect of D on σ_N, one needs to solve X as a function of A, B, C from Eq. (3.51). Since an exact solution is not possible for $n > 4$ (according to Abel-Galois theorem), a numerical solution may be easily obtained by Newton iterations or, more effectively, by minimizing

the quadratic expression

$$\Phi = (AX^{n+1} + BX^2 - C)^2 \tag{3.53}$$

with an optimization algorithm such as Levenberg-Marquardt. Nevertheless, a very accurate closed-form analytical approximation is possible, as shown in the next section.

A tentative iterative procedure to identify the G_f and h_0 values from size effect tests may begin, in the first iteration, with a guess of the values of $G_f + G_p, \sigma_0$ based on a preliminary estimate by linear regression according to Eq. (3.43). Minimization of Φ then yields the optimum values.

3.11 Closed-form approximation of small-to-large-scale yielding and evaluation of size effect tests

We denote:

$$X_A = (C/A)^{\frac{1}{n+1}}, \;\; X_B = (C/B)^{\frac{1}{2}}, \;\; Y = X/X_A, \;\; m = X_A/X_B \tag{3.54}$$

by which Eq. (3.51) becomes

$$Y^{n+1} + m^2 Y^2 = 1 \quad \text{where} \quad m = \left(1 - Y^{n+1}\right)^{\frac{1}{2}} / Y \tag{3.55}$$

The real solution of this equation can be closely approximated by:

$$m = \left(Y^{-d} - 1\right)^{\frac{1}{d}} \quad \text{with} \quad d = \sqrt{2(n+1)} \tag{3.56}$$

and Y then follows from Eq. (3.54). Fig. 3.3 shows how close this approximation is. Note that this approximation does not depend on A, B and C. The maximum error occurs when $X \to X_A$

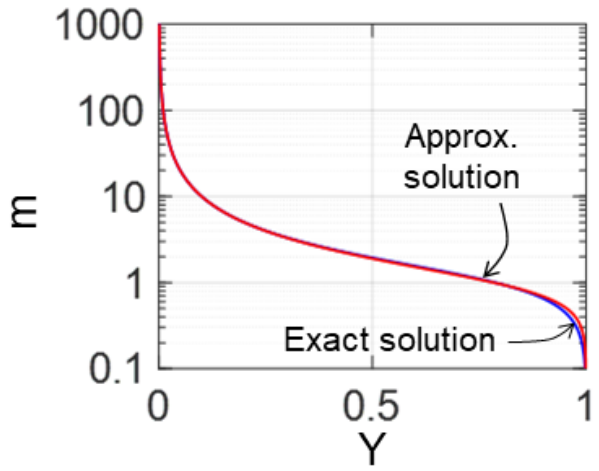

Figure 3.3: Comparison of accuracy of Eq. (3.56) in approximating the exact solution, Eq. (3.55).

or $D \to 0$ but these are not realistic cases.

The ratio σ_N/σ_0 obtained from this solution converges to LEFM (though not SEL) as $n \to 1$. It may further be checked that $\sigma_N/\sigma_0 \to (kD/D_0)^{-\frac{1}{n+1}}$ for $D \to 0$, and $\sigma_N/\sigma_0 \to (D/D_0)^{-\frac{1}{2}}$ for $D \to \infty$.

Identification of fracture properties from size effect tests is done by directly optimizing σ_0 and $G_f + G_p$ based on Eq. (3.53). The standard algorithm for nonlinear optimization in commercial software, such as Matlab, can be used.

3.12 Tests of notched specimens of aluminum and comparisons

A total of 12 notched three-point-bend (3PB) fracture specimens of aluminum (of type Al 6061-T651) have been manufactured (Fig. 3.4). The experiments involved 4 different sizes with the size range of $1 : 2 : 4 : 8$. Three identical specimens were tested for each size. The span-to-depth ratio was 6.0 and the relative notch depth was $a/D = 0.5$. The specimens of all sizes and their notches were geometrically similar in two dimensions but the transverse thickness, $b = 10$ mm, was kept constant (in order to avoid having to separate the size effects of plastic shear lip and of

3D singularity of stress field at the intersections of the crack front edge with the side faces).

The tests have been conducted in a MTS servo-controlled testing machine with load capacity of 10 kN and digital closed-loop controls. The built-in three-point-bend fixture of the system has been used as the test setup. Steel rollers have been placed at the load point and at end supports. The built-in load-cell and linear variable differential transformer (LVDT) have been employed and calibrated before testing. Displacement controlled loading was used. The loading rate was 0.002 mm/s for the smallest-size specimens. For larger sizes, the loading rate has been scaled so as to keep the strain rate approximately the same for all the sizes. The loading continued into the postpeak until the load dropped to 80% of the peak load.

Similar tests of aluminum have been conducted already in 1987 by Bažant, Lee and Pfeiffer [85], before the size effect theory was fully developed. Fig. 3.5 demonstrated that the size effect derived here matches these tests quite well.

3.13 The optimum fit of size effect law for ductile materials

The optimum fits of the results of the present tests of geometrically scaled aluminum specimens (the details of the experiments are presented in a later section), obtained with Eqs. (3.39), (3.46) and (3.53), are presented in Fig. 3.5 a,b,c. The transverse thickness of all specimens was not scaled and was kept as 10 mm (for the specimen details see the next section). For comparison, the results of the tests performed on the same type of aluminum by Bažant, Lee and Pfeiffer [85] (in 1987, before the size effect theory was sufficiently developed) are also shown and analyzed; see Fig. 3.5d,e,f. The specimen dimensions in those tests were in the same range as here, except for the transverse thickness which was 25.4 mm (1 in.).

The plastic dissipation G_p can be calculated directly if one has the data from the standard uniaxial tensile test and if one determines the angular variations ψ_{ij} and φ_{ij} of stress and strain

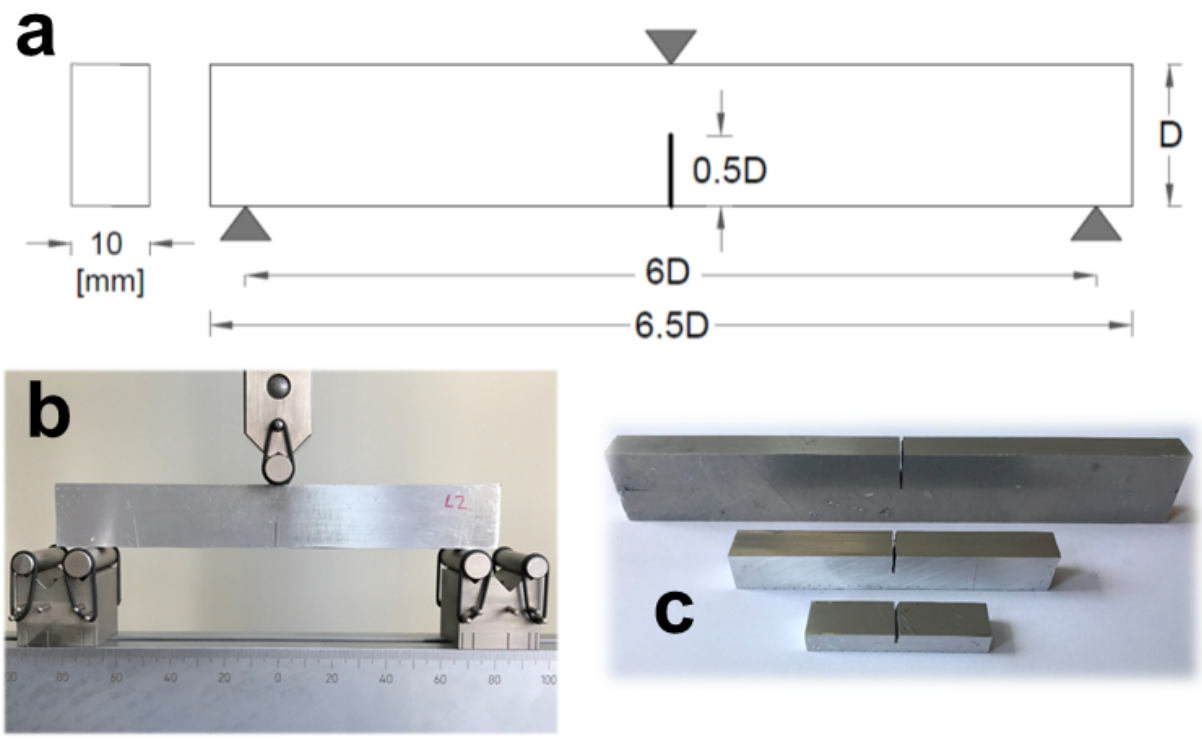

Figure 3.4: (a) Schematic and (b) actual setup of notched three-point-bend tests; (c) Geometrically-scaled specimens with the same transverse thickness and various depths, $D = 6, 12, 24$ mm (specimens with $D = 48$ mm were tested but not shown here).

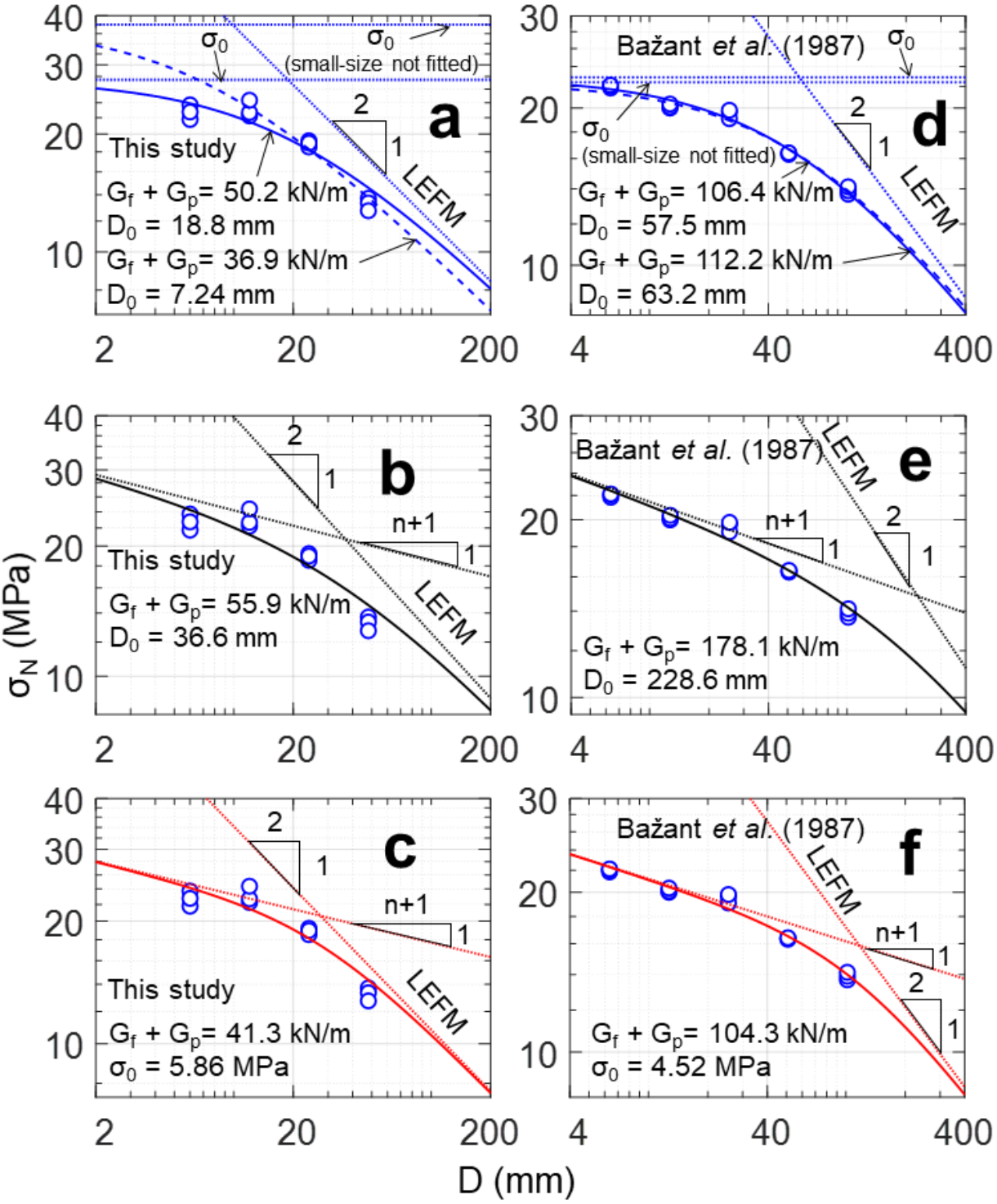

Figure 3.5: Optimum fits of size effect law to test result on aluminum beams based on: Eq.(3.39) (a,d), Eq.(3.46) (b,e), Eq.(3.50) (c,f). The transverse thickness of specimens was 10 mm (a,b,c), and 25.4 mm (1 in.) [85] (d,e,f).

(which can be done once for all for a given specimen geometry, e.g., the 3PB test). If this is unavailable, one can obtain only the sum $G_f + G_p$ as a whole, which is what is done here.

Even though the values of $G_f + G_p$ of the tested material (Al 6061-T651) obtained from Eqs. (3.39), (3.46) and (3.53) were in a reasonable range, some discrepancies need to be noted. Eq. (3.46) tends to give a higher $G_f + G_p$ than the other two. Due to the assumption of a fixed r_p in Eq. (3.39), choosing the data points in which the yielding zone is fully developed matters. This was reflected in Fig. 3.5a, in which the fitting of three larger sizes captured the data trend better and its resulting fracture energy was in agreement with Fig. 3.5c. So we consider this to be the true value of $G_f + G_p$. The same conclusion can be drawn from Fig. 3.5d,f. In this case, however, including or excluding the anomalous test result from the smallest specimen did not make a big difference.

According to [89], the transverse thickness has an appreciable effect. In large-scale yielding, the material at mid-thickness will begin yielding first. Because the material on the sides has not yet yielded, a plane-strain constraint develops at the middle part of the crack front edge, which creates a triaxial stress state. The larger the transverse thickness, the stronger the plane strain effect. This tends to increase $G_f + G_p$. Further tests are necessary to assess the magnitude of this effect as an envelope of fracture equilibrium curves.

The standard ASTM-E1820 [90] provides a guideline to measure the fracture energy of plastic-hardening materials. This includes the procedures for (a) the basic test of J_{Ic} and (b) the resistance curve (R-curve). The former requires a number of identical specimens to be loaded to different load levels, with several load-displacement curves to be recorded. This results in a J–Δa curve, based on which the J_{Ic} is obtained by interpolation. The latter method, on the other hand, demands only one specimen, but the loading procedure includes multiple loading-unloading cycles to keep track of the structure compliance. The proposed method which requires testing only the maximum loads of geometrically-scaled specimens of at least three different sizes seems relatively simpler.

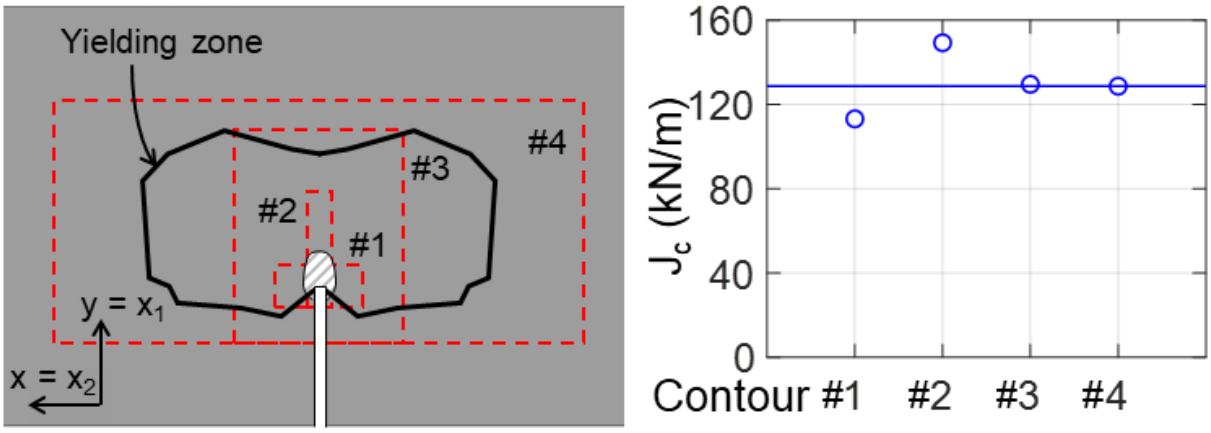

Figure 3.6: J-integrals on different contours, computed on the specimens with $D = 24$ mm and transverse thickness $b = 25$ mm (d,e,f). Path 3 and 4 indicate path-independence, but 1 and 2 not.

It is also related to the R-curve method, as documented in 1967 in [85] where the way to calculate the R-curve from the size-effect was shown.

To confirm the validity of the present method, finite element simulations of the tested material have been performed using a well established material model for metals presented in [91], [92]. Calibrating the material model with uniaxial tensile test data and the load-displacement curve of a specimen of one depth ($D = 24$ mm), J-integral calculations were run for various contours.

It is important to choose contours for which the J-integral is path-independent. They are those on which there is no inelastic unloading. For the contours in Fig. 3.6, if the contour crosses the plastically unloaded region or the damage region of the FPZ (e.g. 1 and 2), the calculated J-integral will be path-dependent. However, if the contour passes entirely through the HRR field, and not the FPZ, its value will be path-independent and will be the same as for an integral lying outside both zones. It is this value that is selected as the correct J_{Ic} of the material. This J_{Ic} (128.4 kN/m) differs by 16% from the J_{Ic} value obtained using the size effect method (112.2 kN/m).

3.14 Scaling for the FPZ-to-yielding transition and intermediate asymptote

When the specimen becomes smaller than the FPZ, which has a size in the micrometer range, the scaling is that of damage mechanics and is the same as for quasibrittle materials. Based on what is known for these materials [15], [93], the approach of the size effect curve to zero size must be linear. This translates, in the log-log scale, to an exponential, with a horizontal asymptote in that scale.

When the specimen becomes much larger than the FPZ but still significantly smaller than the yielding zone which (being of millimeter dimensions) is three order of magnitude larger, the large-size asymptote must be of the type $D^{-\frac{1}{n+1}}$. The simplest asymptotic matching formula then is

$$\sigma_N = \sigma_1 \left(1 + \frac{D}{D_1}\right)^{-\frac{1}{n+1}} \tag{3.57}$$

where σ_1 and D_1 are constants. This equation is valid only when D is smaller by at least one order of magnitude than the yielding zone size.

Considering the full size range from the FPZ to the specimen much larger than the yielding zone, we thus have three asymptotic regimes:

$$\sigma_N \propto D^0, \quad D^{-\frac{1}{n+1}}, \quad D^{-\frac{1}{2}} \tag{3.58}$$

The second is what Barenblatt named, and rigorously defined, as the intermediate asymptote [94] (Fig. 3.4). The intermediate asymptote $D^{-\frac{1}{n+1}}$ serves both as the large-size asymptote for the FPZ-to-yielding transition and as the small-size asymptote for the yielding-to-elasticity transition.

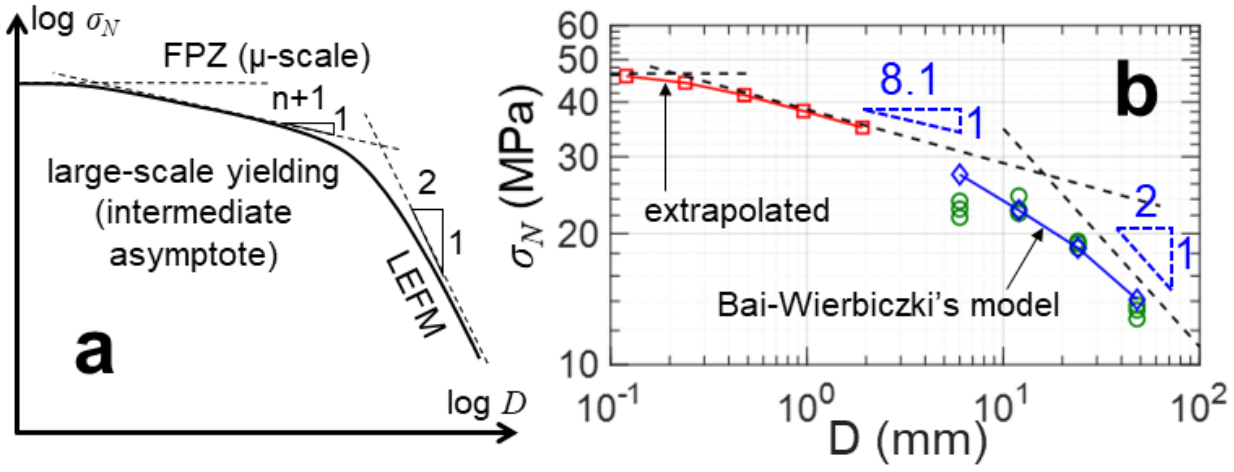

Figure 3.7: (a) Micron-scale asymptote for specimens with sizes comparable to process zone size (volume confined within slip planes or grain boundaries). (b) Simulated and extrapolated results by Bai–Wierzbicki [95] plasticity-damage model.

3.15 Numerical predictions

3.15.1 The Bai-Wierbiczki model and its prediction

To understand the mechanical behavior of the aluminum alloy for different structural sizes and crack-parallel stress levels (presented in the next chapter), we used a model that was claimed to capture the fracture behavior when the notch subjected to complex stress state, developed by Bai and Wierbiczki [95]. Even though more details can be found in Appendix A, the key of this model can be summarized below.

In this model, the Mohr–Coulomb (M–C) fracture criterion is revisited with an objective of describing ductile fracture of isotropic crack-free solids. This criterion has been extensively used in rock and soil mechanics as it correctly accounts for the effects of hydrostatic pressure as well as the Lode angle parameter. It turns out that these two parameters, which are critical for characterizing fracture of geomaterials, also control fracture of ductile metals [96]–[99]. The local form of the M–C criterion is transformed/extended to the spherical coordinate system, where the axes are the

equivalent strain to fracture $\bar{\epsilon}_f$, the stress triaxiality η, and the normalized Lode angle parameter $\bar{\theta}$. For a proportional loading, the fracture surface is shown to be an asymmetric function of $\bar{\theta}$. It was found that the M–C fracture locus predicts almost exactly the exponential decay of the material ductility with stress triaxiality, which is in accord with theoretical analysis of Rice and Tracey [100] and the empirical equation of Hancock and Mackenzie [101], Johnson and Cook [102]. The M–C criterion also predicts a form of Lode angle dependence which is close to parabolic. Test results of two materials, 2024-T351 aluminum alloy and TRIP RA-K40/70 (TRIP690) high strength steel sheets, were used to calibrate and validate the proposed M–C fracture model [95]. Another advantage of the M–C fracture model is that it predicts uniquely the orientation of the fracture surface. It is shown that the direction cosines of the unit normal vector to the fracture surface are functions of the "friction" coefficient in the M–C criterion. The phenomenological and physical sound M–C criterion has a great potential to be used as an engineering tool for predicting ductile fracture.

The scaling law predicted by this model were plotted against the experimental data in Fig. 3.7b. The model tends to result in a higher fracture energy, using either Eqs. (3.39), (3.46), or (3.50). Note that, even though the hardening YZ size is independent of the element size, the FPZ size is not. In fact, the element size should approximate the heterogeneity size, which is the size of poly-crystal grains. In fact, the void nucleation that causes softening is triggered by the mismatch in grain boundary excessive glide and climb. However, depending on the manufacturing method and how the materials are processed, this size may vary from 5-200 μm [103], [104]. In this case, the grain size encountered in the usual processing method, 40 μm [103], is considered. Consequently, the notch is considered blunt as its radius is one order magnitude larger than the element size.

3.15.2 The extrapolation to the micrometer scale

To observe the prediction of fracture behavior at the scale approaching the grain size mentioned above, the same set of parameters was applied to structures in which the ligament length was a few to several hundreds of micrometers. Note that the same notch radius and element size must be used based on the crack band theory [8]. This finding confirms the hypothesized micron scale asymptote; see Fig. 3.7b with a plastic hardening with power $n = 7.1$.

CHAPTER 4

THE EFFECT OF CRACK PARALLEL STRESSES ON DUCTILE MATERIALS

4.1 Yielding zone size under crack-parallel stress via energy matching of singular fields

Previously, we treated the effective radius of the yielding zone as a parameter to be fitted in the size effect formulation. In this section, we will present a method to approximate such a characteristic size based on the loading configuration and the crack parallel stresses.

Before studying the size effect, we also need an estimate of the effective size of the yielding zone, which we approximate as a circle of radius r_p. Furthermore, we must include the dependence of r_p on the crack-parallel stress $\sigma_{11} = T$ (in the case of plane stress), which represents the second term in the LEFM near-tip asymptotic series expansion. The first two terms of this expansion read [105]:

$$\sigma_{11} = \frac{K_I}{\sqrt{r}} f_{11}(\theta) + T \tag{4.1}$$

where $f_{11}(\theta) = \cos\theta'(1 - \sin\theta' \sin 3\theta')/2\pi$, $\theta' = \theta/2$ (e.g. p. 86 in[14]), and $K_I = \sqrt{E'G_f}$ = mode I stress intensity factor of the elastic field. The T-field in the second term is nonsingular and uniform. In small-scale yielding, the σ_{ij} field in Eq. (4.1) prevails at sufficient distance from the yielding zone (YZ). At closer range its interference with the plastic-hardening singular near-tip field given by Eq. (3.10) is complicated, and requires elasto-plastic finite element analysis (the typical contour of the small-scale yielding zone for plane stress, obtained by finite elements [5], is shown in Fig. 3.2).

As a simplification, the boundary between these two fields could be estimated by the intersection of radial profiles at which the stresses from both fields are equal (as suggested by Hutchinson

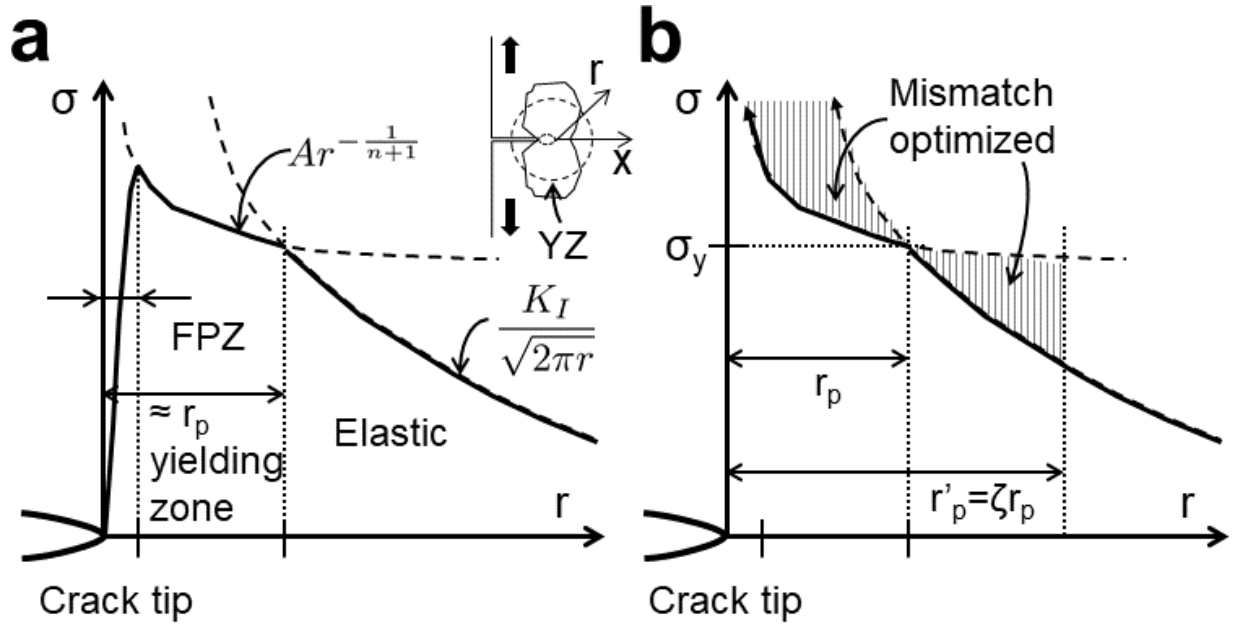

Figure 4.1: Schematic radial stress profiles; (a) intersection of yielding and elastic zones; and (b) mismatch areas (cross-hatched) for equilibrium matching of both zones by virtual work.

and Rice, and previously for perfect plasticity by Irwin). But this would still be complicated, giving r_p as a function of θ and T. Such a complication, though, is unnecessary for the global behavior such as the failure load and size effect. Besides, a dependence or r_p on θ would prevent us getting a clear result for the size effect.

In this light, we try (similar to [75]) to determine one effective constant value of transition radius r_p. To this end, we introduce a different approach—the use of the variational principle of virtual work to enforce global equilibrium, or overall energy equivalence, of the two interfering fields, Eqs. (3.18) and (4.1). With r_p defined as a constant, the stress at the intersection of the fields given by these two equations would, of course, not be equal to σ_y at each ray θ. The yield stress, σ_y, would be matched only in the average sense for all θ, and based on equilibrium in the crack direction (see Fig. 4.1).

Since T works on crack-parallel strain $\epsilon_{xx} = \epsilon_{11}$ in the case of plane stress, we match the two

singular fields by imposing, for a circle of a certain larger radius r_p' ($> r_p$, to be estimated later), the virtual work condition of overall equivalence of the stress resultants in crack direction x_1:

$$\int_{-\pi}^{\pi}\int_{0}^{r_p'} (\sigma_{11} - T)\, r\, \mathrm{d}\theta\, \mathrm{d}r\ \delta\epsilon_{11} = \int_{-\pi}^{\pi}\int_{0}^{r_p'} \hat{s}_{11}\, r\, \mathrm{d}\theta\, \mathrm{d}r\ \delta\epsilon_{11} \tag{4.2}$$

where $$\hat{s}_{11} = K_I\, r^{-\frac{1}{2}} f_{11}(\theta) \tag{4.3}$$

In the yielding zone, σ_{11} can be represented by s_{11} and expressed according to Eq. (3.18). Integrating, and noting that the resulting equation must be valid for any variation, we set the the multiplier of $\delta\epsilon_{11}$ to zero. This gives:

$$\frac{r_p'}{\zeta} = \boxed{r_p = \frac{C_e^2 l_0}{\zeta\,(C_n C_p - \pi T/\sigma_y)^2}} \tag{4.4}$$

where $$C_n = \zeta^{-\frac{1}{n+1}} \frac{n+1}{2n+1}, \quad l_0 = \frac{E' G_f}{\sigma_y^2} \tag{4.5}$$

$$C_e = \frac{2}{3}\int_{-\pi}^{\pi} f_{11}(\theta)\, \mathrm{d}\theta, \quad C_p = \int_{-\pi}^{\pi} \psi_{11}(\theta)\, \mathrm{d}\theta \tag{4.6}$$

Note that, for $T = 0$, the proportionality to l_0 is the same as in Eq. (5.4-10) of [75] but dimensionless factors C_n, C_e, C_p are different.

To estimate the factor ζ, we must give equal weights to the mismatches in the yielding and elastic zones. So we require that a half of the matching zone would lie within the yielding zone and the other half in the elastic zone, i.e., $\pi r_p'^2 = 2\pi r_p^2$. This yields $r_p' \approx r_p\sqrt{2}$. However, because of the approximate nature of energy matching, the factors C_e, C_p may best be determined by FEM or experiment. Note that, for the special case of $T = 0$, an estimate of r_p can be obtained in a different way in 1976 by Shih and Hutchinson [106]; they used the J-integral and superposed the displacements for the plastic-hardening and linear elasticity.

In addition to r_p, the effect of T will probably also change the energy dissipation in the FPZ,

represented by J_{cr} (or G_f), as confirmed for quasibrittle materials by the gap test [42], [76]. This is a separate question, which will be addressed theoretically and experimentally in a subsequent study.

Alternatively, Eq. (4.4) for r_p' can be obtained by least-square optimization of the matching of both singular fields, i.e., by minimizing the square of the difference between the two integrands in Eq.(4.2), integrated over the area of circle of radius r_p'. The minimizing condition based on the squares of the differences of stress resultant differences in the x_1 direction then is:

$$\frac{\mathrm{d}}{\mathrm{d}r_p'}\int_{-\pi}^{\pi}\int_{0}^{r_p'}\left[\sigma_{11}-T-\hat{s}_{11}\right]^2\, r\,\mathrm{d}\theta\,\mathrm{d}r\;=\;0 \tag{4.7}$$

We note that, r_p depends on the polycrystalline grain size indirectly via Hall-Petch effect [36], [107]. However, unlike the FPZ, YZ size is also affected by the loading configuration and the specimen's geometry.

4.2 Calculation of dimensionless angular functions and work expressions

The expressions for angular functions in Eqs. (3.18–3.20) were not presented in the preceding study [108]. However, they are needed to predict the mechanical response and size effect of the structural-scale strength when experimental data for calibration are unavailable or scant. Calculating the partial derivatives in the linearized strain expression $e_{ij}=\frac{1}{2}(u_{i,j}+u_{j,i})$, one finds the dimensionless angular function in Eq. (3.19) is:

$$\varphi_{ij}(\theta)=\frac{1}{2}\left\{\frac{F_i(\theta)\xi_j(\theta)+F_j(\theta)\xi_i(\theta)}{n+1}+F_i'(\theta)\xi_j^{\perp}(\theta)+F_j'(\theta)\xi_i^{\perp}(\theta)\right\} \tag{4.8}$$

where $\boldsymbol{\xi}(\theta)$ and $\boldsymbol{\xi}^{\perp}(\theta)$ are the unit position vector and its orthogonal counterpart. Functions F_i could, in theory, be also calculated from functions φ_{ij}. However, it would involve solving a stress

function that satisfies Eqs. (3.20–3.18) and boundary conditions numerically.

Because the Ramberg-Osgood constitutive law, Eq. (3.8), does not allow expressing s_{ij} in terms of e_{ij} explicitly, the calculation of strain energy density, $\bar{W} = \int s_{ij}\mathrm{d}e_{ij}$, is easier if we first calculate the density of complementary strain energy (or Gibbs free energy), which is defined as $W^* = \int e_{ij}\mathrm{d}s_{ij}$. Since it is path-independent, we get a general result even if we conveniently integrate along a proportional loading path, $s_{ij} = S_{ij}\eta$ where S_{ij} are constants, the loading parameter, η, runs from 0 to 1, and $S_{ij} = [s_{ij}]_{\eta=1}$. This way, $\bar{W}$ becomes an integral over η only. Noting Eqs. (3.19) and (3.18) and integrating, we get

$$W^* = \frac{\alpha_p \epsilon_y}{(n+1)\sigma_y^n} \left(\frac{3}{2}\, s_{ij} s_{ij}\right)^{\frac{n+1}{2}} \tag{4.9}$$

The density $\bar{W}$ of strain energy (or Helmholtz free energy) is a function of e_{ij}. However, since it is impossible to invert Eq. (3.8) in a closed form, we must express $\bar{W}$ in terms of s_{ij}. We can do so exploiting Legendre transformation $\bar{W} = s_{ij}e_{ij} - W^*$, which is derived by integrating $\int e_{ij}\mathrm{d}s_{ij}$ by parts. This gives

$$\bar{W} = \frac{n\alpha_p \epsilon_y}{(n+1)\sigma_y^n} \left(\frac{3}{2}\, s_{ij} s_{ij}\right)^{\frac{n+1}{2}} \tag{4.10}$$

Here s_{ij} must be regarded as functions of e_{ij}, given implicitly by Eq. (3.8). To obtain the J-integral, we must also evaluate

$$\nu_j s_{ij} u_{i,1} = \nu_j \alpha_p \epsilon_y \sigma_y \left(\frac{r}{r_p}\right)^{-1} \psi_{ij}(\theta)\chi_i(\theta) \tag{4.11}$$

$$\text{where} \qquad \chi_i(\theta) = \frac{F_i(\theta)}{n+1}\,\xi_1(\theta) + F_i'(\theta)\xi_1^{\perp}(\theta) \tag{4.12}$$

The J-integral may now be calculated at $r = r_p$:

$$J = \alpha_p \epsilon_y \sigma_y r_p \kappa \tag{4.13}$$

$$\text{where} \qquad \kappa = \int_{-\pi}^{\pi} \left[\nu_1 \frac{n}{n+1} \left(\frac{3}{2} \psi_{ij}(\theta) \psi_{ij}(\theta) \right)^{\frac{n+1}{2}} - \nu_j \psi_{ij}(\theta) \chi_i(\theta) \right] \mathrm{d}\theta \tag{4.14}$$

4.3 Gap Tests of Aluminum

All the standard fracture specimens happen to have zero or negligible normal stresses $\sigma_{xx}, \sigma_{zz}, \sigma_{xz}$ parallel to the crack plane (x, z). The obvious reason is that cracks are normally imagined as planes, having zero thickness. If that were true, then $\sigma_{xx}, \sigma_{zz}, \sigma_{xz}$ could have no effect on crack propagation. In reality, however, the fracture process zone (FPZ) at the front of every crack (probably even cracks in an atomically perfect lattice) has a finite width δ_y. This is the basic feature of the blunt crack [109] and crack band [8], [110] models, which indicated already in 1979 that, if δ_y is finite, the effect of $\sigma_{xx}, \sigma_{zz}, \sigma_{xz}$ ought to be significant, that the damage tensor in the FPZ must play a role, and that the scalar stress-displacement law of the cohesive (or fictitious) crack model is an insufficient characterization of fracture. Some role of the crack-parallel stress in concrete has long been suspected by a few investigators [8], [22], [109], [110], but a simple unambiguous test was lacking until the development of the gap test in 2020 [42], [76], [108].

For a detailed description of the gap test, see [76]. Briefly, the end supports of a standard notched three-point bend beam are installed with suitable gaps and, next to the notch, the specimen is supported by elastoplastic pads (Fig. 4.2a). Under vertical load at midspan, the pads first generate a field of crack-parallel compressive stress σ_{xx}, which is almost uniform near the notch tip. When the pads begin yielding, at nearly constant load, the end gaps close (Fig. 2.2a) and then the end reactions begin applying a bending moment, which produces mode I loading at the crack

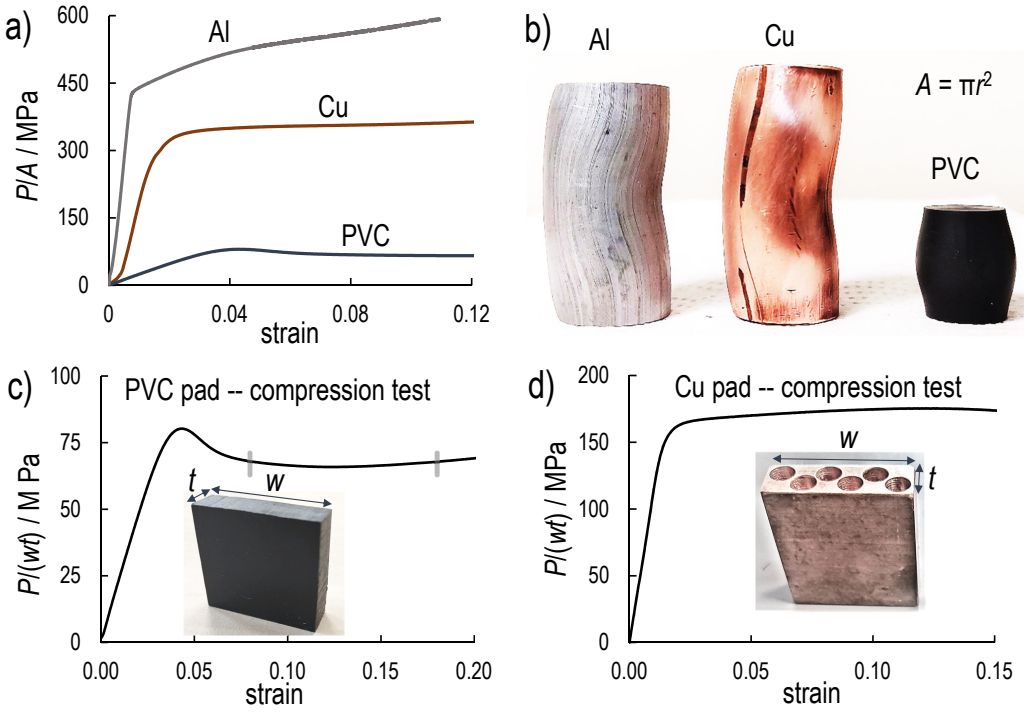

Figure 4.2: (a) Uniaxial stress-strain curves of aluminum (Al), copper (Cu) and polyvinyl-chloride (PVC); (b) The deformed shapes of Al, Cu and PVC loading pads after compression test; (c,d) compression tests of PVC pad and perforated Cu pad.(Note: w and t are the cross sectional dimensions and r is the radius).

tip. For evaluation it is advantageous that the load-support system is statically determinate, both initially and after the gaps close while the pads yield.

Another advantage is that one can apply the size effect method [86], [108] to determine the fracture energy, G_f, and the combined size of the yielding zone and the FPZ. To this end, the test must be carried out on scaled specimens of several sufficiently different sizes.

The gap test has originally been applied to concrete [42], [76]. Soon it was extended to metal [108] using the theory summarized above (gap tests of shale, fiber concrete and fiber composites are also under way). The limited preliminary gap tests of aluminum mentioned in [108] have now been extended and are reported here.

Polypropylene pads of the right shape were found to yield at the right stress level for concrete [42]. But, for the aluminum, supporting pads made of PVC and pure copper (Cu) had to be used to provide the right yield limits for the smaller and larger specimens, respectively. To characterize their basic properties, these three elastoplastic materials were tested according to the ASTM standards—E9-19 for Al and Cu, and D695-15 for PVC. Fig. 4.2a shows the stress-strain results of the cylindrical specimens with diameter $2r = 20$mm and height $H = 60$mm for Al and Cu, and $2r = 15$mm and $H = 30$mm for PVC. The strain rates were 0.005 mm/s for the metals, and 0.0008 mm/s for the PVC. The deformed shapes are shown in Fig. 4.2b. The plastic buckling and bulging seen in the figures occurred after the peak load, which is for the gap test irrelevant.

Additional compression tests of Cu and PVC were carried out on specimens of the same shape as the pads used. The stress-strain curves recorded are shown in Fig. 4.2c,d for the PVC and Cu. The plastic plateaus of the pad materials, required for the crack parallel stress levels in the notched Al beams, were -67 MPa and -172 MPa. Since the yield strength of Cu, 355 MPa, is much higher then 172 MPa, the average stress in the pads had to be reduced. This was achieved simply by drilling holes in the Cu pad, as seen in Fig. 4.2d.

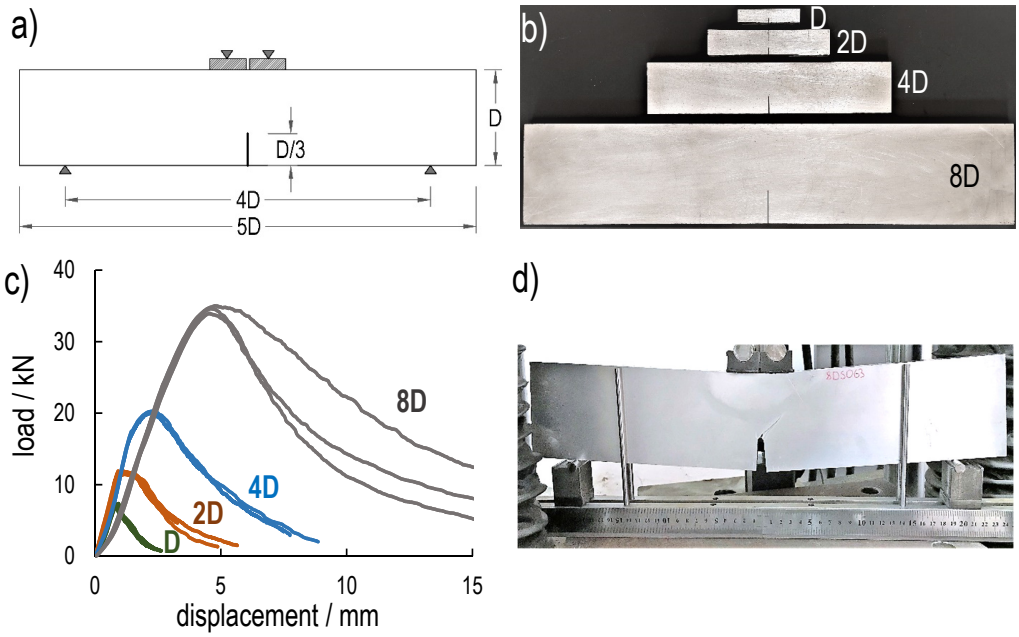

Figure 4.3: (a) The geometry of the Al specimens used; (b) Geometrically similar specimens of four scaled sizes; (c) The load-deflection curves of the scaled specimens; (d) Failure and grown crack image in 8D sized specimen.

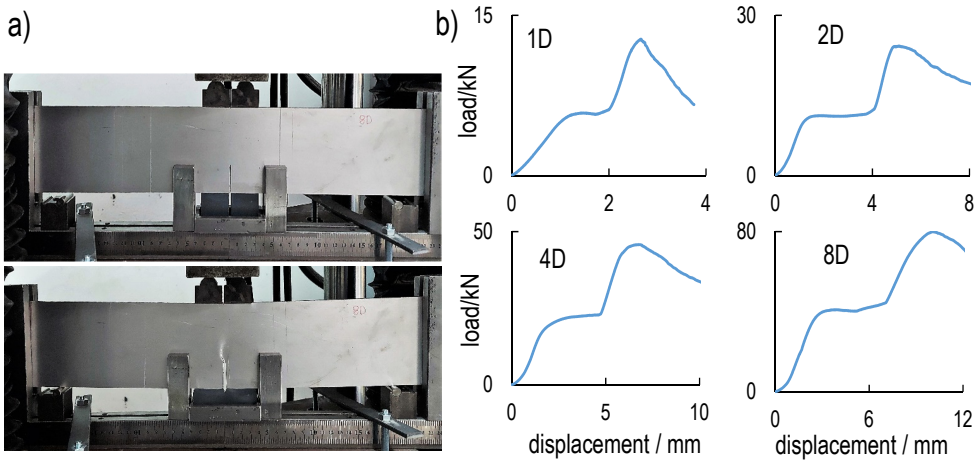

Figure 4.4: (a) The loading scheme of the gap tests using PVC pads and corresponding failure and cracking; (b) The load-deflection curves of the gap tests using PVC pads generating a 67 MPa crack-parallel compression in the Al specimens.

The notched beam specimens of aluminum, scaled geometrically in 2D, with the same width of 10 mm, are shown in Fig. 4.3a,b. Their depths are 12, 24, 48 and 96 mm. Figs. 4.3c,d show the results of standard three-point bend tests (with no gaps, no pads). The largest specimen, as deformed in postpeak softening, is seen in Fig. 4.3d. It is restrained by stiff vertical straps to prevent lateral buckling. In smaller specimens the buckling restraint was unnecessary.

Stronger supports against lateral buckling had to be used in the specimens with pads, as seen in Fig. 4.4a and 4.5a on the left. On the right, one can see 8 recorded load-deflection curves with Al and Cu pads, generating compressive crack-parallel stresses -67 MPa and -172 MPa. The second rising portions of the curves represent the effect of the bending moments after the gaps at beam ends have closed (the initial convex curvatures are due to gradual seating of the pads or beam end supports, which must be disregarded).

Ideally, a near-horizontal plateau controlled by the pads should have developed on these curves before reaching the ”hill” with the second rise of load. Such a plateau, however, has been attained at only 4 of the 8 curves in Figs. 4.4–4.5, but unfortunately not in the remaining 4 curves. It was not

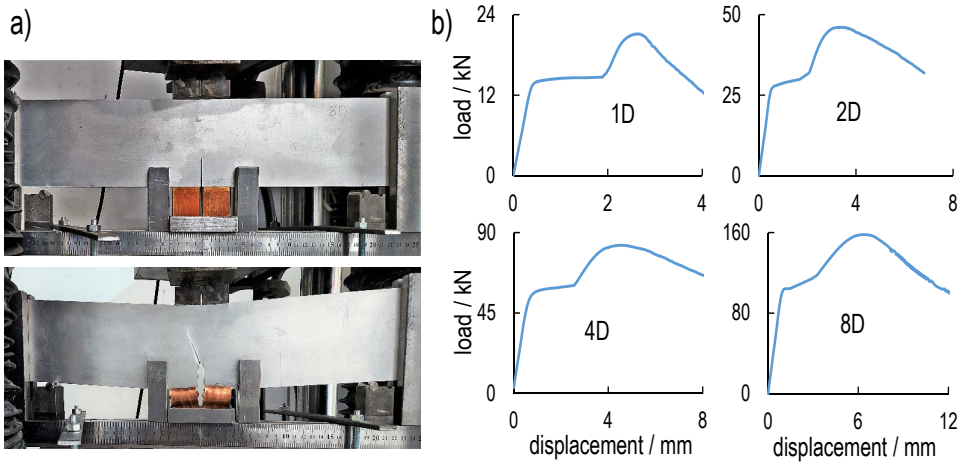

Figure 4.5: (a) The loading scheme of the gap tests using Cu pads. and the corresponding failure and cracking; (b) The load-deflection curves of the gap tests using Cu pads that generate a 172 MPa crack-parallel compression in the Al specimens.

possible (due to funding limitations) to repeat these tests with bigger gaps or with some different pads, so as to achieve a plateau. However, what matters is the stress on the pads at the peak load (hidden below the ”hill”). Though unidentifiable from these diagrams, it was assumed that an invisible plateau has been reached under the peak loads in these three diagrams. This assumption is supported by the systematic trend of the results plotted in Fig. 4.6a,b.

4.4 Aluminum test results and their discussion

The data points in Fig. 4.6a show the measured nominal strengths σ_N for scaled gap tests of 4 different sizes D = 12, 24, 48, 96 mm, and for 3 different levels of crack-parallel stress for the three nominal stress levels σ_{xx} relative to the yield strength f_y (note that compression is negative while f_y is considered positive). The 3 solid curves represent the optimal fits of the data points with the size effect law, Eq. (3.25) (based on the parameters obtained from the linear regression plots in Fig. 4.6a,b). Note the systematic trends of the data points. For the three stress levels, the

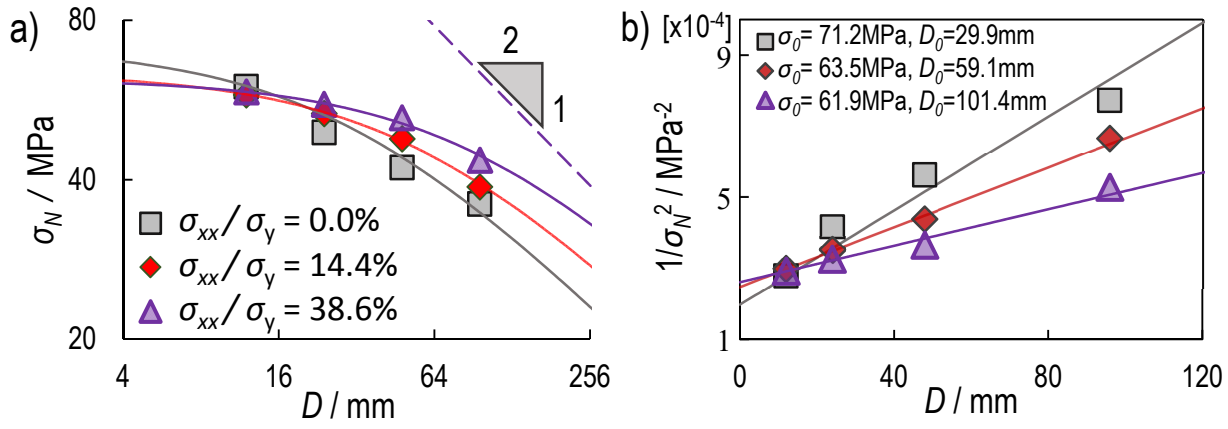

Figure 4.6: (a) Measured size effect data of aluminum for four different specimen sizes D and three different ratios of crack-parallel stress σ_{xx} to yield strength f_y in logarithmic scales; (b) ditto in a linear regression plot (the square and triangle data points give averages of 3 tests, the diamond data points the averages of 2 tests)

coefficients of variation of regression errors (defined as the root-mean-square error divided by data mean) are 9.7%, 1.5% and 6.2%, which is quite low. The fact that these trends are so systematic lends credence to our assumption that the lack of visible plateau in Fig. 4.5 did not spoil the results significantly.

Further note in Fig. 4.6a that the LEFM size effect slope of $-1/2$ is still far from being attained, even for the largest specimens. This means that a much larger size would be needed to attain LEFM behavior (i.e., the small-scale yielding range). Also note that what determines the fracture energy G_f is the position of the LEFM asymptote of slope $-1/2$, which is marked by a dashed line for each curve. The shift of the asymptote to the right means an increase of G_f. Obviously, these asymptotes for the three levels of σ_{xx} are shifted relative to each other (Fig. 4.6a), which means that the G_f values for different σ_{xx} are quite different (Fig. 4.6).

Fig. 4.6b shows the same test results in the linear regression plot of $1/\sigma_{xx}^2$ versus D [86]. The slope of the regression line is $1/G_f$. Once G_f is determined, one can get from the intercept the effective size r_p of the yielding zone ([86]). The fracture energy values obtained in this manner are

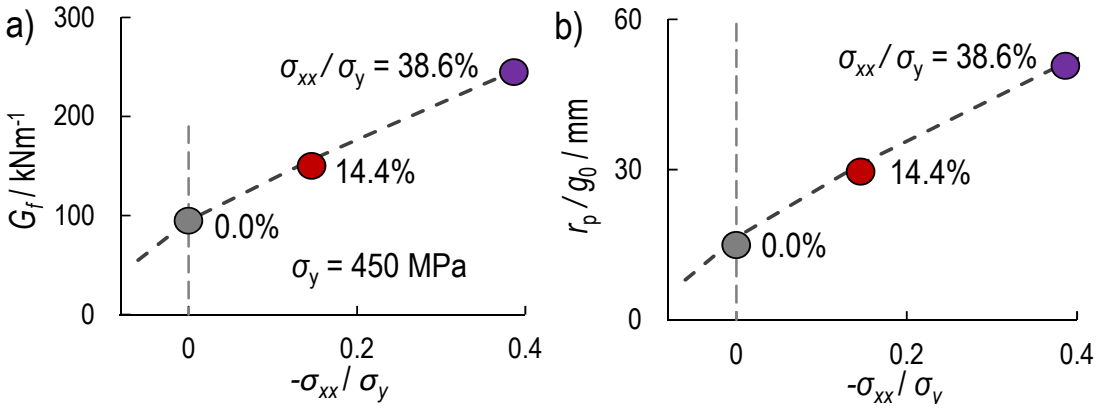

Figure 4.7: Experimentally obtained data on (a) the dependence of fracture energy G_f of aluminum on the ratio of crack-parallel compressive stress σ_{xx} to yield strength σ_y; and (b) ditto for the dependence of the characteristic size r_p of the fracture process zone.

plotted in Fig. 4.7 for the three levels of crack-parallel stress σ_{xx} used in the tests. From the linear regression shown in Fig. 4.6b, we may also infer a strong variation of the combined effective width r_p of the millimeter-scale yielding zone and the micrometer-scale fracture process zone.

The increase ΔG_f of G_f with increasing crack-parallel compression σ_{xx}, as seen in Fig. 4.7a, is remarkably strong (stronger than for concrete). A major part of ΔG_f variation is due to the effect of σ_{xx} (or T-stress) on the yielding zone of a millimeter-scale width, which has been well known since the 1980s [30], [31], [35]. The question is whether a part of ΔG_f, if any, may be due to the interaction of σ_{xx} with the micrometer-scale fracture process zone (FPZ), which is embedded within the yielding zone. Doubtless the FPZ has a finite width of micrometer dimensions, several times larger than the crystal size (but still 3 orders of magnitude smaller than the yielding zone).

To assess what part G_{FPZ} of the ΔG_f gets dissipated within the micrometer-scale FPZ, one could, in theory, use the nano-to-micro scaling law $\sigma_N = \sigma_1(1 + D/D_1)^{-1/(n+1)}$, given by Eq. 64 in [108], and then proceed in the same way as in [86]. To that end, however, one would need to calculate the hardening-plastic energy release rate of a theoretically sharp line crack (or slit) within a plasticized specimen of the given geometry, which is not available and would be quite

tedious to determine. To do it experimentally, one would need to fabricate geometrically scaled notched specimens of several sizes, with cross sections ranging roughly from 0.01 mm to 0.1 mm. One could also use finite element analysis on the micrometer scale. But that would require developing a realistic micrometer-scale constitutive damage model for the metallic polycrystal. All these studies would be quite demanding and are beyond the scope of this study.

Nevertheless, the part G_{FPZ} of the ΔG_f can be estimated from the observed size effect curves in Fig. 4.6, based on the fact that, for the same T-stress, the size of the yielding zone for specimens of different sizes D is about the same (as transpires from finite element simulations). This means that the energy dissipation in the wake of the yielding is, for the same T, independent of D. Hence, the difference in the size effect curves from the gap tests, seen in Fig. 4.6a, must be ascribed to a change in the energy dissipation in the micrometer scale fracture process zone of the polycrystal. So the variation of G_f and r_p shown in Fig. 4.7a,b (for $\sigma_{xx} \leq 0.4 f_y$) must be due to a change of both the FPZ (at the micrometer scale) and the yielding zone. However, this change was approximately 10-30 mm, indicating a much more significant contribution from the yielding zone. To distinguish the contributions from these two zones requires either micrometer-scale gap tests or numerical simulation results from a reliable constitutive law. The latter is presented in the following section.

A noteworthy point is that the size effect curves in Fig. 4.6a and b cross each other, and the effect of σ_{xx} gets reversed at the small size limit (as also marked in Fig. 4.8a). The reason doubtless is that the small size asymptotic limit of the size effect law is a crack filled by a perfectly plastic material, which may be reasonably described by the Mohr or von Mises yield envelope; see Fig. 4.8b. On the envelope one can see that increasing the magnitude of compression, $|\sigma_1|$, causes a drop in the transverse principal stress, $\sigma_2 = \sigma_{yy}$, which controls the small-size asymptote.

A comparison with concrete is instructive. Fig. 4.8d shows the diagram of the dependence

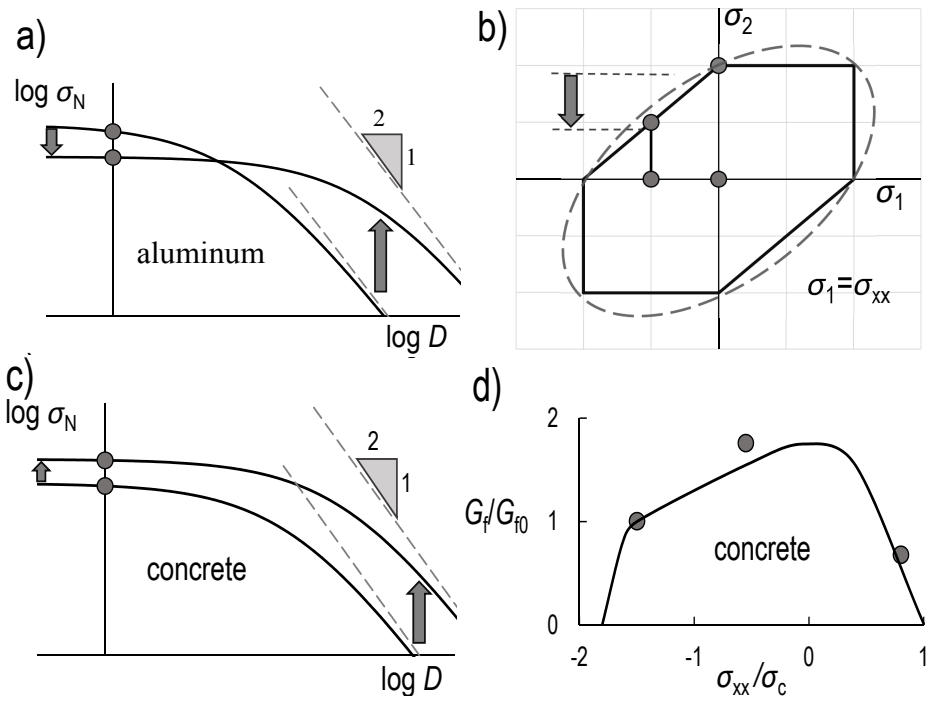

Figure 4.8: (a) Size effect curves of aluminum in logarithmic scales for $\sigma_{xx} = 0$ and for large σ_{xx} $(= T)$; (b) Mohr and von Mises yield envelopes of metals; (c) size effect curves of concrete, showing, for comparison, that for quasibrittle materials the curves do not cross; (d) dependence of G_f on σ_{xx} in concrete.

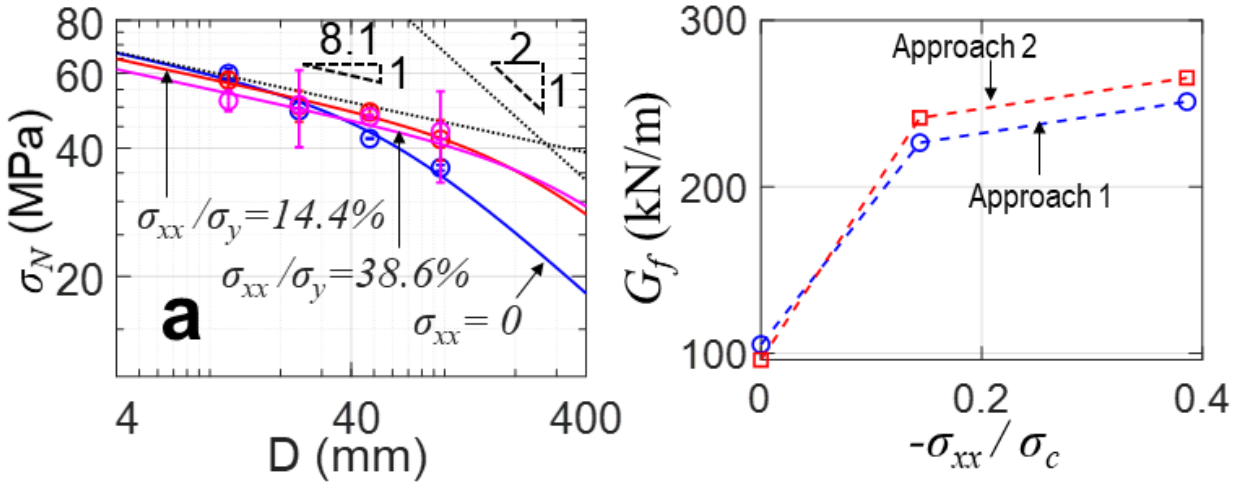

Figure 4.9: (a) The fitted fracture energy resulted from Eq. 3.50; (b) The variation of G_f with different σ_{xx}.

of G_f of concrete on σ_{xx}/f_c recently obtained experimentally [42], [76] (here f_c = compressive strength of concrete). At the compression limit, $\sigma_{xx} = f_c$, this diagram drops to a zero value of G_f. Could the same behavior be expected for aluminum? Certainly not. Although no tests for $|\sigma_{xx}| > 0.4f_y$ have been conducted for aluminum, the diagram of G_f versus σ_{xx} must end at the yield limit $|\sigma_{xx}| = f_y$ with a significant value of G_f.

Another difference is seen in the size effect curves. For concrete, these curves, shown in Fig. 4.8c, do not cross on approach to the small-size limit, unlike those for aluminum. Again, the reason is that in concrete, at the uniaxial tensile strength limit there is no yielding plastic material bridging the crack, regardless of the size.

Note that we also used Eq. 3.50 to fit these results and by no surprise, the G_f at zero σ_{xx} resulted from both approaches are quite close (see Fig. 4.9). This is owing to the fact that, unlike the experiment mentioned in the previous chapter, we used the smallest size ($D = 12mm$) that has the ligament length is approximate to the size of the YZ.

However, the difference seems to arise at different σ_{xx}'s. In particular, fitting to Eq. 3.50 would result in a higher values of G_f than Eq. 3.38. This is due to the fact that, as σ_{xx} increases, the effective yielding zone, r_p would evolve and exceeds the ligament length of smaller sizes. This will shift the nature of the problem from small-scale to large-scale yielding and a transitional fitting is necessary. In addition, fitting to Eq. 3.50 is more informative in a sense that, when such a small-to-large-scale yielding happens, the power law portion of the optimized curves are extended to a larger D regime, hinting the extension of the power-law $-1/(n+1)$ applicability.

4.5 The effect of T-stresses via Bai-Wierbiczki model

4.5.1 The prediction with σ_{xx}

In this section, the experimental results will be fitted using the Bai-Wierbiczki plasticity-damage model mentioned in the previous chapter. The results show an increase of the fracture energy G_f with no presence of a crossing point when size increases. However, neither the fitted G_f using the nominal strength of structure with different sizes nor the change of such value with different σ_{xx} is quantitatively correct. Therefore, only the trend is discussed here. Fig. 4.10a shows that the presence of σ_{xx} increases the nominal strength of structures at any size.

When σ_{xx} increases, the energy release rate will increase due to the enlargement of the YZ size (or r_p). This increase is monotonic because the constraint is further enhanced with the hardening plasticity in the crack front; see Fig. 4.10a,b. This is evidenced by the plot of the yielding zone of the beam of size $D = 48mm$. The slope of these curves, however, follows strictly the slope of the material point's constitutive law $-1/(7.1+1)$ with an extension of this regime to a larger D.

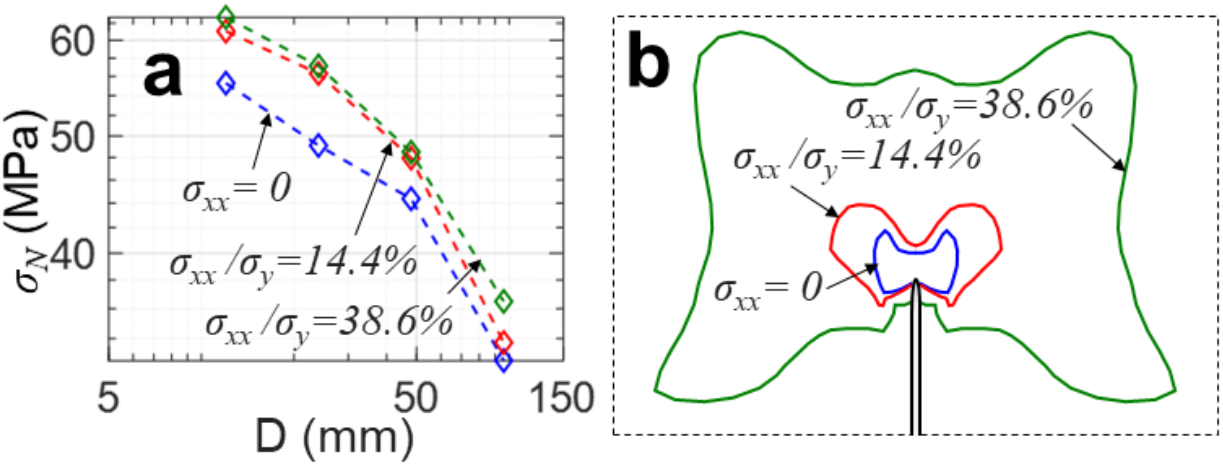

Figure 4.10: (a) The prediction of the size effect of aluminum alloy using Bai-Wierbiczki's model; (b) The corresponding change of the YZ as σ_{xx} increases.

CHAPTER 5
THE EFFECT OF THE CRACK-PARALLEL STRESS IN OTHER MATERIALS AND THE IMPLICATION OF THE GAP TEST RESULTS IN DIFFERENT ENGINEERING PROBLEMS

5.1 The applicability to other materials

5.1.1 Fiber reinforced concrete (FRC)

Short random fibers change significantly the post-peak softening damage in concrete. Microplane model M7f was calibrated to capture it [111] and has been used to simulate G_f for the present specimen geometry; see Fig. 5.1a,b. Due to the lack of material for calibration, we extrapolated the currently used model to account for the presence of fibers. First, the parameters for plain concrete were determined from calibration as described in section 2. Later, the parameters related to fibers were obtained from [111] as if 3% Dramix fiber was mixed to the same batch of concrete. Later, the same set of different specimen sizes were numerically tested and results were provided in Fig. 5.1a,b. Note that, this procedure is compliant with the calibration of M7f for FRC.

The presence of fibers enhanced the cohesive strength and the crack bridging effect, which gives a higher G_f at zero σ_{xx}. Therefore, a mild increase of σ_{xx} also showed a relative increase in G_f, but with a lower magnitude. This was probably stemming from the fact that the effect of fiber on the friction boundary is weaker than on the normal boundary of M7, i.e., the fibers are more effective in bridging the opening micro-cracks rather than preventing their sliding. Furthermore, the decline of G_f towards zero is more gradual than in plain concrete. This phenomenon originates from the inhibition of splitting micro-cracks, so that a higher σ_{xx} is needed to cause slip expansion

and energy dissipation becomes more gradual (see Fig. 2.8).

5.1.2 Shale

The recently developed sphero-cylindrical microplane model for shale [112], intended for the simulation of hydraulic fracturing, can capture the effect of anisotropy due to bedding layers on the damage development in shale. The orientation of the crack plane relative to bedding layers matters. Because the overburden pressure is about the double of the horizontal tectonic stresses and the bedding layers are nearly horizontal, we simulate a shale specimen of the present geometry with a crack normal to the bedding layers. For comparison, we add the case of a crack parallel to the bedding layers. The resulting curve of G_f versus σ_{xx} is shown in Fig. 5.1c,d. In the case of the crack normal to the bedding plane, the crack must cut through these layers which are stronger than the interlayer material. Thus a higher energy release is required, which explains why compressive σ_{xx} leads to much higher relative G_f-values than those for cracks parallel to bedding layers, as seen in Fig. 5.1c.

5.2 Crack-parallel stresses at nanoscale

5.2.1 The fracture response of pristine transition metal dichalcogenides and the brittleness of covalent bonds

Not until recently, an accurate measurement of J-integral have been achieved for 2D materials. This study uses $MoSe_2$ and MoS_2 (both belong to a group of semiconducting materials called transition metal dichalcogenides, or TMDs) as case study. The results are accompanied by an optimizing framework that combines the thorough optimizing power on the global scale of a multi-objective genetic algorithm–NSGA [113] and the stability of a local optimizer [114] which uses the correlation between the optimized physical properties on the Pareto front. Note that the optimization

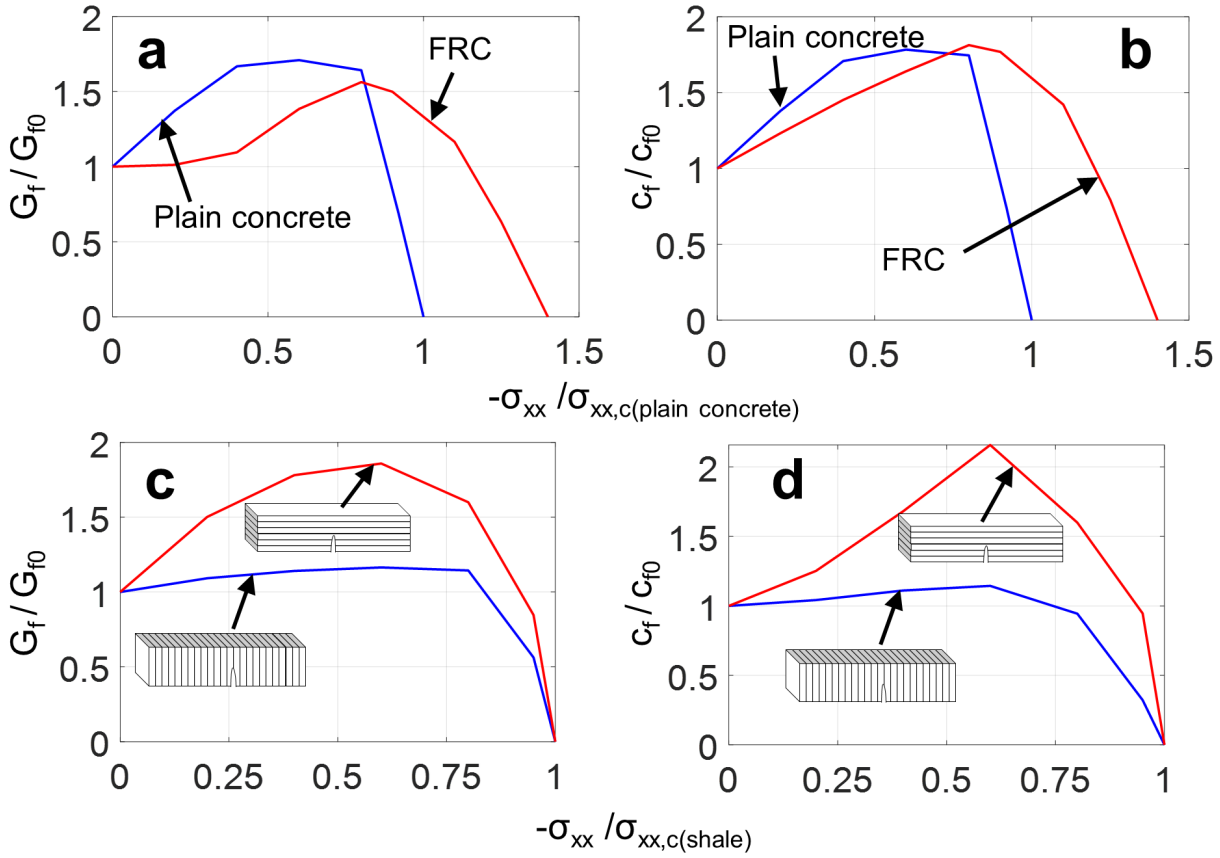

Figure 5.1: (a–b) The variation of G_f and c_f of 3% Dramix-fiber-reinforced concrete as functions of σ_{xx} ; (c–d) The variation of G_f and c_f of shale with bedding plane normal and parallel to the crack as functions of σ_{xx}.

only uses ab-initio data (obtained by the density functional theory code, or DFT) that are useful for large-strain regime [113]. The excellent match between high-resolution images using transmission electron microscope (HR-TEM) of the highly nonlinear zone (crack front and crack tip) enables a direct comparison between two sources of data and enhances the confidence of the potential in predicting the behavior of the studied TMDs in presence of vacancies, reported in the following section.

5.2.2 The emergence of heterogeneous structures due to the presence of vacancies

It can be seen from the near-tip stress mapping and from the load-displacement curve that the behavior of the material is quite brittle, except for a small nonlinear area; see Fig. 5.2. It is the nature of the covalent bonds breakage that abruptly releases the energy from a stretching state and the homogeneity of the material. However, the emergence of vacancies break that symmetry and creates heterogeneity on the structural level. Without these vacancies, a crack parallel stress would not have any effect.

In this section, we used MD simulations, with a Tersoff potential optimized by the framework mentioned above, to examine the behaviors of atoms at the crack tip and at the crack edges in the presence of vacancies. The model consisted of an 80×40 nm rectangular monolayer and a 20-nm long crack, which was loaded along the y direction (see Fig. 5.2a). The boundary conditions were set to be free or a fixed displacement value corresponding to a prescribed strain at the left and right edges and periodic at the top and bottom. To prevent the curling-up of the free edges, repulsive walls were placed parallel to the x-y plane at a distance of 10 Å away from the monolayer. This is consistent with the fact that in a typical in-situ electron microscopy experimental setup, the monolayer specimen is not completely freestanding but restrained by adhesion to the substrate. A fast-loading rate was applied up to a point close to failure and then reduced to avoid rate effects in

bond breakage when the energy stored in the strained monolayer was released abruptly. The atomic positions at the onset of crack propagation were used in a discrete-to-continuum mapping scheme, which was in turn used to compute the critical J-integral. A snapshot of the crack tip and crack edges, on a pristine monolayer when the crack propagated to half of the domain size, is shown in Fig. 5.2b. Along the crack, edges with single Se atoms and distorted hexagonal rings are observed in both experiments and simulations17. We note that these types of edge structures could not be formed by the mere removal of atoms, but only through a stress-assisted dissociating process. The crack tip depicted in Fig. 5.2b also exhibits several features resembling those observed in atomic configurations revealed by HRTEM and DFT, such as rotation of the Se-Mo-Se angular structure and stretching of the bonds at the crack tip17. The agreement between experiments and ab-initio-informed atomistic simulations, in fracture responses of pristine $MoSe_2$ monolayers, enables us to make predictions about the interaction of defects and the dominating cracks depicted in Figs. 5.2c-g. Building on this development, we aimed at understanding the fundamental role of each vacancy type and their density on $MoSe_2$ fracture. However, as presented earlier, due to the low density of two vacancy types, iSe_2 and iMo, these values were raised to be equal to the density of iSe for comparison purposes.

The qualitative and quantitative effects of four vacancy types are summarized in Figs. 5.2c-g. If iSe vacancies are present in the vicinity of a crack tip (Figure 3c and Movie 1), they mildly deflect the crack path but barely change the fracture resistance, as presented in Fig. 5.2f. On the other hand, other types of defects have more impact on the fracture response and associated fracture energy. We note that due to their similar effects on fracture, iMo and iSe_2 were considered together. When vacancies of these types appeared ahead of the crack, they blunt the tip, which locally decreases the stress singularity and triggers an edge-nucleated slip motion in the $\pm 60^\circ$ directions (Fig. 5.2d). This motion is enabled by the shear stress at $\pm 60^\circ$ of the tip and the

presence of another isolated vacancy appearing along the slip plane. The deformation process lowers the associated energy and stress barriers, allowing Se atoms to hop to a nearby location and create a slip plane. At the same time, the decrease in stress singularity increases the energy barrier for the crack to propagate at 0°. As this barrier becomes larger than the one needed for slip, a locally strengthening structure is nucleated. Interestingly, this local structural change traps the propagating crack tip. As a result, the crack must proceed in a different path, which required an increase in driving force and a higher fracture energy. By performing simulations on multiple replicas, we found that the probability of these events is about 20%. This percentage implies that the probability of such an event is relatively low even though the increase of the fracture energy was significant. This leads to a more moderate increase of the average value obtained by simulating several different replicas (see Figs. 5.2f,g).

On the other hand, when Se vacancy lines were present at the crack tip, they deflected the crack towards the direction of the line, resulting in a tortuous kinked crack path (Fig. 5.2e). In some cases, when two vacancy lines intersected, extra free edges were created, leading to a higher dissipated energy. In addition, the crack tortuosity resulted in a more gradual release of energy (see Fig. 5.2f). However, due to the loss of one layer of Se atoms and the brittle nature of covalent bonds, the strength and overall fracture energy decreases when compared to pristine $MoSe_2$ (see Fig. 5.2g). We note that in all cases, the error bars in monolayers with vacancies are larger as we accounted for both errors from various contours and various replicas with randomly generated vacancies. The fracture behavior in the presence of vacancies brought up two contrasting behaviors. In the presence of iMo and iSe_2 vacancies, the crack propagation occurs in the direction opposite to the direction of the vacancies. In other words, vacancies repelled the crack. On the contrary, a Se vacancy lines attracted and guided the crack along their orientations.

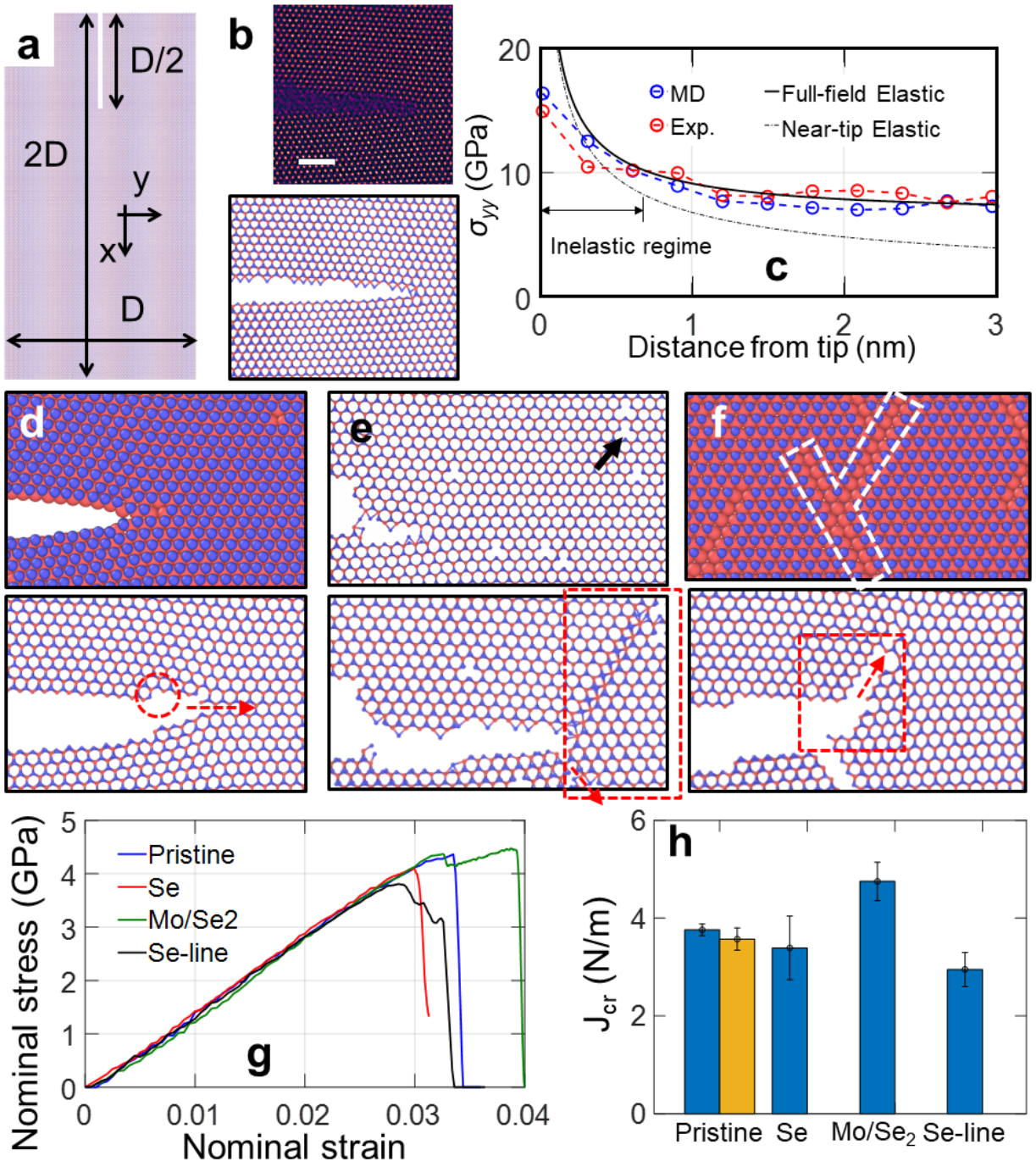

Figure 5.2: (a) Domain sizes used in the uniaxial and fracture tests, D = 40nm; (b) A comparison between HR-TEM and atomically simulated images of the crack tip and crack edges on a pristine monolayer; (c) The stress distribution of σ_{yy} in front of the tip; (d-f) The interaction of the main crack with isolated Se, Mo/Se_2, and Se vacancy lines (red arrows show the propagating direction of the crack); (g) Typical nominal stress-strain curves for pristine and in the presence of these types of vacancies; and (h) The effect of these vacancies on $MoSe_2$ fracture energy (yellow bar indicates the experimental value).

5.2.3 The effect of crack parallel tensile stress

Due to the single-atom thickness of TMDs, compressive normal stress will lead to the buckling of a monolayer. Therefore, only crack-parallel tensile stress is considered here. When such a stress is applied to the structure with iMo vacancy type, the phase transition which depends on the dislocation glide is restricted, i.e., the atoms cannot displace to form the strengthening boundary at the tip. Therefore, instead of being deflected, the cracks continues to grow in the x-direction; see Fig. 5.3. This ultimately leads to a lower fracture energy and diminishes the role of the iMo vacancy. Therefore, biaxial stress state needs to be considered in vacancy engineering problems.

5.3 The implications of the crack-parallel stress in engineering problems

5.3.1 Crack-parallel stresses: where do they matter in practice?

Aside from the cases mentioned in chapter 1, other practical situations may be affected by the crack-parallel stresses.

1. Shear failure of RC beams and slabs, prestressed concrete
2. Longitudinal crack in pressurized aircraft fuselage
3. Crack in casing of solid-fuel rocket
4. Shear crack in aircraft wing, wing box, rudder, stabilizer
5. Fracking, esp. with poromechanical stress transfer to solid
6. Sea ice sheet pushing on a fixed structure
7. Pressure vessel fractures
8. Fracture in arch dam or arch bridge abutments, in footings
9. Crush cans for automobile crashworthiness
10. Cracks caused by projectile impact

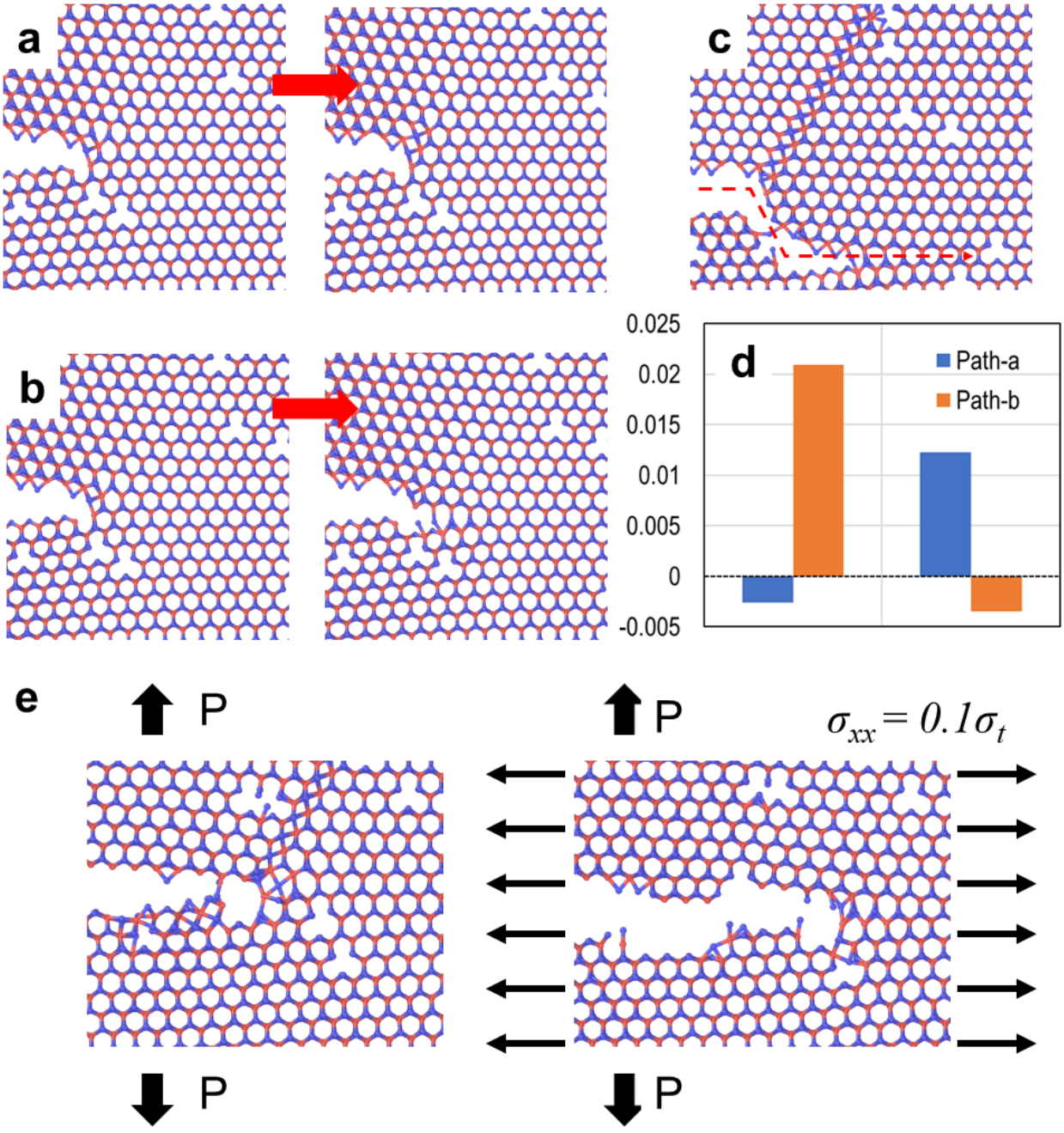

Figure 5.3: (a-b) Two possible atomic changes when the heterogeneous structure arises at the crack front due to the isolated vacancies, leading to the formation of a strengthening phase and ultimately a crack deflection (c). (d) The energy difference between path-a and path-b transitions without (left0 and with (right) a crack-parallel tension $\sigma_{xx} = 0.1\sigma_t$ in which such a stress suppresses the formation of the strengthening phase.

11. Cracks in inflatable shells
12. Most thermal cracks
13. Cracks in geology, in seismic events
14. Pullout fracture of anchors from rock or concrete
15. Fuselage cracks, shear cracks in fiber composite wings, wing box,rudder
16. Shear crack in fiber composite wind turbine leafs;
17. Particle comminution in projectile impact;
18. Many situations in fracture of fatigued plastic-hardening polycrystalline metals; mine openings; bio-materials; , etc.

5.3.2 Gap test as an indicator of a model capability to describe damage and fracture properly

In this section, the ability of a few damage/fracture models to capture the results of the gap test was assessed and presented in Fig. 5.4 (the description of each model was presented in Appendix). Due to differences in accuracy of various numerical models, the size effect method, when applied to different models, yields for the same material different values of fracture energy G_{f0} at $\sigma_{xx} = 0$; see Fig. 5.4a. Therefore, to facilitate comparisons, ratios G_f/G_{f0} are used as the coordinate in the diagram of Fig. 5.4b.

- The crack band model with microplane M7 damage law (**CB-M7**) and a tensorial plasticity-damage law (**CB-Gr**) both follow the trend of gap test, which is an increasing G_f through low to medium σ_{xx} and weakening at high σ_{xx}. Quantitatively, though, the **CB-M7** captures the variation of fracture energy G_f with σ_{xx} better than **CB-Gr** (Fig. 5.4).

- The PD models cannot predict the effect of crack parallel stress on G_f at all. Furthermore, due to their excessive brittleness, the basic peridynamic model (**bPD**) incorrectly shows

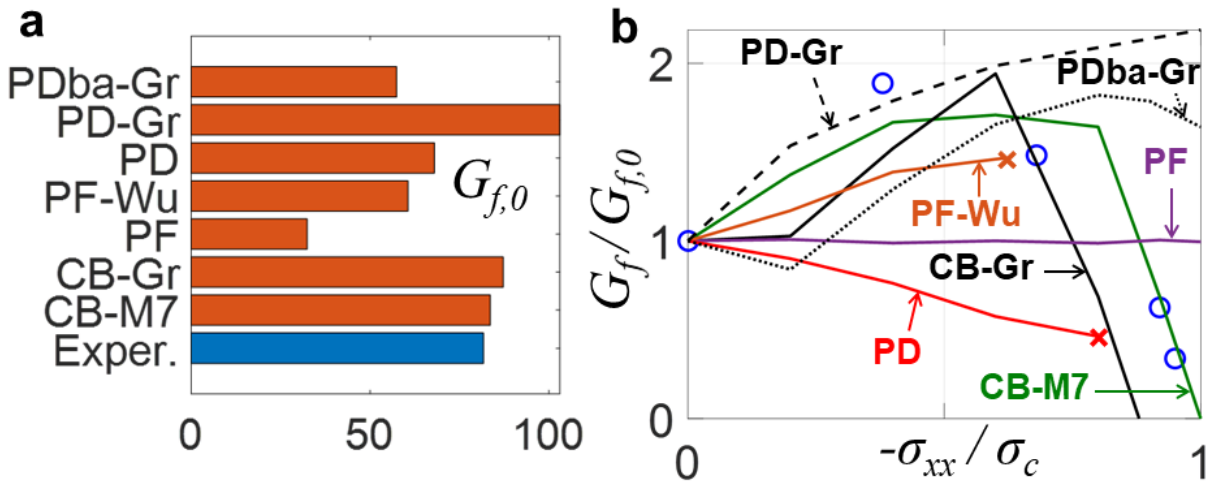

Figure 5.4: a) The deviations from the experimental fracture energy of CB, PF, and PD models. b) Gap test results showing the relative change of measured concrete fracture energy G_f versus crack-parallel compression σ_{xx}, normalized by uniaxial compression strength σ_c, and comparisons to CB, PF, and PD models.

a monotonically decreasing G_f, explained by sudden bond breakages upon reaching their compression strength limit). This model predicts a premature failure (indicated by the x point) much before reaching the material compression strength σ_c. Among the PD models, the bond-associated peridynamic model (**PDba-Gr**) shows the least error and captures at least the increasing trend of G_f as σ_{xx} increases.

- As σ_{xx} increases, the basic phase-field model (**bPF**) shows incorrectly no change in G_f, which confirms it is a LEFM model. The formulation of an enhanced phase-field model (**PF-Wu**), however, generates an FPZ with non-zero width that can interact with σ_{xx}. Yet this model gives an insufficient monotonic growth of G_f which terminates prematurely (indicated by another x point) because, in using the size effect method, the gap test fails by compression before the gaps close. This is similar to what happens in the compression test of 2D confined specimens in which the biaxial stress state actually weakens the calculated response.

CHAPTER 6
CONCLUSION AND FUTURE DIRECTION

6.1 For quasibrittle materials

1. Moderate crack-parallel compressive stress, in-plane or out-of-plane, drastically increases, even doubles, the Mode I fracture energy G_f (or fracture toughness K_{Ic}) of concrete, and probably also shale and various rocks, coarse-grained ceramics and sea ice. This can be explained by increase of hydrostatic pressure raising friction on inclined planes.
2. High crack-parallel compressive stress close to the compression strength limit drastically decreases G_f and eventually reduces it to zero. This can be explained by frictional slip on inclined planes and splitting microcracks, causing lateral dilation.
3. The cohesive crack model (CCM), as a line crack model with a scalar relation between crack-bridging stress and relative displacement of crack faces, cannot capture these phenomena, since the crack-parallel strains are not the thermodynamic variables in this model. So σ_{xx} and σ_{zz} must be used as parameters which, however, appears to be only a crude approximation which cannot capture the effect of the triaxial stress and strain history. The same objection also applies to the recent cohesive crack model that is enriched with crack-parallel strain by shrinking a crack band into a line [115] .
4. To capture the experimentally evidenced effect of crack-parallel compression in general, either a microscale descriptive or a tensorial constitutive model for softening damage must be used. This is effectively done with the crack band model coupled with the microplane damage constitutive law. This law can mimic the effects of inelastic frictional slips and microcracks separately on planes of different orientations. The damage laws in the phase-

field models restricted to only a single damage parameter do not appear to be realistic.

5. Linear elastic fracture mechanics cannot capture the effect of crack-parallel compression. As a line crack model, CCM can neither. Nor can the computational models based on LEFM or CCM.
6. An effective method for fracture testing with crack-parallel compression is the gap test, in which the compression is generated by plastic pads capable of perfectly plastic yielding, and the supports are installed with a gap that closes only after the pads begin yielding.
7. The results are of particular interest for: a) the shear failure of reinforced concrete beams and punching of slabs; b) fracture of prestressed concrete, c) for hydraulic fracturing of shale, at which the overburden and tectonic stress introduce significant crack-parallel compression; c) fiber composites, where buckling of embedded fibers reduces compression strength; d) propagation of the front of slip on earthquake fault, subjected to enormous crack-parallel tectonic and overburden stresses; e) splitting fracture of sea ice plates pushing against fixed objects; f) cyclic and static fatigue crack growth under crack-parallel in-plane and out-of-plane stresses; h) high biaxial tensile stresses in composite aircraft fuselage.
8. The Mohr circles for various levels of crack parallel stress in shale do not have an envelope. Therefore, the use of Mohr-Coulomb failure criterion for shale or other quasibrittle materials is unwarranted.

6.2 For ductile materials

1. In contrast to quasibrittle fracture, the analysis of ductile fracture of plastic-hardening materials is complicated by the existence of a millimeter-scale yielding zone separating the unloading elastic zone of structure from the micrometer-scale damage zone of fracture process.

2. The effective size of the yielding zone is properly determined by using the principal of virtual work to enforce equilibrium in the zone of transition between the plastic hardening zone and elastic zone. Alternatively, the same effective size is obtained by minimizing the squared difference of these fields integrated over this zone. This furnishes the yielding zone size as a function of the crack-parallel T-stress.
3. In addition to the energy released from the structure, further energy is released from the unloaded band of material trailing the advancing yielding zone. In addition to the energy dissipated at fracture front, further energy is dissipated by irreversible unloading of the material behind the advancing yielding zone. The energy flux described by the J-integral delivers energy through the yielding zone to the fracture process zone at crack front, but neither releases nor dissipates any energy within the yielding zone.
4. Balance of energy release and energy dissipation leads to an approximate size effect law for plastic-hardening fracture matching the asymptotic behaviors on both sides of the size scale. The law is of the same form as the classical size effect law (of Type 2) for quasibrittle materials such a concrete. However, the coefficients in this law are related to the material properties in a different way.
5. Based on the size effect law derived, the identification of fracture energy and effective size of the yielding zone for specimens significantly larger than the yielding zone is reducible to linear regression.
6. When the test data range reaches into specimens so small that the development of the crack tip yielding zone is restricted by the boundaries, a modification of the size effect law is required. Linear regression is then impossible but identification of fracture properties is still possible.
7. The derived size effect law is verified by two series of tests of scaled notched three-point

bend specimens of aluminum.

8. The size effect method is a relatively simple method to estimate the fracture energy of plastic-hardening materials. It is simpler than the elaborate procedure specified in ASTM-E1820 [90]. However, broader experimental verification is appropriate and some details might still need to be worked out.
9. Extension of the gap tests of aluminum to three different levels of the crack-parallel compressive stress σ_{xx} provides a clear evidence of the effect of σ_{xx} on the size effect, which is found to be strong.
10. Regression analysis of the gap tests of different sizes for the same σ_{xx} level yields unambiguous evidence of the σ_{xx} effect on the fracture energy G_f and effective radius of the yielding zone r_p.
11. Increasing σ_{xx} from 0 to $0.4f_y$ approximately causes G_f to double and r_p to tripple. Although no tests were made at $|\sigma_{xx}| > 0.4f_y$, the extension of the curve of G_f versus σ_{xx} is expected not to tend to 0 at $\sigma_{xx} \to -f_y$ because in contrast to concrete, aluminum under compression yielding in x-direction still has a significant tensile yield strength in the y-direction.
12. The results of the gap test of aluminum are rather systematic, with low scatter. This makes the evidence clear.
13. The slope of $-1/2$ in the log-log size effect plot is an indicator of small-scale yielding and applicability of linear elastic fracture mechanics in metals. The present specimen sizes are not large enough to approach this asymptotic slope closely. One might see it as a disadvantage but it is actually an advantage because the material characteristic length r_p can be identified only by testing in the transitional size range between the small-size and large-size asymptotes.
14. Unlike quasibrittle material such as concrete, the size effect curves of nominal strength of geometrically similar notched specimens under various levels of crack parallel stress cross

each other and produces at the small size asymptotic limit a reverse trend, such that the small-size asymptotic strength for a compression magnitude $|\sigma_{xx}|$) occurs at smaller σ_N.

15. To reproduce the present experiments mathematically, a fracture process zone of correct finite width, described by a realistic tensorial damage constitutive model, must be considered. The finite element crack band model can do that.

6.3 Opportunities for future research

Aside from the studied materials, this thesis initiates multiple collaborations with Dr. Hubler at University of Colorado-Boulder, Dr. Salviato at University of Washington-Seattle and Dr. Czabaj at University of Utah to investigate the effect of crack-parallel stresses on fiber-reinforced concrete and carbon-fiber composites with different weaving and laminate designs. As mentioned above, the results of these tests have broad implications on the safety of the structures made of these materials if their service conditions involve being frequently subjected to complex stress state.

Despite the speculation and the estimation of the changes in size of FPZ with different σ_{xx}, an experimental technique is still needed to visualize such changes. This open opportunities for the use of X-Ray and Micro Computed Tomography (μCT) to observe the microstructural change at the crack tip. On the other hand, discrete particle methods such as LDPM [11], [12] can also provide more insights into these mechanisms and the entire fracture process.

The FPZ with finite width begs the question of how the permeability of a hydraulic crack changes when it propagates through the regions with different crack parallel stress levels. Some of the microcracks may be suppressed, indicating a reduced permeability, while their dilation enhances the fluid flow. In a highly permeable reservoir, leakoff water may diffuse from the crack into the matrix and alter the stress state at the tip. All of these questions require further research.

REFERENCES

[1] C. E. Inglis, "Stresses in a plate due to the presence of cracks and sharp corners," *Trans Inst Naval Archit*, vol. 55, pp. 219–241, 1913.

[2] A. Griffith, "The phenomena of rupture and flow in solid, philosophical translation," in *Royal Soc of London, Series A*, vol. 221, 1921.

[3] C. Kesler, D. Naus, and J. Lott, "Fracture mechanics-its applicability to concrete," in *Proceedings of the Society of Materials Science Conference on the Mechanical Behavior of Materials.*, 1972.

[4] J. Rice and G. F. Rosengren, "Plane strain deformation near a crack tip in a power-law hardening material," *Journal of the Mechanics and Physics of Solids*, vol. 16, no. 1, pp. 1–12, 1968.

[5] J. Hutchinson, "Singular behaviour at the end of a tensile crack in a hardening material," *J. Mech. Phys. Solids.*, vol. 16, pp. 13–31, 1968.

[6] G. Barenblatt, "Equilibrium cracks formed on a brittle fracture," *Dokl. Ak. N.*, vol. 127, pp. 47–50, 1959.

[7] N. Moës, J. Dolbow, and T. Belytschko, "A finite element method for crack growth without remeshing," *International journal for numerical methods in engineering*, vol. 46, no. 1, pp. 131–150, 1999.

[8] Z. P. Bažant and B. H. Oh, "Crack band theory for fracture of concrete," *Matériaux et construction*, vol. 16, no. 3, pp. 155–177, 1983.

[9] Z. P. Bažant and M. Jirásek, "Nonlocal integral formulations of plasticity and damage: Survey of progress," *J. Eng. Mech.*, vol. 128, pp. 1119–1149, 2002.

[10] G. Cusatis, Z. Bažant, and L. Cedolin, "Confinement-shear lattice model for concrete damage in tension and compression: Ii. computation and validation," *Journal of Engineering Mechanics - ASCE*, vol. 129, no. 12, pp. 1449–1458, Dec. 2003.

[11] G. Cusatis, D. Pelessone, and A. Mencarelli, "Lattice discrete particle model (ldpm) for failure behavior of concrete. i: Theory," *Cem. Concr. Compos.*, vol. 33, pp. 881–890, 2011.

[12] G. Cusatis, A. Mencarelli, D. Pelessone, and J. Baylot, "Lattice discrete particle model (ldpm) for failure behavior of concrete. ii: Calibration and validation," *Cem. Concr. Compos.*, vol. 33, pp. 891–905, 2011.

[13] F. C. Caner and Z. P. Bažant, "Microplane model m7 for plain concrete. i: Formulation," *Journal of Engineering Mechanics*, vol. 139, no. 12, pp. 1714–1723, 2013.

[14] Z. P. Bažant and J. Planas, "Fracture and size effect in concrete and other quasibrittle materials," 1998.

[15] Z. P. Bažant, *Scaling of structural strength*. CRC Press, 2002.

[16] Z. P. Bažant and Q. Yu, "Designing against size effect on shear strength of reinforced concrete beams without stirrups: Ii. verification and calibration," *J. Struct. Eng.*, vol. 131, pp. 1886–1897, 2005.

[17] Q. Yu, J.-L. Le, M. H. Hubler, R. Wendner, G. Cusatis, and Z. P. Bažant, "Comparison of main models for size effect on shear strength of reinforced and prestressed concrete beams," *Struct. Concr.*, vol. 17, pp. 778–789, 2016.

[18] A. Dönmez and Z. P. Bažant, "Size effect on punching strength of reinforced concrete slabs with and without shear reinforcement," *ACI Struct. J.*, vol. 114, p. 875, 2017.

[19] M. Alnaggar, D. Pelessone, and G. Cusatis, "Lattice discrete particle modeling of reinforced concrete flexural behavior," *J. Struct. Eng.*, vol. 145, p. 04 018 231, 2019.

[20] E. Lale, R. Rezakhani, M. Alnaggar, and G. Cusatis, "Homogenization coarse graining (hcg) of the lattice discrete particle model (LDPM) for the analysis of reinforced concrete structures," *Eng. Fract. Mech.*, vol. 197, pp. 259–277, 2018.

[21] Z. P. Bažant, J.-L. Le, and M. Salviato, *Quasibrittle Fracture Mechanics and Size Effect: A First Course*. Oxford University Press, 2021.

[22] E. Tschegg, M. Elser, and S. Stanzl-Tschegg, "Biaxial fracture tests on concrete—development and experience," *Cem. Concr. Compos.*, vol. 17, pp. 57–75, 1995.

[23] Z. P. Bažant, P. A. Pfeiffer, *et al.*, "Determination of fracture energy from size effect and brittleness number," *ACI Materials Journal*, vol. 84, no. 6, pp. 463–480, 1987.

[24] G. Cusatis and E. A. Schauffert, "Cohesive crack analysis of size effect," *Eng. Fract. Mech*, vol. 76, pp. 2163–2173, 2009.

[25] Z. P. Bažant and Q. Yu, "Size-effect testing of cohesive fracture parameters and nonuniqueness of work-of-fracture method," *Journal of engineering mechanics*, vol. 137, no. 8, pp. 580–588, 2011.

[26] C. G. Hoover and Z. P. Bažant, "Cohesive crack, size effect, crack band and work-of-fracture models compared to comprehensive concrete fracture tests," *Int. J. Fract.*, vol. 187, pp. 133–143, 2014.

[27] Z. P. Bažant and M. T. Kazemi, "Size effect in fracture of ceramics and its use to determine fracture energy and effective process zone length," *Journal of the American Ceramic Society*, vol. 73, no. 7, pp. 1841–1853, 1990.

[28] S. P. Shah, "Rilem recommendation tc89-fmt: Size-effect method for determining fracture energy and process zone size of concrete," *Materials and Structures*, vol. 23, no. 6, p. 461, 1990.

[29] L. Cedolin and G. Cusatis, "Identification of concrete fracture parameters through size effect experiments," *Cement and Concrete Composites*, vol. 30, no. 9, pp. 788–797, 2008.

[30] N. O'dowd and C. F. Shih, "Family of crack-tip fields characterized by a triaxiality parameter—i. structure of fields," *Journal of the Mechanics and Physics of Solids*, vol. 39, no. 8, pp. 989–1015, 1991.

[31] N. P. O'Dowd and C. F. Shih, "Family of crack-tip fields characterized by a triaxiality parameter—ii. fracture applications," *Journal of the Mechanics and Physics of Solids*, vol. 40, no. 5, pp. 939–963, 1992.

[32] C. Betegón and J. W. Hancock, "Two-parameter characterization of elastic-plastic crack-tip fields," *Journal of applied mechanics*, vol. 58, no. 1, pp. 104–110, 1991.

[33] V. Tvergaard and J. W. Hutchinson, "The relation between crack growth resistance and fracture process parameters in elastic-plastic solids," *J. Mech. Phys. Solids.*, vol. 40, no. 6, pp. 1377–1397, 1992.

[34] L. Xia, T. Wang, and C. Shih, "Higher-order analysis of crack tip fields in elastic power-law hardening materials," *Journal of the mechanics and physics of solids.*, vol. 41, no. 4, pp. 665–687, 1993.

[35] X. Gao, C. Shih, V. Tvergaard, and A. Needleman, "Constraint effects on the ductile-brittle transition in small scale yielding," *Journal of the mechanics and physics of solids.*, vol. 44, no. 8, pp. 1255–1282, 1996.

[36] E. O. Hall, "The deformation and ageing of mild steel: Iii discussion of results," *Proceedings of the Physical Society. Section B*, vol. 64, no. 9, p. 747, 1951.

[37] A. H. Cottrell, *Dislocations and Plastic Flow in Crystals*. Oxford University Press, 1958.

[38] J. R. Greer and J. T. M. De Hosson, "Plasticity in small-sized metallic systems: Intrinsic versus extrinsic size effect," *Progress in Materials Science*, vol. 56, no. 6, pp. 654–724, 2011.

[39] D. Kiener, W. Grosinger, G. Dehm, and R. Pippan, "A further step towards an understanding of size-dependent crystal plasticity: In situ tension experiments of miniaturized single-crystal copper samples," *Acta Materialia*, vol. 56, no. 3, pp. 580–592, 2008.

[40] M. C. Shaw, "The size effect in metal cutting," *Sadhana*, vol. 28, no. 5, pp. 875–896, 2003.

[41] P. Walsh, "Fracture of plain concrete," *Indian Concrete Journal*, vol. 46, no. 11, 1972.

[42] H. Nguyen, M. Pathirage, M. Rezaei, M. Issa, G. Cusatis, and Z. P. Bažant, "New perspective of fracture mechanics inspired by novel test with crack-parallel compression," *Proceedings of the National Academy of Sciences,*, vol. In Press, 2020.

[43] Z. P. Bažant, "Size effect in blunt fracture: Concrete, rock, metal," *J. Eng. Mech.*, vol. 110, pp. 518–535, 1984.

[44] Z. Bažant, "Scaling of quasibrittle fracture: Asymptotic analysis," *Int. J. Fract.*, vol. 83, p. 19, 1997.

[45] Z. P. Bazant and J.-L. Le, *Probabilistic mechanics of quasibrittle structures: strength, lifetime, and size effect*. Cambridge University Press, 2017.

[46] A. C. 446, "Fracture mechanics of concrete: Concepts, models and determination of material properties," vol. 91, 1992.

[47] F. R. Shanley, "Inelastic column theory," *Journal of the aeronautical sciences*, vol. 14, no. 5, pp. 261–268, 1947.

[48] Z. P. Bažant and L. Cedolin, "Why direct tension test specimens break flexing to the side," *Journal of Structural Engineering*, vol. 119, no. 4, pp. 1101–1113, 1993.

[49] L. Cedolin *et al.*, *Stability of structures: elastic, inelastic, fracture and damage theories*. World Scientific, 2010.

[50] Z. P. Bažant and A. Beghini, "Stability and finite strain of homogenized structures soft in shear: Sandwich or fiber composites, and layered bodies," *International journal of solids and structures*, vol. 43, no. 6, pp. 1571–1593, 2006.

[51] T. Fett, *Stress intensity factors-t-stresses-weight functions*. 2008.

[52] Z. Bažant, R. Gettu, and M. Kazemi, "Identification of nonlinear fracture properties from size effect tests and structural analysis based on geometry-dependent r-curves," in *International journal of rock mechanics and mining sciences & geomechanics abstracts*, Elsevier, vol. 28, 1991, pp. 43–51.

[53] F. C. Caner and Z. P. Bažant, "Microplane model m7 for plain concrete. ii: Calibration and verification," *Journal of Engineering Mechanics*, vol. 139, no. 12, pp. 1724–1735, 2013.

[54] J. Nakayama, "Direct measurement of fracture energies of brittle heterogeneous materials," *J. Am. Ceram. Soc.*, vol. 48, pp. 583–587, 1965.

[55] H. G. Tattersall and G. Tappin, "The work of fracture and its measurement in metals, ceramics and other materials," *J. Mater. Sci.*, vol. 1, pp. 296–301, 1966.

[56] A. Hillerborg, M. Modéer, and P.-E. Petersson, "Analysis of crack formation and crack growth in concrete by means of fracture mechanics and finite elements," *Cem. Concr. Res.*, vol. 6, pp. 773–781, 1976.

[57] Z. P. Bažant and Y. Xiang, "Size effect in compression fracture: Splitting crack band propagation," *Journal of engineering mechanics*, vol. 123, no. 2, pp. 162–172, 1997.

[58] Z. P. Bažant, "Microplane model for strain-controlled inelastic behaviour," *Mechanics of Engineering Materials*, pp. 45–59, 1984.

[59] W. T. Koiter, "Stress-strain relations, uniqueness and variational theorems for elastic-plastic materials with a singular yield surface," *Quarterly of applied mathematics*, vol. 11, no. 3, pp. 350–354, 1953.

[60] W. Koiter, *General Theorems for Elastic-plastic Solids*. North-Holland, 1960.

[61] A. Phillips, J.-L. Tang, and M. Ricciuti, "Some new observations on yield surfaces," *Acta Mechanica*, vol. 20, no. 1, pp. 23–39, 1974.

[62] Z. P. Bažant, "Endochronic inelasticity and incremental plasticity," *International Journal of Solids and Structures*, vol. 14, no. 9, pp. 691–714, 1978.

[63] K. Kirane and Z. P. Bažant, "Microplane damage model for fatigue of quasibrittle materials: Sub-critical crack growth, lifetime and residual strength," *International Journal of Fatigue*, vol. 70, pp. 93–105, 2015.

[64] J. R. Rice, "A path independent integral and the approximate analysis of strain concentration by notches and cracks," *ASME Journal of Applied Mechanics*, vol. 35, no. 2, pp. 379–386, 1968.

[65] F. Z. Li, C. F. Shih, and A. Needleman, "A comparison of methods for calculating energy release rates," *Engineering fracture mechanics*, vol. 21, no. 2, pp. 405–421, 1985.

[66] P. Grassl, D. Xenos, U. Nyström, R. Rempling, and K. Gylltoft, "Cdpm2: A damage-plasticity approach to modelling the failure of concrete," *International Journal of Solids and Structures*, vol. 50, no. 24, pp. 3805–3816, 2013.

[67] D. C. Drucker and W. Prager, "Soil mechanics and plastic analysis or limit design," *Quarterly of applied mathematics*, vol. 10, no. 2, pp. 157–165, 1952.

[68] A. Nadai, *Theory of flow and fracture of solids, v1*. McGraw-Hill, 1950.

[69] S. Rahimi-Aghdam, V.-T. Chau, H. Lee, *et al.*, "Branching of hydraulic cracks enabling permeability of gas or oil shale with closed natural fractures," *Proceedings of the National Academy of Sciences*, vol. 116, no. 5, pp. 1532–1537, 2019.

[70] J. Mazars, "A model of a unilateral elastic damageable material and its application to concrete," *Fracture toughness and fracture energy of concrete*, pp. 61–71, 1986.

[71] G. Pijaudier-Cabot and Z. P. Bažant, "Nonlocal damage theory," *Journal of engineering mechanics*, vol. 113, no. 10, pp. 1512–1533, 1987.

[72] Z. P. Bažant, W. Luo, V. T. Chau, and M. A. Bessa, "Wave dispersion and basic concepts of peridynamics compared to classical nonlocal damage models," *Journal of Applied Mechanics*, vol. 83, no. 11, 2016.

[73] J. W. Hutchinson, "Plastic stress and strain fields at a crack tip," *Journal of the Mechanics and Physics of Solids*, vol. 16, no. 5, pp. 337–342, 1968.

[74] T. L. Anderson, *Fracture Mechanics: Fundamentals and Applications*. Boca Raton, FL: CRC Press, 1991.

[75] M. F. Kanninen and C. H. Popelar, *Advanced Fracture Mechanics*, ser. Oxford engineering science series. New York: Oxford University Press, 1985.

[76] H. T. Nguyen, M. Pathirage, G. Cusatis, and Z. P. Bažant, "Gap test of crack-parallel stress effect on quasibrittle fracture and its consequences," *Journal of Applied Mechanics*, vol. 87, no. 7, p. 071 012, 2020.

[77] Z. P. Bažant and E.-P. Chen, "Scaling of structural failure," *Applied Mechanics Reviews ASME*, vol. 50, no. 10, pp. 593–627, 1997.

[78] W. Ramberg and W. R. Osgood, "Description of stress-strain curves by three parameters," *Technical Note 902, NACA, Washington, D.C.*, 1943.

[79] J. W. Hutchinson and P. C. Paris, "Stability analysis of j-controlled crack growth," in *Elastic-plastic fracture*, ASTM International, 1979.

[80] J. R. Rice, "Mathematical analysis in the mechanics of fracture," *Fracture: an advanced treatise*, vol. 2, pp. 191–311, 1968.

[81] G. Nikishkov, "J-a fracture concept based on the three-term elastic-plastic asymptotic expansion of the near-crack tip stress field," *Fracture: a topical encyclopedia of current knowledge*, pp. 557–574, 1998.

[82] B. Revil-Baudard, O. Cazacu, and N. Chandola, "Effect of the yield stresses in uniaxial tension and pure shear on the size of the plastic zone near a crack," *International Journal of Plasticity*, vol. 102, pp. 101–117, 2018.

[83] G. Xin, W. Hangong, K. Xingwu, and J. Liangzhou, "Analytic solutions to crack tip plastic zone under various loading conditions," *European Journal of Mechanics-A/Solids*, vol. 29, no. 4, pp. 738–745, 2010.

[84] N. Levy, P. Marcal, W. J. Ostergren, and J. R. Rice, "Small scale yielding near a crack in plane strain: A finite element analysis," *International Journal of Fracture Mechanics*, vol. 7, no. 2, pp. 143–156, 1971.

[85] Z. P. Bažant, S.-G. Lee, and P. A. Pfeiffer, "Size effect tests and fracture characteristics of aluminum," *Engineering Fracture Mechanics*, vol. 26, no. 1, pp. 45–57, 1987.

[86] Z. P. Bažant and M. T. Kazemi, "Size effect on diagonal shear failure of beams without stirrups," *ACI Structural journal*, vol. 88, no. 3, pp. 268–276, 1991.

[87] G. Herrmann and H. Sosa, "On bars with cracks," *Engineering Fracture Mechanics*, vol. 24, no. 6, pp. 889–894, 1986.

[88] R. Kienzler and G. Herrmann, "An elementary theory of defective beams," *Acta Mechanica*, vol. 62, no. 1-4, pp. 37–46, 1986.

[89] R. Narasimhan and A. J. Rosakis, "Three-dimensional effects near a crack tip in a ductile three-point bend specimen: Part i—a numerical investigation," *Journal of applied mechanics*, vol. 57, no. 3, pp. 607–617, 1990.

[90] A. S. for Testing and Materials, "Standard test method for measurement of fracture toughness," ASTM International, West Conshohocken, PA, Standard, 2020.

[91] A. Srivastava, L. Ponson, S. Osovski, E. Bouchaud, V. Tvergaard, and A. Needleman, "Effect of inclusion density on ductile fracture toughness and roughness," *Journal of the Mechanics and Physics of Solids*, vol. 63, pp. 62–79, 2014.

[92] K. K. Mathur, A. Needleman, and V. Tvergaard, "Three dimensional analysis of dynamic ductile crack growth in a thin plate," *Journal of the Mechanics and Physics of Solids*, vol. 44, no. 3, pp. 439–464, 1996.

[93] Z. P. Bažant, "Scaling theory for quasibrittle structural failure," *Proceedings of the National Academy of Sciences*, vol. 101, no. 37, pp. 13 400–13 407, 2004.

[94] G. Barenblatt, *Similarity, Self-similarity, and Intermediate Asymptotics*. New York: Consultants Bureau, 1979.

[95] Y. Bai and T. Wierzbicki, "Application of extended mohr–coulomb criterion to ductile fracture," *International Journal of Fracture*, vol. 161, no. 1, pp. 1–20, 2010.

[96] ——, "A new model of metal plasticity and fracture with pressure and lode dependence," *International journal of plasticity*, vol. 24, no. 6, pp. 1071–1096, 2008.

[97] L. Xue, "Ductile fracture modeling: Theory, experimental investigation and numerical verification," Ph.D. dissertation, Massachusetts institute of technology, 2007.

[98] I. Barsoum, "Ductile failure and rupture mechanisms in combined tension and shear," Ph.D. dissertation, Hållfasthetslära, 2006.

[99] M. Wilkins, R. Streit, and J. Reaugh, "Cumulative-strain-damage model of ductile fracture: Simulation and prediction of engineering fracture tests," Lawrence Livermore National Lab., CA (USA), Tech. Rep., 1980.

[100] J. R. Rice and D. M. Tracey, "On the ductile enlargement of voids in triaxial stress fields," *Journal of the Mechanics and Physics of Solids*, vol. 17, no. 3, pp. 201–217, 1969.

[101] J. Hancock and A. Mackenzie, "On the mechanisms of ductile failure in high-strength steels subjected to multi-axial stress-states," *Journal of the Mechanics and Physics of Solids*, vol. 24, no. 2-3, pp. 147–160, 1976.

[102] G. R. Johnson and W. H. Cook, "Fracture characteristics of three metals subjected to various strains, strain rates, temperatures and pressures," *Engineering fracture mechanics*, vol. 21, no. 1, pp. 31–48, 1985.

[103] M. R. Shankar, S. Chandrasekar, W. D. Compton, and A. H. King, "Characteristics of aluminum 6061-t6 deformed to large plastic strains by machining," *Materials Science and Engineering: A*, vol. 410, pp. 364–368, 2005.

[104] Z. Zhang, J. Wang, Q. Zhang, S. Zhang, Q. Shi, and H. Qi, "Research on grain refinement mechanism of 6061 aluminum alloy processed by combined spd methods of ecap and mac," *Materials*, vol. 11, no. 7, p. 1246, 2018.

[105] M. L. Williams, "Stress singularities resulting from various boundary conditions in angular corners of plates in extension," *Journal of applied mechanics*, vol. 19, no. 4, pp. 526–528, 1952.

[106] C. F. Shih and J. W. Hutchinson, "Fully plastic solutions and large scale yielding estimates for plane stress crack problems," *Journal of Engineering Materials and Technology*, vol. 98, pp. 289–295, 1976.

[107] N. Petch, "The cleavage strength of polycrystals," *Journal of the iron and steel institute*, vol. 174, pp. 25–28, 1953.

[108] H. T. Nguyen, A. A. Dönmez, and Z. P. Bažant, "Structural strength scaling law for fracture of plastic-hardening metals and testing of fracture properties," *Extreme Mechanics Letters*, vol. 43, p. 101 141, 2021.

[109] Z. P. Bažant and L. Cedolin, "Blunt crack band propagation in finite element analysis," *Journal of the Engineering Mechanics Division*, vol. 105, no. 2, pp. 297–315, 1979.

[110] Z. P. Bažant, "Scaling laws in mechanics of failure," *Journal of Engineering Mechanics*, vol. 119, no. 9, pp. 1828–1844, 1993.

[111] F. C. Caner, Z. P. Bažant, and R. Wendner, "Microplane model m7f for fiber reinforced concrete," *Engineering fracture mechanics*, vol. 105, pp. 41–57, 2013.

[112] C. Li, F. C. Caner, V. T. Chau, and Z. P. Bažant, "Spherocylindrical microplane constitutive model for shale and other anisotropic rocks," *Journal of the Mechanics and Physics of Solids*, vol. 103, pp. 155–178, 2017.

[113] X. Zhang, H. Nguyen, J. T. Paci, S. K. Sankaranarayanan, J. L. Mendoza-Cortes, and H. D. Espinosa, "Multi-objective parametrization of interatomic potentials for large deformation pathways and fracture of two-dimensional materials," *npj Computational Materials*, vol. 7, no. 1, pp. 1–11, 2021.

[114] C. Igel, N. Hansen, and S. Roth, "Covariance matrix adaptation for multi-objective optimization," *Evolutionary computation*, vol. 15, no. 1, pp. 1–28, 2007.

[115] J. J. Remmers, R. De Borst, C. V. Verhoosel, and A. Needleman, "The cohesive band model: A cohesive surface formulation with stress triaxiality," *Int. J. Fract.*, vol. 181, pp. 177–188, 2013.

[116] N. Toshio and D. M. Parks, "Determination of elastic t-stress along three-dimensional crack fronts using an interaction integral," *International journal of solids and structures*, vol. 29, no. 13, pp. 1597–1611, 1992.

[117] K. Lu and T. Meshii, "Three-dimensional t-stresses for three-point-bend specimens with large thickness variation," *Engineering Fracture Mechanics*, vol. 116, pp. 197–203, 2014.

[118] C. Hoover, Z. Bažant, R. Wendner, *et al.*, "Experimental investigation of transitional size effect and crack length effect in concrete fracture," in *Life-Cycle and sustainability of civil infrastructure systems: Proceedings of the 3rd International Symposium on Life-Cycle Civil Engineering (IALCCE), October*, 2012, pp. 3–6.

[119] C. G. Hoover, Z. P. Bažant, J. Vorel, R. Wendner, and M. H. Hubler, "Comprehensive concrete fracture tests: Description and results," *Engineering fracture mechanics*, vol. 114, pp. 92–103, 2013.

[120] N. Provatas and K. Elder, *Phase-field methods in materials science and engineering*. John Wiley & Sons, 2011.

[121] G. A. Francfort and J.-J. Marigo, "Revisiting brittle fracture as an energy minimization problem," *Journal of the Mechanics and Physics of Solids*, vol. 46, no. 8, pp. 1319–1342, 1998.

[122] J.-Y. Wu, Y. Huang, H. Zhou, and V. P. Nguyen, "Three-dimensional phase-field modeling of mode i+ ii/iii failure in solids," *Computer Methods in Applied Mechanics and Engineering*, vol. 373, p. 113 537, 2021.

[123] K. Pham, K. Ravi-Chandar, and C. Landis, "Experimental validation of a phase-field model for fracture," *International Journal of Fracture*, vol. 205, no. 1, pp. 83–101, 2017.

[124] S. Narayan and L. Anand, "A gradient-damage theory for fracture of quasi-brittle materials," *Journal of the Mechanics and Physics of Solids*, vol. 129, pp. 119–146, 2019.

[125] Z. P. Bažant and M. R. Tabbara, "Bifurcation and stability of structures with interacting propagating cracks," *International journal of fracture*, vol. 53, no. 3, pp. 273–289, 1992.

[126] J.-Y. Wu, "A unified phase-field theory for the mechanics of damage and quasi-brittle failure," *Journal of the Mechanics and Physics of Solids*, vol. 103, pp. 72–99, 2017.

[127] S. A. Silling, "Reformulation of elasticity theory for discontinuities and long-range forces," *Journal of the Mechanics and Physics of Solids*, vol. 48, no. 1, pp. 175–209, 2000.

[128] S. A. Silling and E. Askari, "A meshfree method based on the peridynamic model of solid mechanics," *Computers & structures*, vol. 83, no. 17-18, pp. 1526–1535, 2005.

[129] S. A. Silling, M. Epton, O. Weckner, J. Xu, and E. Askari, "Peridynamic states and constitutive modeling," *Journal of elasticity*, vol. 88, no. 2, pp. 151–184, 2007.

[130] E. Madenci and E. Oterkus, *Peridynamic Theory and Its Applications*, ser. SpringerLink : Bücher. Springer New York, 2013, ISBN: 9781461484653.

[131] N. J. Burt and J. W. Dougill, "Progressive failure in a model heterogeneous medium," *Journal of the Engineering Mechanics Division*, vol. 103, no. 3, pp. 365–376, 1977.

[132] K. Kirane, K. D. Singh, and Z. P. Bažant, "Size effect in torsional strength of plain and reinforced concrete.," *ACI Structural Journal*, vol. 113, no. 6, 2016.

[133] M. Hobbs, T. Dodwell, G. Hattori, and J. Orr, "An examination of the size effect in quasi-brittle materials using a bond-based peridynamic model," 2021.

[134] S. A. Silling, "Stability of peridynamic correspondence material models and their particle discretizations," *Computer Methods in Applied Mechanics and Engineering*, vol. 322, pp. 42–57, 2017.

[135] M. Behzadinasab and J. T. Foster, "On the stability of the generalized, finite deformation correspondence model of peridynamics," *International Journal of Solids and Structures*, vol. 182, pp. 64–76, 2020.

[136] ——, "Revisiting the third sandia fracture challenge: A bond-associated, semi-lagrangian peridynamic approach to modeling large deformation and ductile fracture," *International Journal of Fracture*, vol. 224, no. 2, pp. 261–267, 2020.

[137] ——, "A semi-lagrangian constitutive correspondence framework for peridynamics," *Journal of the Mechanics and Physics of Solids*, vol. 137, p. 103 862, 2020.

[138] G. Zhang, "Peridynamic models for fatigue and fracture in isotropic and in polycrystalline materials," Ph.D. dissertation, The University of Nebraska-Lincoln, 2017.

[139] A. Dönmez and Z. P. Bažant, "Size effect on branched sideways cracks in orthotropic fiber composites," *International Journal of Fracture*, vol. 222, no. 1, pp. 155–169, 2020.

THE EFFECT OF CRACK-PARALLEL STRESSES ON FRACTURE PROPERTIES OF QUASIBRITTLE AND DUCTILE MATERIALS

Approved by:

Zdeněk P. Bažant
McCormick Institute Professor, Walter P. Murphy Professor of Civil and Environmental Engineering, and (by courtesy) Mechanical Engineering and Material Science and Engineering
Northwestern University

Horacio D. Espinosa
James N. and Nancy J. Farley Professor in Manufacturing & Entrepreneurship, Theoretical and Applied Mechanics Program
Northwestern University

Gianluca Cusatis
Professor of Civil and Environmental Engineering
Northwestern University

Victor Lefèvre
Assistant Professor of Mechanical Engineering
Northwestern University

Date Approved: April 8, 2022

APPENDIX A

BAI-WIERBICKZKI MODEL FOR METALS

Even though one can find the relevant details of this model in the original paper [96], its essential equations are summarized here. First, the three invariants of a stress tensor $\boldsymbol{\sigma}$ are defined respectively by:

$$p = -\sigma_m = -\frac{1}{3}\operatorname{tr}([\sigma]) = -\frac{1}{3}\left(\sigma_1 + \sigma_2 + \sigma_3\right) \tag{A.1}$$

$$q = \bar{\sigma} = \sqrt{\frac{3}{2}\mathbf{S} : \mathbf{S}} = \sqrt{\frac{1}{2}\left[\left(\sigma_1 - \sigma_2\right)^2 + \left(\sigma_2 - \sigma_3\right)^2 + \left(\sigma_3 - \sigma_1\right)^2\right]}$$

$$r = \left(\frac{9}{2}\mathbf{S} \cdot \mathbf{S} : \mathbf{S}\right)^{1/3} = \left[\frac{27}{2}\det(\mathbf{S})\right]^{1/3} = \left[\frac{27}{2}\left(\sigma_1 - \sigma_m\right)\left(\sigma_2 - \sigma_m\right)\left(\sigma_3 - \sigma_m\right)\right]^{1/3} \tag{A.2}$$

where $\mathbf{S}$ is the deviatoric tensor. The dimensionless hydrostatic pressure η and the normalized Lode angle are defined by:

$$\eta = \frac{-p}{q} = \frac{\sigma_m}{\bar{\sigma}} \tag{A.3}$$

$$\bar{\theta} = 1 - \frac{6\theta}{\pi} = 1 - \frac{2}{\pi}\arccos\left(\frac{r}{q}\right)^3 \tag{A.4}$$

The extend plasticity is described by:

$$2\bar{\sigma}_y^{2k} = (\sigma_1 - \sigma_2)^{2k} + (\sigma_2 - \sigma_3)^{2k} + (\sigma_3 - \sigma_1)^{2k} \tag{A.5}$$

$$\bar{\sigma} = A\bar{\varepsilon}^n \left[1 - c_\eta \left(\eta - \eta_0\right)\right] \left[c_\theta^s + \left(c_\theta^{ax} - c_\theta^s\right)\gamma\right] \tag{A.6}$$

$$c_\theta^{ax} = \begin{cases} 1 & \text{for } \bar{\theta} \geq 0 \\ c_\theta^c & \text{for } \bar{\theta} < 0 \end{cases} \tag{A.7}$$

The constitutive relation can be summarized as:

$$\bar{\varepsilon}_f = \left\{ \frac{A}{c_2} \left[1 - c_\eta \left(\eta - \eta_\circ\right)\right] \right.$$
$$\left. \left[c_\theta^s + \frac{\sqrt{3}}{2-\sqrt{3}} \left(c_\theta^{ax} - c_\theta^s\right) \left(\sec\left(\frac{\bar{\theta}\pi}{6}\right) - 1\right)\right] \left[\sqrt{\frac{1+c_1^2}{3}} \cos\left(\frac{\bar{\theta}\pi}{6}\right) + c_1 \left(\eta + \frac{1}{3}\sin\left(\frac{\bar{\theta}\pi}{6}\right)\right)\right] \right\}^{-\frac{1}{n}}$$

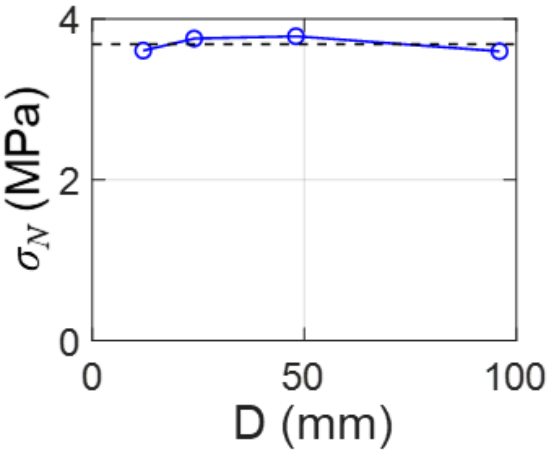

Figure B.1: The constancy of the YZ's size.

APPENDIX B

THE APPROXIMATE CONSTANCY OF THE YIELDING ZONE IN SCALED STRUCTURES WITH SMALL-SCALE YIELDING

In the case of small-scale yielding, the first approach for scaling (Eq.3.38) assumes a constant size of the yielding zone (YZ). To confirm this, we plot the characteristic size of the YZ (which is the cubic root of such zone's volume) of structures at different sizes. These values are measured at the moment when J-integral on the structure at each scale reaches the same value, and the von Mises constitutive law would suffice for this purpose (no crack growth).

The results in Fig. B.1 show that such an assumption is reasonable for the case of the gap test geometry. However, as stated in the chapter 4, the smallest structure must be selected so that its ligament length encloses the whole YZ.

APPENDIX C

DISTINGUISH BETWEEN THE INTRINSIC VS. EXTRINSIC CRACK-PARALLEL STRESS

The effect of the crack parallel stresses on the fracture energy of plastic material was studied by many authors, via analytical and numerical analyses [30], [31]. However, we note that these stresses are considered intrinsic, as they arise from the interaction between the loading configuration and the crack tip constraint stemming from plasticity. Also, their effect is usually quantified by an equivalent elastic annulus surrounding a yielding tip, with an implicit assumption of small-scale yielding. Therefore, the T-stresses (or their normalized version Q in the J-Q theory) increase proportionally with the applied load [116] and consequently, the effect of constant T-stresses is not well-defined.

In our experiments, we intentionally selected a notch-to-length ratio that resulted in zero intrinsic crack-parallel stresses. Note that this is only feasible in bending-tensile specimens. In pure tensile specimens such as single-etch-notch, σ_{xx} is non-zero and does not change sign. Therefore, one should be careful in evaluating the fracture energy of geometrically scaled specimens for this configuration because the peak loads at different sizes would correspond to different values of intrinsic σ_{xx} and hence different r_p. The total σ_{xx} in such analysis should be the sum of the intrinsic and the extrinsic value.

It can be seen in [117, Fig. 4] that not only the intrinsic σ_{xx} is zero at any size, such a value also does not vary with the thickness-to-depth ratio. Therefore, in this study, the total σ_{xx} coincides with the extrinsic values applied by the pad.

APPENDIX D

THE CALIBRATION PROCESS FOR MICROPLANE MODEL, BAI-WIERBICZKI MODEL AND OTHERS

In view of their diverse features, each model in this study had to be calibrated differently. The finite element discretization (which serves as the geometry for all methods) began by selecting the element size. For CB models applied to experiments lacking size effect data (which are what matters most), the element size was initialized as the maximum aggregate size of concrete, d_a, and then updated between d_a and $3d_a$ based on the optimum fitting of existing data. For PF models, a sufficient number of elements need to be included in the band width w_0 to avoid mesh bias and ensure the convergence, which normally range from 3 to 6 elements. For PD models, the horizon size was chosen to be $2.5-3$ times the element size. For fairness of comparison, the horizon radius was chosen to be 1/2 of the crack band width. This ensured that the same RVE volume would be involved in the energy dissipation and that the PD results would be as close as possible to CB results (note that the PD models behave strangely when the element sizes are spatially graded to vary between a chosen minimum and maximum; e.g., in the unnotched three-point-bend specimens in , the crack tends to form where small elements transit to larger elements rather than at midspan).

In the next step, the model parameters have been calibrated to fit best the data for each experiment. In the case of size effect tests, the calibration was based on the peak loads and the load-displacement curve for the smallest specimen, and then adjustments were made for larger sizes. The size effect data, if available, were prioritized over the postpeak data for one size, as they are more unambiguous [26]. Whenever available, data of other tests for the same concrete were also considered; e.g., Hoover *et al.* [118], [119] performed uniaxial compression of cylinders

and prisms, Brazilian tests, size effect tests on beams with different notch-to-depth ratios, etc., on the same concrete with a high consistency. For experiments with more limited material data, qualitative characteristics like crack patterns were also taken into account.

One must also note that each model requires different amount of data. The **bPF** model uses only three parameters—E, G_f and Poisson ratio ν. Hence it requires fewer data than the **CB-M7** model which involves 8 free parameters $E, \nu, k_1, ...k_6$ (also, some parameters are more relevant than others, e.g, ν is unimportant for the Type 2 size effect tests).

For example, in the case of microplane model for concrete the calibration starts with the adjustment of its three scaling parameters to fit the tensile strength and Young's modulus. Four more parameters can be easily adjusted to fit the confined compression data. The initial fracture energy G_f is obtained through the fitting of the maximum loads for scaled notched fracture specimens using the size effect law (if such data exist). If G_f is specified , the scaling parameters of M7 are best adjusted so as to fit the size effect law (SEL) that corresponds to the G_f value [14], [21]. Alternatively, a given G_f can be matched as the area under the initial tangent of the postpeak softening load-displacement curve (corrected for dissipation away from the FPZ, if any). The total fracture energy G_F is obtained as G_f times the ratio of the total areas under the total load-displacement curve and under its initial tangent.

APPENDIX E

DESCRIPTION OF MODELS USED IN CHAPTER 5

E.1 Basic phase-field model

The phase-field concept was introduced more than half a century ago in physical chemistry, as a way of "spreading out", for numerical purposes (e.g. [120, Fig. 2.2]), the Heaviside step function that represents a sharp interface between, for example, the solid and liquid phases of the material (see [120, Fig. 4.1]). Similarly, a sharp crack may be regarded as a Dirac delta function, and the idea is to "spread it out" via a smooth "phase field", φ, as shown in Fig. E.1a) [121]. In the simplest form, the function φ is chosen so that the energy minimization would cause the φ to decay from 1 at the crack line to 0 and $\varphi \propto e^{\pm x/w_0}$. However, φ physically represents no material damage characterized by some constitutive law and there is no associated Irwin' material characteristic length l_c. The length scale w_0 merely serves the numerical purpose of anchoring a sharp line crack with a point-wise tip to the mesh of elastic finite elements, so as to achieve mesh independence of crack direction. The phase parameter φ must be applied as a stiffness reduction factor in the phase-field band of a width w_0 spanning over a sufficient number of finite elements. Thus w_0 represents a "fictitious" damage (or stiffness loss) of the finite element system, as shown in Fig. E.1a by the exponential decay across the imagined (shaded) damage field toward the line crack. Typically, the elasticity matrix of the material is multiplied by $c = 1 - \varphi$ at all finite element integration points in that band.

In each loading step $(t_{n-1}, t),\ n = 1, 2, ...$, one calculates the state vector $\boldsymbol{X}_n = [\boldsymbol{u}_n, \varphi_n]^T$ from the preceding state vector $\boldsymbol{X}_{n-1} = [\boldsymbol{u}_{n-1}, \varphi_{n-1}]^T$ by a variational algorithm (Fig. E.1a)

described as follows:

$$\begin{bmatrix} \boldsymbol{u}_{n-1} \\ \varphi_{n-1} \end{bmatrix} \Rightarrow \quad \downarrow \begin{pmatrix} [\Psi_e]_{\Psi_c=\text{const.}} \Rightarrow \min \\ \\ [\Psi_c]_{\Psi_e=\text{const.}} \Rightarrow \min \end{pmatrix} \uparrow \quad \Rightarrow \begin{bmatrix} \boldsymbol{u}_n \\ \varphi_n \end{bmatrix} \tag{E.1}$$

Starting with $\boldsymbol{X}_{n-1} = [\boldsymbol{u}_{n-1}, \varphi_{n-1}]^T$, the free energy Ψ_e (Helmholtz's, isothermal) of the finite element system with its applied loads and imposed displacements is minimized while keeping the phase-field parameter $\varphi = \varphi_{n-1}$ (or its free energy Ψ_{cn-1}) constant. This yields a system of linear equations for $\boldsymbol{u}$. Then the free energy Ψ_c of the phase-field φ is minimized while keeping Ψ_e constant. This yields another system of equations for the discrete values of φ. These minimization may but need not be iterated. The result is the new vector $\boldsymbol{X}_n = [\boldsymbol{u}_n, \varphi_n]^T$ at the end of the loading step. This alternative minimization (which is usually referred to as the "staggered scheme") makes the algorithm efficient.

The key feature of the phase field is the expression for the free energy. Its convenient form is:

$$\Psi_c = \int_\Omega \frac{G_f}{2w_0} \left(\varphi^2 + w_0^2 |\nabla\varphi|^2\right) \, \mathrm{d}V \tag{E.2}$$

where G_f is the fracture energy of the material which, together with the elasticity matrix, forms the complete input of material properties; V is the volume of the body domain Ω, and ∇ is the gradient operator.

Upon minimization of Ψ_c, in which the expression in the parenthesis was postulated in 1998 by Francfort and Marigo [121], leads to the vanishing of the following expression as a function of the transverse coordinate, x:

$$w_0^2 |\nabla\varphi|^2 - \varphi^2 = 0 \tag{E.3}$$

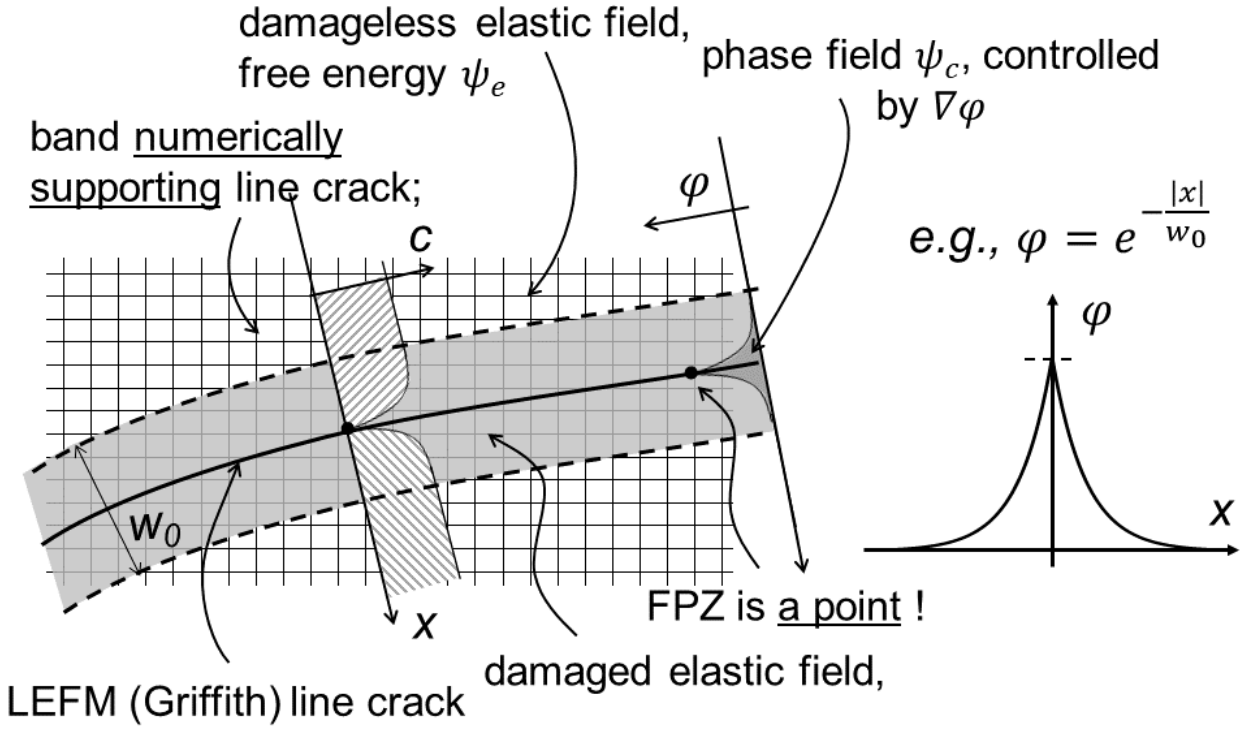

Figure E.1: Schematic concept of phase-field φ, chosen with w_0 or supporting band, and profile of damage $c = 1 - \varphi$.

This is a differential equation for phase-field variable φ. Its solution for φ = 1 at the crack line is: $\varphi = e^{-|x|/w_0}$. Some other expressions, giving more complicated decay functions φ, have also been introduced [122] to improve the representation of a certain type of fracture.

To validate the phase-field models, good fits of a few selected experiments, such as propagating curved cracks, have often been presented as supportive evidence. For example, [123, Figs. 19, 20] presented an experimental validation for a standard compact tension specimen with a hole drilled on the side of the notch extension line including 1) the up-and-down curve of load versus deflection along with the curve of crack length versus the crack opening displacement; and 2) the crack path in the same specimen. The hole causes the crack to run toward it, and the phase-field predictions matched these observations, qualitatively as well as quantitatively. However, the question of scaling was left unanswered.

Another validation attempt used a standard double-edge-notched tensile specimen under axial tensile loads at the ends. Without a check of instability breaking symmetry, two opposite curved cracks are predicted to propagate from both sides symmetrically [124, Fig. 4]. Even though the load versus displacement curve agreed with the test, the overall failure prediction was unsatisfactory since the energy analysis of the stability of the of post-bifurcation path [49], [125] showed that only a crack from one side can propagate.

An obvious weakness of the phase-field model is that the existing validated constitutive laws cannot be used directly. Instead, they need to be approximated in terms of free or potential energy functions, which cannot be fully equivalent and lead to complicated material characterizations in terms of multiple inelastic functions and complex loading/unloading responses.

Another weakness of the phase-field models is the arbitrariness in the choice of boundary condition imposed upon the microscopic force (i.e., the state variable that is work-conjugated with the phase variable). Mostly the Neumann boundary condition is chosen, but with no meaningful

physical justification.

E.2 Phase-field modifications by Feng and Wu

Feng and Wu [126] modified the degradation and the dissipation functions of the original PF model [121] to approximate the energy dissipation by the cohesive force acting along the FPZ. His energy density reads:

$$\Psi(\varepsilon(\mathbf{u}), g(\varphi)) = g(\varphi)\Psi_0^+(\varepsilon(\mathbf{u})) + \Psi_0^-(\varepsilon(\mathbf{u})) + \frac{G_f}{4c_w w_0}\left(w(\varphi) + w_0^2|\nabla\varphi|^2\right) \tag{E.4}$$

where $$g(\varphi) = \frac{(1-\varphi)^d}{(1-\varphi)^d + a\varphi(1+b\varphi)}, \quad a = \frac{4EG_f}{\pi w_0 f_t^2} \tag{E.5}$$

$$\Psi_0^+ = \frac{\langle\sigma_1\rangle_+^2}{2E};\ \Psi_0^- = \frac{1}{2E}\left[\sigma_I\langle\sigma_I\rangle_- + \sigma_{II}^2 + \sigma_{III}^2 - 2\nu\left(\sigma_{II}\sigma_{III} + \sigma_I\sigma_{III} + \sigma_I\sigma_{II}\right)\right] \tag{E.6}$$

$$w(\varphi) = 2\varphi - \varphi^2, \quad c_w = \int_0^1 \sqrt{w(\zeta)}\mathrm{d}\zeta \tag{E.7}$$

Using calculus of variations, one can find the solution $[\mathbf{u}, \varphi]^T$ that minimizes the integral of the energy function (E.4) over the entire domain.

E.3 Phase-field modifications by Fei and Choo

Fei and Choo separated the energy density into three parts: elastic, fracture and interfacial friction, separated by a threshold fracture energy $\mathcal{H}_t$:

$$\Psi = \Psi^e + \Psi^f + \frac{3\mathcal{G}_{fII}}{8w_0}\left(\varphi + w_0^2|\nabla\varphi|^2\right) \tag{E.8}$$

where $$\Psi^e = \int_{t_p}^{t} \sigma_{bulk} : \dot{\varepsilon}\mathrm{d}t - \int_{t_p}^{t} [1 - g(\varphi)]\tau_{bulk}\dot{\gamma}\mathrm{d}t \tag{E.9}$$

$$\Psi^f = \int_{t_p}^{t} [1 - g(\varphi)]\tau_r\dot{\gamma}\mathrm{d}t \tag{E.10}$$

$$g(\varphi) = \frac{(1-\varphi)^n}{(1-\varphi)^n + m\varphi(1+p\varphi)},\ n = 2,\ p \geq 1,\ m = \frac{3\mathcal{G}_{fII}}{8w_0}\frac{1}{\mathcal{H}_t} \tag{E.11}$$

E.4 Overview of the concept of peridynamics

The theory of peridynamics was formulated (and the new term conceived) in 2000 by Silling [127]. Later it branched into several versions [128], [129]. The original and simplest version of peridynamics, the bond-based model [128], is characterized by the integral:

$$\rho(\mathbf{x})\ddot{\mathbf{u}}(\mathbf{x},t) = \int_H \mathbf{f}\left(\mathbf{u}' - \mathbf{u}, \mathbf{x}' - \mathbf{x}, t\right)\mathrm{d}H + \mathbf{b}(\mathbf{x},t) \tag{E.12}$$

where t = time, $\mathbf{x}$ = coordinate vector of material point, $\mathbf{u}$ = displacement vector at the center point, ρ = mass density, $\mathbf{b}$ = body force vector; H = volume or area within the assumed horizon, $\mathbf{f}$ = assumed function characterizing the central interacting force between material points. The bond-based version assumes that all central-force bond interactions are independent of each other. This assumption leads to a fixed Poisson's ratio equal to 0.25 [130] and limits further generalizations.

To overcome this problem, a version of peridynamics called "state-based" [129] was created

upon introducing the assumption that the interacting forces within a horizon are inter-dependent and could be characterized by means of the states of forces $\mathbf{T}$ and states of deformation vectors in all the bonds emanating from the same center $\mathbf{Y}$:

$$\rho(\mathbf{x})\ddot{\mathbf{u}}(\mathbf{x},t) = \int_H \left[\underline{\mathbf{T}}(\mathbf{x},t)\left\langle \mathbf{x}'-\mathbf{x}\right\rangle - \underline{\mathbf{T}}\left(\mathbf{x}',t\right)\left\langle \mathbf{x}-\mathbf{x}'\right\rangle\right] \mathrm{d}H + \mathbf{b}(\mathbf{x},t) \tag{E.13}$$

It has been generally overlooked that (as pointed out in [72]) peridynamics actually represents a mathematically rigorous refinement and generalization of the "network model" proposed in 1977 by Burt and Dougill [131]. In that model, a field of random nodes is created and each node is connected by bars to all adjacent nodes up to a certain maximum distance (which is what is in peridynamics called the horizon radius). After criticisms at conferences, these authors promptly switched to another approach.

In 2016 [72], several fundamental problems with the concept of peridynamics were identified, as follows:

1) *Lattice microstructure:* The basic physical problem with peridynamics is that it implies a lattice microstructure (Fig. E.2a), which leads to a particle-skipping potential and a neglect of shear interactions that resist particle rotations. The lattice microstructure is unrealistic even for the state-based version. Although that version allows the equivalent continuum strain and stress tensors for each center point to be calculated and thus any constitutive damage model including the microplane model M7 to be applied, the underlying lattice characterized by central forces exists nonetheless.

2) *Particle skipping interactions* are another physically unrealistic feature of peridynamics. These fictitious interactions are particularly detrimental for the modeling of compression-shear damage and fracture. In reality, the material contains finite particles which not only displace but

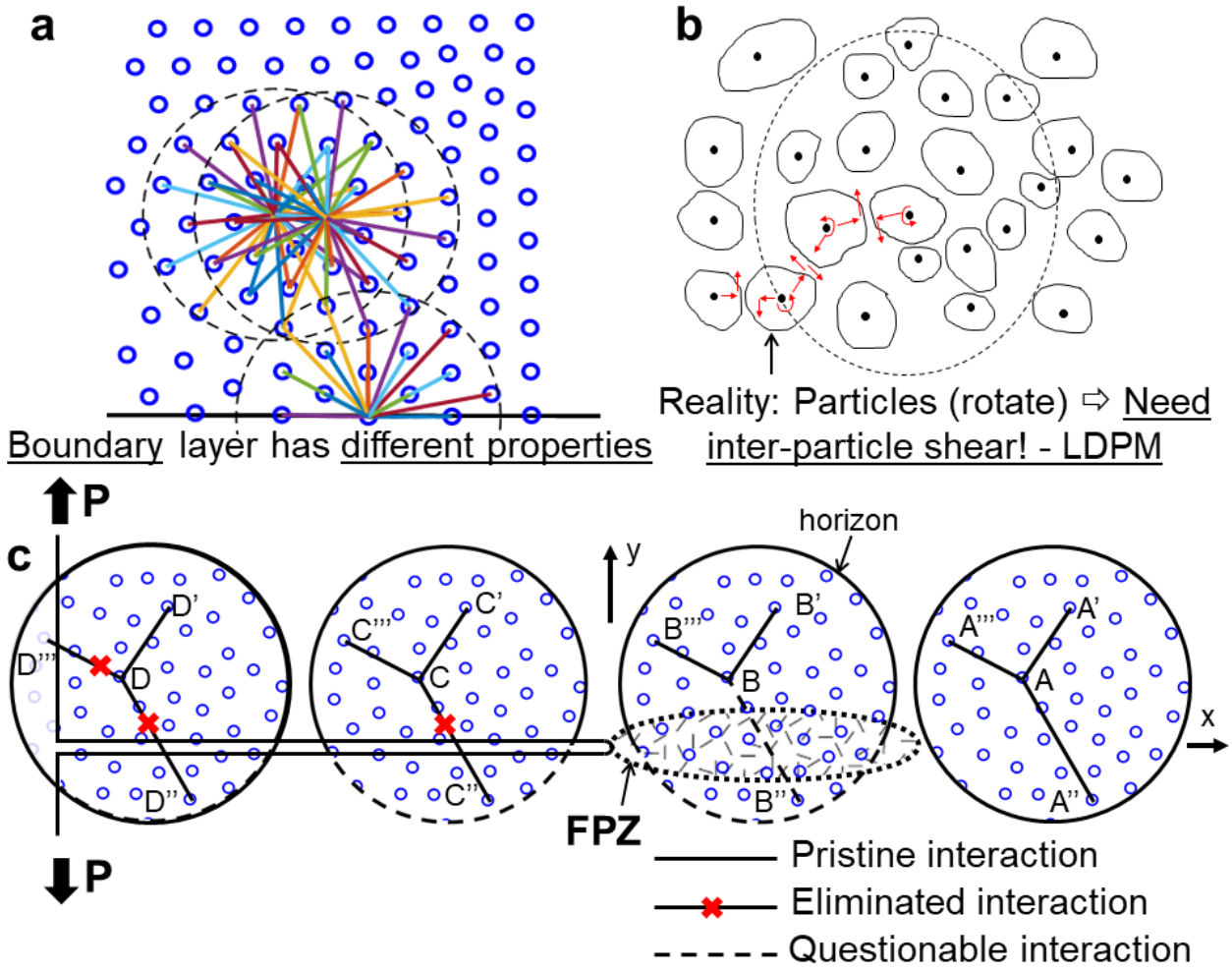

Figure E.2: a) Central forces (or lattice bonds) connecting each material point to all other material points within its horizon, shown as two dashed circles, and the same for the horizon (unreduced) of a point at the boundary (note the reduced density of connections near the boundary) [130]. b) Particles (or grains) in a quasibrittle material and their interactions by contact normal and shear forces. c) Horizons spanning a crack or fracture process zone, with interactions AA′, AA″, AA‴, BB′, CC′, DD′ when considered undisturbed by the crack (note that CC″, DD″ must be eliminated, while BB″ is getting progressively weaker while moving along the FPZ closer to crack tip.

also rotate (Fig. E.2b). Above the atomic scale, no potential communicating particle-skipping interactions exists. Indeed, interactions with the second and farther neighbors are communicated through the intermediate particles, by interparticle normal and shear forces. The shear forces resist relative rotations of particles (which is the basis of the LDPM model [10], [11]. Another oddity of the particle skipping interactions is that, in the bond-based version of peridynamics, the micromodulus governing the overall material stiffness has the queer dimension of MN/m^6.

3) *Boundary conditions:* The peridynamic horizon that skips several particles inevitably leads to unphysical boundary conditions, as well as crack face conditions and and FPZ border conditions (Fig. E.2). The horizon of the nodes located near the boundary protrudes outside the boundary or across the open crack. To prevent it, such interactions must be deleted. This alone would, of course, significantly decrease the stiffness and strength of the boundary layer or crack surface layer (of thickness δ_B = horizon radius).

To clarify the last point graphically, consider the diagrams in Fig. E.2a, which shows the central force interactions within a circular horizon that emanate from the central point. When the horizon reaches beyond the boundary, the protruding central force interactions must be deleted. But this causes a major decrease of the stiffness and strength of the boundary layer. Also, it degrades the accuracy of the calculation of the deformation gradient in the correspondence state-based method. To counter this problem, surface-correction factors have been applied, as reported in [130]. But again this is only a partial remedy.

Another problem arises in applying the free surface boundary conditions. Since the displacement derivatives are unavailable for PD, a surface traction needs to be smeared over a certain volume. The displacement and velocity boundaries, however, are usually applied indirectly onto an imagined no-fail zone [130] considered as an undamaged zone of the material.

4) *Boundary conditions at crack faces and the FPZ dilemma*: The boundary problem is more

severe and more complicated at the crack faces, and even more so at the boundary of the FPZ or the cohesive crack zone. Ahead of the crack and of its FPZ (Fig. E.2c), the central force interaction along segment AA″ crossing the crack extension line is, of course, undisturbed. The interaction along segments or CC″ or DD″ crossing the open crack must be deleted, and the same surface correction factor must be introduced. A tougher predicament arises for the interactions along segment BB″ crossing the FPZ, for which the central forces crossing the FPZ get weakened only partly—strongly near the crack tip, where the damage is high, but weakly near the front of damage zone (dashed ellipse in the figure), where the damage is still developing. A satisfactory, physically realistic resolution of the FPZ predicament looks impossible (this will be shown in the following comparisons with experiments).

5) *Homogenization, localization, wave dispersion, fatigue:* Another physical problem, highlighted in [72], is that the same material length, the horizon, governs both the elastic homogenization and damage localization. Dispersion of waves by damage or plastic zones, and by innate heterogeneity cannot be distinguished and independently controlled. However, experimental comparisons with wave propagation experiments are beyond the scope of this study. So is the fatigue loading of materials such as concrete [132], which is another unresolved problem.

The previous criticism of peridynamics [72] was strictly theoretical. No support by comparisons with experiments was given. This is remedied here. Comparisons are given not only for PD but also for PF models. In many cases, different versions of PD models, i.e., bond-based and state-based, give very different predictions for the same experiment. Even worse, subcategories of state-based models, which are ordinary and non-ordinary (the latter are usually misnamed as the ”correspondence-based” models) [130], suffer from the same deficiency. In this study, both ”state-based” model types have been investigated. The performance of a bond-based model [133] will be briefly discussed in Appendix B.

E.5 The mathematical basis of bond-associated PD

The PD deformation gradient is originally defined in [129], [130]. If combined with nodal quadrature, it permits zero-energy deformation modes [134], [135]. Therefore, in a recent development [136], [137], a new Lagrangian correspondence-based deformation gradient associated with bonds connecting material points $\mathbf{X}$ and $\mathbf{X}'$ has been proposed:

$$\mathbf{F}\left(\mathbf{X},\mathbf{X}'\right)=\mathbf{F}^{avg}\left(\mathbf{X},\mathbf{X}'\right)+\mathbf{F}^{corr}\left(\mathbf{X},\mathbf{X}'\right) \tag{E.14}$$

$$\mathbf{F}^{avg}\left(\mathbf{X},\mathbf{X}'\right)=\frac{\mathbf{F}(\mathbf{X})+\mathbf{F}\left(\mathbf{X}'\right)}{2} \tag{E.15}$$

$$\mathbf{F}^{corr}\left(\mathbf{X},\mathbf{X}'\right)=\left(\left(\mathbf{x}'-\mathbf{X}\right)-\mathbf{F}^{avg}\left(\mathbf{X},\mathbf{X}'\right)\cdot\left(\mathbf{X}'-\mathbf{X}\right)\right)\otimes\frac{\left(\mathbf{X}'-\mathbf{X}\right)}{\left|\left(\mathbf{X}'-\mathbf{X}\right)\right|^{2}} \tag{E.16}$$

the authors computed the basis-function gradient by methods commonly used in the mesh-free formulation. The accuracy of the gradient calculation is assured by the polynomial-reproducing conditions imposed on these basis functions.

E.6 The mathematical form of CDPM2 model by Grassl *et al.* [66]

The stress tensor at a material point is computed by:

$$\boldsymbol{\sigma}=\left(1-\omega_t\right)\overline{\boldsymbol{\sigma}}_t+\left(1-\omega_c\right)\overline{\boldsymbol{\sigma}}_c;\ \overline{\boldsymbol{\sigma}}=\mathbf{D}_e:\left(\boldsymbol{\varepsilon}-\boldsymbol{\varepsilon}_p\right) \tag{E.17}$$

The plasticity part of the model can be written as:

$$f_p\left(\overline{\boldsymbol{\sigma}},\kappa_p\right)=F\left(\overline{\boldsymbol{\sigma}},q_{\mathrm{h1}},q_{\mathrm{h2}}\right) \tag{E.18}$$

$$\dot{\varepsilon}_p=\dot{\lambda}\frac{\partial g_p}{\partial\overline{\boldsymbol{\sigma}}}\left(\overline{\boldsymbol{\sigma}},\kappa_p\right) \tag{E.19}$$

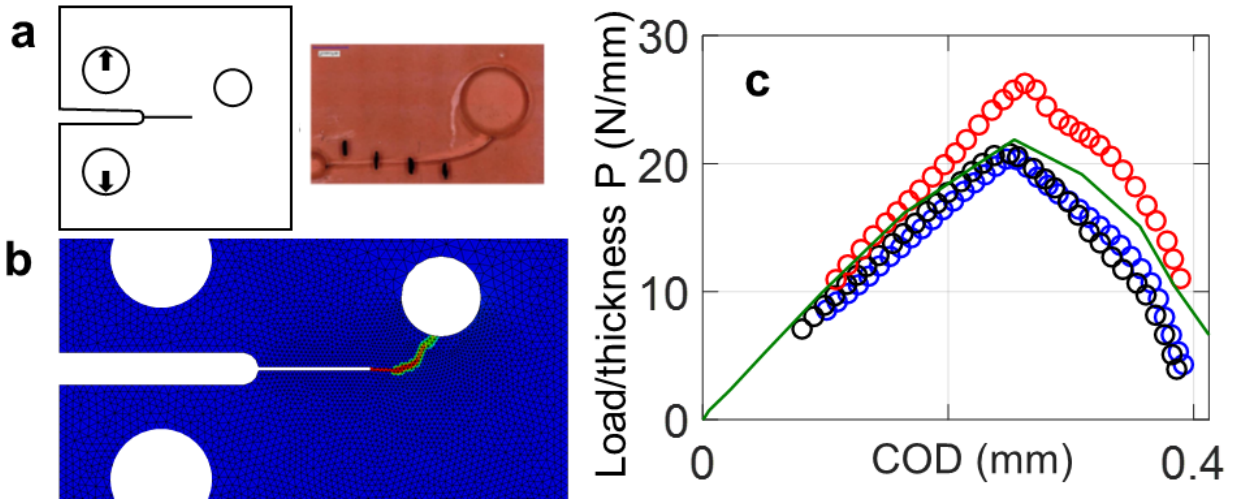

Figure E.3: a) A curved crack on the compact-tension specimen with a hole in front of the notch is captured by the CB model in (b). c) The load versus crack-opening-displacement (COD) curve of the specimen in (a).

Note that the plastic potential g_p and plastic loading function f_p are different. The growth of compressive and tensile damages is described as:

$$f_{dt} = \tilde{\varepsilon}_t(\overline{\boldsymbol{\sigma}}) - \kappa_{dt} \tag{E.20}$$

$$f_{dt} \leq 0, \quad \dot{\kappa}_{dt} \geq 0, \quad \dot{\kappa}_{dt} f_{dt} = 0 \tag{E.21}$$

$$\omega_t = g_{dt}\left(\kappa_{dt}, \kappa_{dt1}, \kappa_{dt2}\right) \tag{E.22}$$

$$f_{dc} = \alpha_c \tilde{\varepsilon}_c(\overline{\boldsymbol{\sigma}}) - \kappa_{dc} \tag{E.23}$$

$$f_{dc} \leq 0, \quad \dot{\kappa}_{dc} \geq 0, \quad \dot{\kappa}_{dc} f_{dc} = 0 \tag{E.24}$$

$$\omega_c = g_{dc}\left(\kappa_{dc}, \kappa_{dc1}, \kappa_{dc2}\right) \tag{E.25}$$

E.7 The ability of the crack-band microplane model in describing curved crack

For a finite crack front width, the direction of crack growth is significantly affected by the triaxial stress state at the front. This effect plays a role in the curved propagation of a crack band in a

compact tension specimen in which a hole has been drilled on the side of the crack extension line. As mentioned in Sections 3 and 4, both PF and PD [123], [138] predict a smoothly curved crack running into the hole. Despite the ruggedness imposed by the mesh, the M7 crack band model, too, predicts a similar curved path into the hole; Fig. E.3. Note that, even if the band were not rugged, the path could not be identical. The reason is that the aforementioned triaxial stress effect, influencing the crack path direction, cannot be captured correctly by the PD and PF models. Therefore, and also because of missing the crack-parallel compression, the PD and PF crack paths cannot be quite realistic. This triaxiality effect in the FPZ is best manifested by sideways crack propagation in orthotropic fiber composites, making a sharp angle on the crack path. Such as path is correctly predicted correctly by the crack band model [139] but not by LEFM, PF and PD models (nor by the cohesive crack model).

LIST OF PUBLICATIONS

[1] H. Nguyen, M. Pathirage, M. Rezaei, M. Issa, G. Cusatis, and Z. P. Bažant, "New perspective of fracture mechanics inspired by gap test with crack-parallel compression," *Proceedings of the National Academy of Sciences*, vol. 117, no. 25, pp. 14015–14020, 2020.

[2] H. T. Nguyen, M. Pathirage, G. Cusatis, and Z. P. Bažant, "Gap test of crack-parallel stress effect on quasibrittle fracture and its consequences," *Journal of Applied Mechanics*, vol. 87, no. 7, p. 071012, 2020.

[3] H. T. Nguyen, A. A. Dönmez, and Z. P. Bažant, "Structural strength scaling law for fracture of plastic-hardening metals and testing of fracture properties," *Extreme Mechanics Letters*, vol. 43, p. 101141, 2021.

[4] A. A. Dönmez, H. T. Nguyen, and Z. P. Bažant, "Crack-parallel stress effect on fracture energy of plastic hardening polycrytstalline metal identified from gap test scaling," *In preparation*.

[5] X. Zhang, H. Nguyen, J. Wen, X. Zhang, P. M. Ajayan, and H. D. Espinosa, "Atomistic measurement and modeling of intrinsic fracture toughness of two-dimensional materials," *In preparation*.

[6] H. Nguyen, X. Zhang, J. Wen, X. Zhang, P. M. Ajayan, and H. D. Espinosa, "Vacancies in transition metal dichalcogenide monolayers and their impact on fracture," *In review at Nature Communications*.

[7] R. A. Soler-Crespo, W. Gao, L. Mao, H. T. Nguyen, M. R. Roenbeck, J. T. Paci, J. Huang, S. T. Nguyen, and H. D. Espinosa, "The role of water in mediating interfacial adhesion and shear strength in graphene oxide," *ACS nano*, vol. 12, no. 6, pp. 6089–6099, 2018.

[8] S. Rahimi-Aghdam, V.-T. Chau, H. Lee, H. Nguyen, W. Li, S. Karra, E. Rougier, H. Viswanathan, G. Srinivasan, and Z. P. Bažant, "Branching of hydraulic cracks enabling permeability of gas or oil shale with closed natural fractures," *Proceedings of the National Academy of Sciences*, vol. 116, no. 5, pp. 1532–1537, 2019.

[9] I. Benedetti, H. Nguyen, R. A. Soler-Crespo, W. Gao, L. Mao, A. Ghasemi, J. Wen, S. Nguyen, and H. D. Espinosa, "Formulation and validation of a reduced order model of 2d materials exhibiting a two-phase microstructure as applied to graphene oxide," *Journal of the Mechanics and Physics of Solids*, vol. 112, pp. 66–88, 2018.

[10] H. T. Nguyen, S. Rahimi-Aghdam, and Z. P. Bažant, "Sorption isotherm restricted by multilayer hindered adsorption and its relation to nanopore size distribution," *Journal of the Mechanics and Physics of Solids*, vol. 127, pp. 111–124, 2019.

[11] R. A. Soler-Crespo, L. Mao, J. Wen, H. T. Nguyen, X. Zhang, X. Wei, J. Huang, S. T. Nguyen, and H. D. Espinosa, "Atomically thin polymer layer enhances toughness of graphene oxide monolayers," *Matter*, vol. 1, no. 2, pp. 369–388, 2019.

[12] X. Zhang, H. Nguyen, M. Daly, S. T. Nguyen, and H. D. Espinosa, "Nanoscale toughening of ultrathin graphene oxide-polymer composites: mechanochemical insights into hydrogen-bonding/van der waals interactions, polymer chain alignment, and steric parameters," *Nanoscale*, vol. 11, no. 25, pp. 12305–12316, 2019.

[13] H. Nguyen, S. Rahimi-Aghdam, and Z. P. Bažant, "Unsaturated nanoporomechanics," *Proceedings of the National Academy of Sciences*, vol. 117, no. 7, pp. 3440–3445, 2020.

[14] H. D. Espinosa, A. Zaheri, H. Nguyen, D. Restrepo, M. Daly, M. Frank, and J. McKittrick, "In situ wear study reveals role of microstructure on self-sharpening mechanism in sea urchin teeth," *Matter*, vol. 1, no. 5, pp. 1246–1261, 2019.

[15] W. Li, L. P. Frash, J. W. Carey, N. J. Welch, M. Meng, H. Nguyen, H. S. Viswanathan, E. Rougier, Z. Lei, S. Rahimi-Aghdam, *et al.*, "Injection parameters that promote branching of hydraulic cracks," *Geophysical Research Letters*, vol. 48, no. 12, p. e2021GL093321, 2021.

[16] H. Nguyen, S. Rahimi-Aghdam, and Z. P. Bažant, "Time lag in measuring pore humidity in concrete by a gage in finite cavity," *Materials and Structures*, vol. 51, no. 1, pp. 1–9, 2018.

[17] W. Li, L. Frash, J. Carey, M. Meng, H. Viswanathan, E. Rougier, Z. Lei, V. Chau, T. Nguyen, S. Rahimi-Aghdam, *et al.*, "Experimental investigation of hydraulic fracture branching," in *54th US Rock Mechanics/Geomechanics Symposium*, OnePetro, 2020.

[18] W. Li, L. Frash, J. Carey, N. Welch, M. Meng, H. Viswanathan, H. Nguyen, S. Rahimi-Aghdam, and Z. Bažant, "Effect of injection parameters on hydraulic fracture branching," in *55th US Rock Mechanics/Geomechanics Symposium*, OnePetro, 2021.

[19] Z. P. Bažant, A. A. Dönmez, and H. T. Nguyen, "Précis of gap test results requiring reappraisal of line crack and phase-field models of fracture mechanics," *Engineering Structures*, vol. 250, p. 113285, 2022.

[20] J. Y. Choi, X. Zhang, H. T. Nguyen, M. R. Roenbeck, L. Mao, R. Soler-Crespo, S. T. Nguyen, and H. D. Espinosa, "Atomistic mechanisms of adhesion and shear strength in graphene

oxide-polymer interfaces," *Journal of the Mechanics and Physics of Solids*, vol. 156, p. 104578, 2021.

[21] X. Zhang, H. Nguyen, J. T. Paci, S. K. Sankaranarayanan, J. L. Mendoza-Cortes, and H. D. Espinosa, "Multi-objective parametrization of interatomic potentials for large deformation pathways and fracture of two-dimensional materials," *npj Computational Materials*, vol. 7, no. 1, pp. 1–11, 2021.

[22] H. T. Nguyen, F. C. Caner, and Z. P. Bažant, "Conversion of explicit microplane model with boundaries to a constitutive subroutine for implicit finite element programs," *International Journal for Numerical Methods in Engineering*, vol. 122, no. 6, pp. 1563–1577, 2021.

[23] Z. P. Bazant, H. T. Nguyen, and A. A. Dönmez, "Critical comparison of phase-field, peridynamics and crack band model m7 in light of gap test and classical fracture tests," *Journal of Applied Mechanics*, pp. 1–79.